NEUTRAL MESON PHOTOPRODUCTION FROM HYDROGEN AT FORWARD ANGLES IN THE PHOTON ENERGY RANGE 750 - 1500 MeV

Thesis by

G. Laurie Hatch

In Partial Fulfillment of the Requirements

For the Degree of

Doctor of Philosophy

California Institute of Technology

Pasadena, California

1967

(Submitted November 18, 1966)

ACKNOWLEDGMENTS

The author wishes to thank C. R. Clinesmith and Professor A. V. Tollestrup for their material help, moral support, and dependable advice. The measurements reported in this thesis were taken in collaboration with C. R. Clinesmith.

The experiment could not have been performed without the expert and sometimes inspired aid of Drs. A. V. Tollestrup, Joe Mullins, Charlie Peck, and Owen Maloy; Al Neubieser, Walter Nilsson and other members of the Synchrotron staff and crew. Of course, the Synchrotron will simply not operate properly without Larry Loucks. The author wishes to thank Mrs. B. Hall, Miss C. Carter, and Bette Brent for the preparation and finally typing of the thesis manuscript.

A special thanks goes to Professor R. L. Walker, both for his support of this project as laboratory administrator and for his personal encouragement during trying times.

The financial support of the U. S. Atomic Energy Commission and the General Electric Foundation is gratefully acknowledged.

ABSTRACT

Measurements have been made of the cross-sections for neutral meson photoproduction from protons at angles in the forward hemisphere for photon energies near 911, 1182, and 1390 MeV. The experimental method consists of detecting the decay gamma-rays of the neutral meson in two pb-glass total absorption Čerenkov counters. The results agree very well with the existing data where the same points have been measured.

The striking feature of the angular distributions at 1182 and 1390 MeV is the small 0° cross-section and the peak near 30° to 40° in the CMS. Using as a model for the cross-section calculation a vector meson X^{o} exchange plus background, we find the product $\Gamma (X^{o} \rightarrow \pi^{o} + \gamma) \times \frac{\gamma^{2}_{XNN}}{4\pi} \simeq 1.8 \pm 0.2$ MeV for $M_{X} = 788$ MeV. Fits made without the vector meson pole are not inconsistent with a resonance model for the cross-section.

TABLE OF CONTENTS

I. INTRODUCTION

Measurements made by Talman et al.[1] of the photoproduction cross-sections for π^o mesons at photon energy near 1160 MeV show that above the third resonance the cross-section is very similar to that expected from a neutral vector meson pole. They were able to fit their angular distribution using mainly the exchange term represented by the Feynman diagram below,

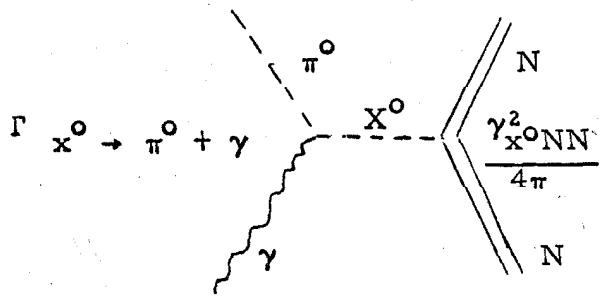

where a neutral meson of spin 1 is exchanged. The cross-section when computed using just this diagram has the feature that it is zero at 0^o and rises proportional to $\sin^2\theta$ for small angles to a maximum, then finally falls off at backward angles. In addition, the location of the pole in the unphysical region moves closer to 0^o as the photon energy increases causing the maximum in the cross-section to grow larger and move closer towards 0^o. At k = 1160 MeV one should also expect substantial contributions to the cross-section from the third nucleon resonance at k = 1050 MeV in addition to general background. Moravcsik[2] has given a prescription (described in text of thesis) for extracting the coupling constants from the angular distribution when sources in addition to the pole term are contributing to the cross-section. Talman[10] used this method to find the product

$\Gamma (x^o \rightarrow \pi^o + \gamma) \times \frac{\gamma^2_{x^oNN}}{4\pi} = 0.5 \pm 0.1$ MeV when the mass of the X^o meson was set equal to 780 MeV. The width $\Gamma(\omega^o \rightarrow \pi^o + \gamma)$ is now known to be 1.1 MeV and the best estimate of $\frac{\gamma^2_{\omega^oNN}}{4\pi}$ is ~3, hence one should expect the product $\Gamma(X^o \rightarrow \pi^o + \gamma) \times \frac{\gamma^2_{x^oNN}}{4\pi}$ to be somewhat larger than Talman's result if the exchange term is present and if the exchange particle is an ω^o. However, the measurements by Talman are not sufficiently accurate to make the long extrapolation to the pole at $\cos \theta = 1.81$ with much confidence. Clearly more precise measurements of the cross-section at 1000 MeV and higher energies would be necessary in order to see if the vector meson exchange term is present in the cross-section.

It should also be pointed out that any of the other vector meson resonances of mass comparable to the ω^o may be the exchange particle. An obvious possibility is the isovector ρ meson. To decide between the isoscalar ω^o and the isovector one could exploit the difference in their isospins. The amplitudes for photoproducing a π^o meson from a neutron and from a proton are equal when the isoscalar meson is exchanged, whereas the amplitudes are equal but of opposite sign, when an isovector meson is exchanged. To measure the photoproduction cross-section for the free neutron requires measuring the two reactions

$$(A) \quad \gamma + p \rightarrow p + \pi^o$$

$$(B) \quad \gamma + d \rightarrow d + \pi^o$$

and then performing a subtraction. Clearly, both reactions must be measured accurately in order to obtain statistically significant results for the neutron cross-sections.

The author and C. R. Clinesmith undertook the task of measuring reactions (A) and (B) using the same technique as Talman et al.[1] Improvements in the CalTech Synchrotron photon beam intensity and electronic circuit design permitted more rapid accumulation of data with the result that the statistical accuracy of the measured points should be much better than in previous measurements. Also, the increase in the maximum energy of the bremsstrahlung beam of the Synchrotron made possible measurements of the reactions (A) and (B) at higher energy. In this thesis the cross-sections for the reaction $\gamma + p \rightarrow p + \pi^o$ are presented, while in C. R. Clinesmith's thesis the cross-sections for the reaction $\gamma + d \rightarrow d + \pi^o$ and $\gamma + n \rightarrow n + \pi^o$ are given.

The purposes of the experiment can be summarized.

(1) Repeat with improved statistics the measurements of the π^o meson photoproduction cross-section for hydrogen made by Talman [10] at photon energies of 900 MeV and 1150 MeV.

(2) Measure the π^o meson photoproduction cross-sections for hydrogen and deuterium at energies ranging from 900 MeV to the maximum energy of the CalTech Synchrotron, i.e., about 1500 MeV.

(3) Extract the π^o meson photoproduction cross-sections for the neutron.

(4) Unfold the photon energy dependence of the π^o meson photoproduction cross-section for the proton.

II. METHOD

A. Detection

To measure the π^o meson photoproduction cross-section for the reaction $\gamma + p \rightarrow p + \pi^o$ a liquid hydrogen target of cross-sectional density 1.17 g/cm^2 was placed in the photon beam of the CalTech Synchrotron (Figure A1, Page 6). The emerging π^o mesons decay very rapidly into two gamma rays which are detected by two energy sensitive Pb-glass total absorption Cerenkov counters. These counters have an output proportional to the energy of the gamma ray and an energy resolution given by $\sigma(\text{MeV}) = 65 \sqrt{E^{\gamma}(\text{BeV})}$. The two counters were placed one above the other (Figure 1) on a trolley which could be rolled on tracks to the various π^o meson laboratory production angles θ_π desired. The energy of the π^o meson E_π is computed by summing the two gamma ray energies E_1^γ and E_2^γ measured in the Čerenkov counters. Since the reaction is a two body process all the necessary kinematic parameters can be determined from the total laboratory energy E_π and production angle θ_π of the π^o. A list of the kinematics parameters is contained in Table 1, page 30.

Since photons of all energies up to the endpoint energy (E_o) of the bremsstrahlung spectrum are present in the synchrotron photon beam, the energy or energy spread of the photons initiating the reaction must be determined from the acceptance parameters of the detection equipment. The upper end of the photon energy range is fixed by the endpoint energy of the bremsstrahlung beam. The lower end is set by using kinematic properties of the π^o decay.

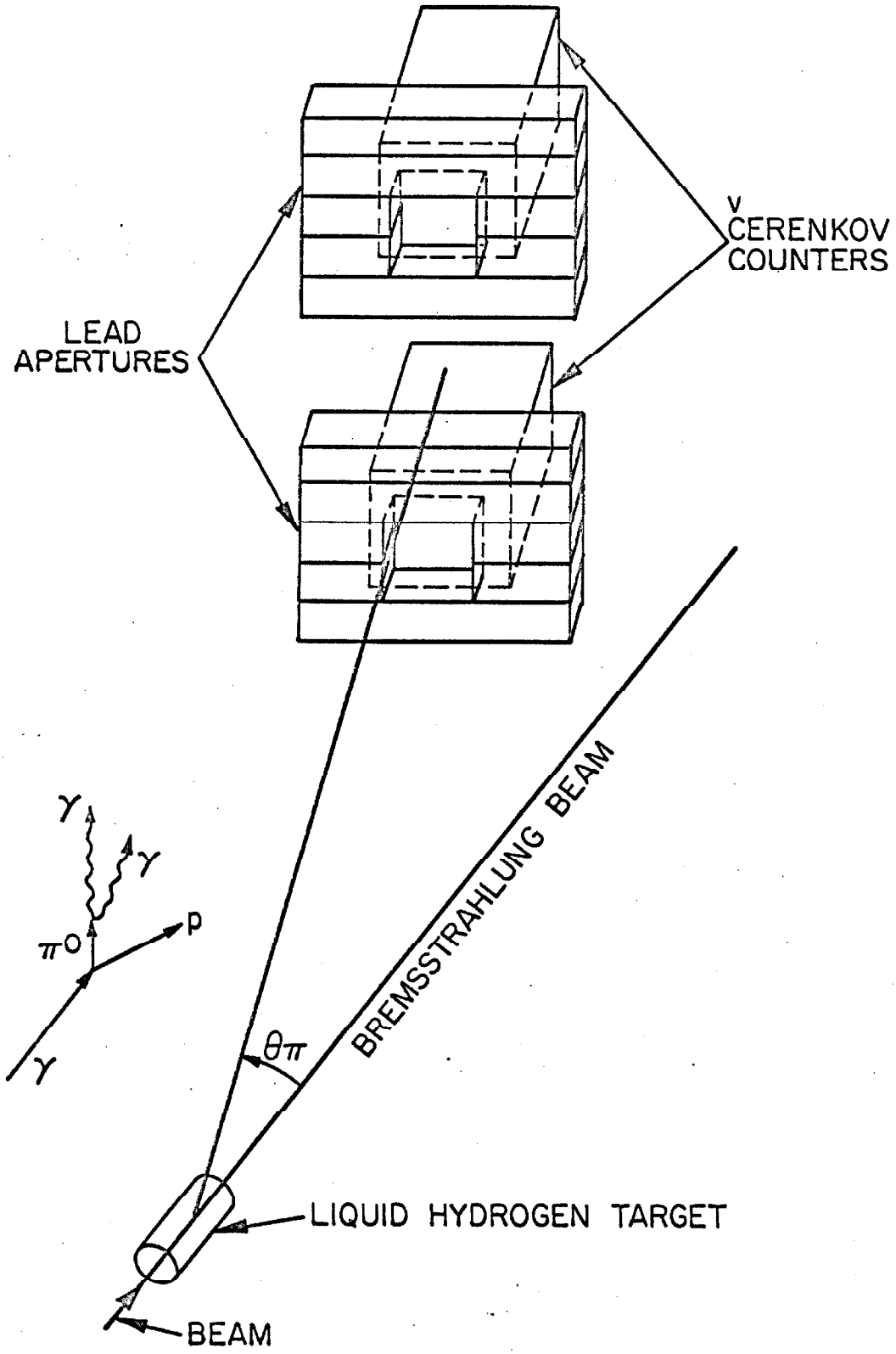

FIGURE 1: EXPERIMENTAL ARRANGEMENT

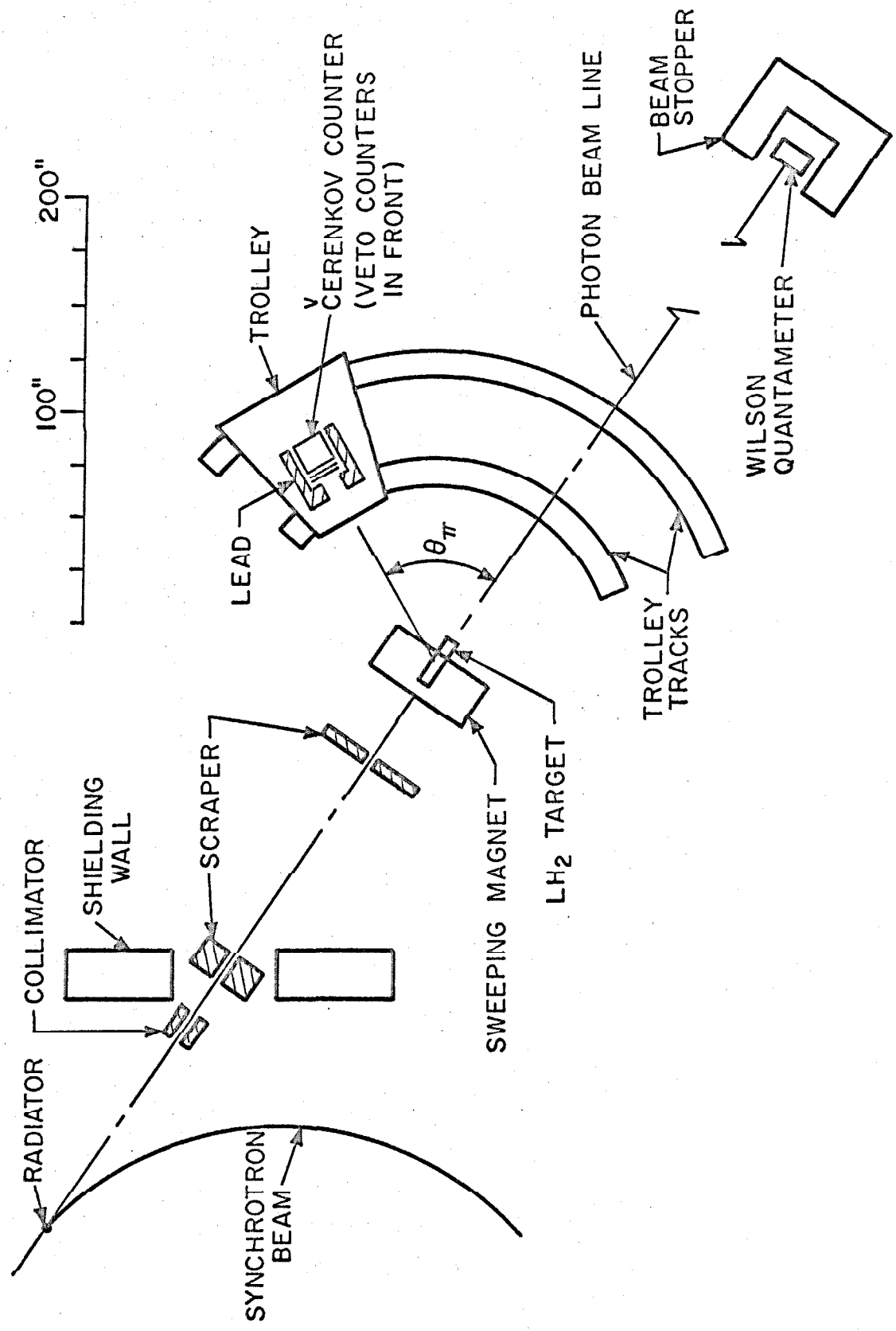

FIGURE A1: BEAM AREA LAYOUT

When viewed in the laboratory frame the directions of the two decay gamma-rays from a π^o of energy E_π form an opening angle Θ which is always greater than a minimum value $\Theta = 2 \sin^{-1} \frac{m_\pi}{E_\pi}$. At the minimum opening angle the decay is symmetric i.e., each gamma-ray makes an angle $\Theta_{min}/2$ with the direction of the decaying π^o. The angle subtended by the outside edges of the apertures of the two Čerenkov counters as viewed from the target corresponds to the minimum opening angle for some π^o energy E_π^{min}. This is the lowest energy π^o which is detectable for the counter positions since π^o's of lower energy would produce gamma-rays with larger opening angles. This cutoff in π^o meson energy corresponds to a cutoff in photon energy. The photon energy range is fixed to be $k_{min} \leq k \leq E_o$ where k_{min} is set low enough to obtain a reasonable counting rate (see Figure 4, page 14).

For this experiment the three photon energy ranges selected were:

$$700 \leq k \leq 1073 \text{ MeV}$$

$$960 \leq k \leq 1308 \text{ MeV}$$

$$1145 \leq k \leq 1513 \text{ MeV}.$$

The combined effects of the detailed structure of the bremsstrahlung beam spectrum near its endpoint energy and the low probability of detecting π^o's produced by photons near k_{min}, result in a photon energy response (Figure 3(b), page 13) which has an effective full width at half maximum of about 200 MeV. The average photon energies and effective photon energy ranges were:

$\bar{k}$	Range
911 MeV	$811 \leq k \leq 1011$ MeV
1182 MeV	$1082 \leq k \leq 1282$ MeV
1390 MeV	$1290 \leq k \leq 1490$ MeV.

At each of these energies counting rates were measured at center of mass angles ranging from 0° to 90°.

The Čerenkov counters (see Appendix B) are sensitive to all particles radiating Čerenkov light, but since particles other than electrons and gamma-rays do not initiate electromagnetic showers readily, they produce small output pulses. To veto this background of charged particles a two-counter telescope consisting of scintillators (called S_1 and S_2) was placed in front of each counter. The material in the scintillators and the paraffin absorber between them helped to keep the coincidence rates between S_1 and S_2 moderate by 1.) absorbing the large flux of low energy electrons and gamma-rays present and 2.) eliminating low energy neutrons by absorbing their knock-on protons. In addition, two scintillators were placed between the two Čerenkov counters to veto vertical moving cosmic rays.

The Čerenkov counters were placed at a nominal distance of 280cm from the hydrogen target. The apertures were built in the lead shielding wall surrounding the Čerenkov counters and varied in size from 15 to 18 cm wide by 13 to 20 cm high, while the target-aperture distance varied from 210 to 380 cm. The angular resolution was about 4 to 5 degrees full width at half maximum in the center of mass angle (see Figure 5, page 15). The glass blocks used in the

Čerenkov counters were 36 cm by 36 cm in frontal area and 30 cm (about 12 radiation lengths) deep.

The electron logic is shown in Figure 2. A pulse from the Čerenkov counter corresponding to a γ-ray with energy greater than a cutoff level (100 - 200 MeV), unaccompanied by a charged particle or cosmic ray signal is called a γ-ray. A γ-ray from each of the two Čerenkov counters is called a π^o trigger. The full width at half maximum of the delay curve for the γ-ray coincidence circuit was 12 ns. The π^o trigger initiates pulse height analysis of the two Čerenkov pulses into a two-dimensional array with coordinates E_1^γ and E_2^γ (the energies of the two decay gamma-rays). The energy of the detected π^o is $E_\pi = E_1^\gamma + E_2^\gamma$, hence all events in the region $E_1^\gamma + E_2^\gamma > E_\pi^{min}$ are in the first analysis pions produced for $k_{min} < k \leq E_o$. Those events in the region $E_1^\gamma + E_2^\gamma < E_\pi^{min}$ can be attributed mostly to the interaction $\gamma + A = A + 2\pi^o$.

B. Cross-section Calculation

To convert the counting rates to a cross-section, one works backwards and determines the counting rate expected for the energy and angular acceptance of the counters. For a given configuration of the counters and endpoint energy of the bremsstrahlung beam (E_o) the number of π^o mesons detected $n(E_\pi)$ having laboratory energy between E_π and $E_\pi + dE_\pi$ in the solid angle $d\Omega$ is given by (* implies quantity measured in center of mass system)

$$n(E_\pi)\, dE_\pi = \sigma(\theta^*)\, \frac{d\Omega^*}{d\Omega}\, Y(E_\pi)\, N(k)\, \frac{dk}{dE_\pi}\, \frac{\rho \ell}{M_p}\, dE_\pi$$

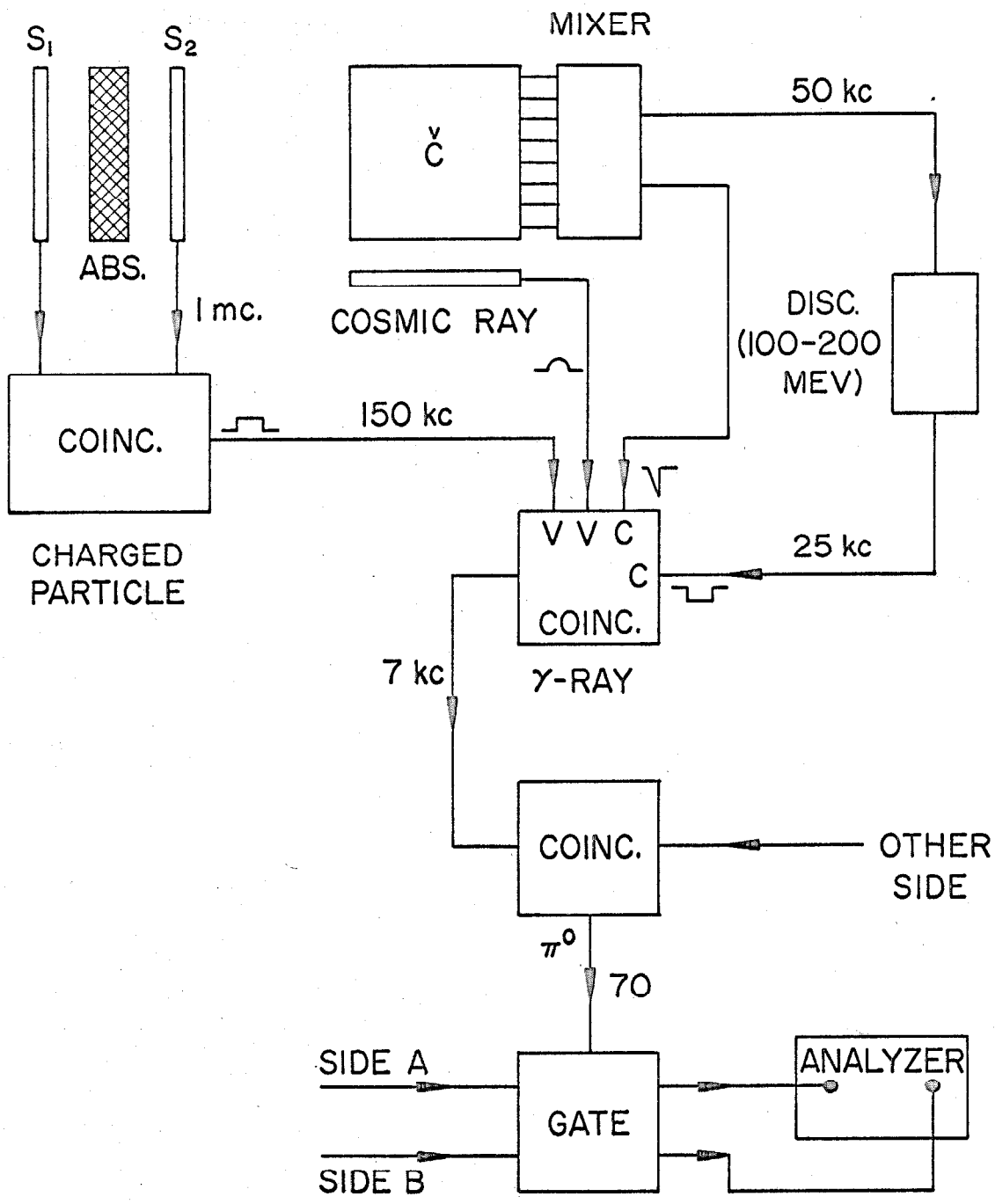

FIGURE 2: ELECTRONIC LOGIC

where:

$\sigma(\theta^*)$ = differential cross-section in center of mass.

$\frac{d\Omega^*}{d\Omega}$ = transformation of solid angle.

$Y(E_\pi)$ = effective solid angle seen by π^o of energy E_π in the laboratory frame.

$N(k)dk = \frac{Q}{k} B(\hat{k})\, dk$ = number of equivalent quanta in the photon energy range k to k + dk, where $\hat{k} = k/E_o$.

$\frac{\rho \ell}{M_p}$ = number of protons per unit cross-sectional area of the target.

For a given range of acceptance $E_1 \leq E_\pi \leq E_2$ we find the counting rate is

$$CR = \int_{E_1}^{E_2} n(E_\pi) dE_\pi.$$

Here E_2 is the energy of the π^o produced from the photon with energy $k = E_o$ and E_1 is the energy of the π^o which decays with a minimum opening angle subtended by the outer edges of the two $\check{C}$ counters.

If we assume that the cross-section is a constant in the region of the integration then we can write $CR = \sigma(\theta^*)\ \eta$ where η is called the efficiency. The counting rate is measured in $\frac{\pi^o \text{ mesons}}{\text{BIP}}$ and $\sigma(\theta^*)$ has the units μbanns, hence the efficiency η is $\frac{\pi^o \text{ mesons}}{\mu\text{barn-BIP}}$. For this experiment a BIP (Beam Integrated Pulse) = 1.097×10^{13} MeV of photons or $\frac{1.097}{E_o} \times 10^{13}$ equivalent quanta (E_o = endpoint energy (MeV) of bremsstrahlung beam).

The factor $Y(E_\pi)$ which appears in the computation of η is the effective detection solid angle which the decaying π^o of energy E_π and production angle θ_π sees due to the size and position of the apertures of the two gamma-ray detectors. $Y(E_\pi)$ is a function of the dynamics of the two decay gamma-rays and the geometry of the detectors. Talman[10] has produced an approximate analytic expression for $Y(E_\pi)$ which yields results for η which are useful for rapid computation (see Appendix D). Clinesmith[4] has developed a Monte Carlo calculation for η which in effect performs the experiment in a computer. The results from the latter program are, of course, statistical in nature. However, a method of using both the Talman and Monte Carlo results to obtain efficiencies good to about 1% is described in Appendix D.

Figure 3 is useful in describing the results of the detection efficiency calculation. Figure 3 (a) shows the high energy end of the bremsstrahlung spectrum with the photon energy cutoff shown. In Figure 3 (b) the photon energy resolution - about 200 MeV wide - is shown, its shape being determined mainly by the effective solid angle $Y(E_\pi)$. Figure 3 (c) is the $\check{C}$ counter resolution and Figure 3 (d) is the π^o energy spectrum expected in the $\check{C}$ counters. This is obtained by smearing the photon resolution Figure 3 (b) with the counter resolution Figure 3 (c).

The efficiency η is a very strong function of the photon cutoff as shown in Figure 4. In order to have a reasonable counting rate a large range of photon energies must be used. The angular

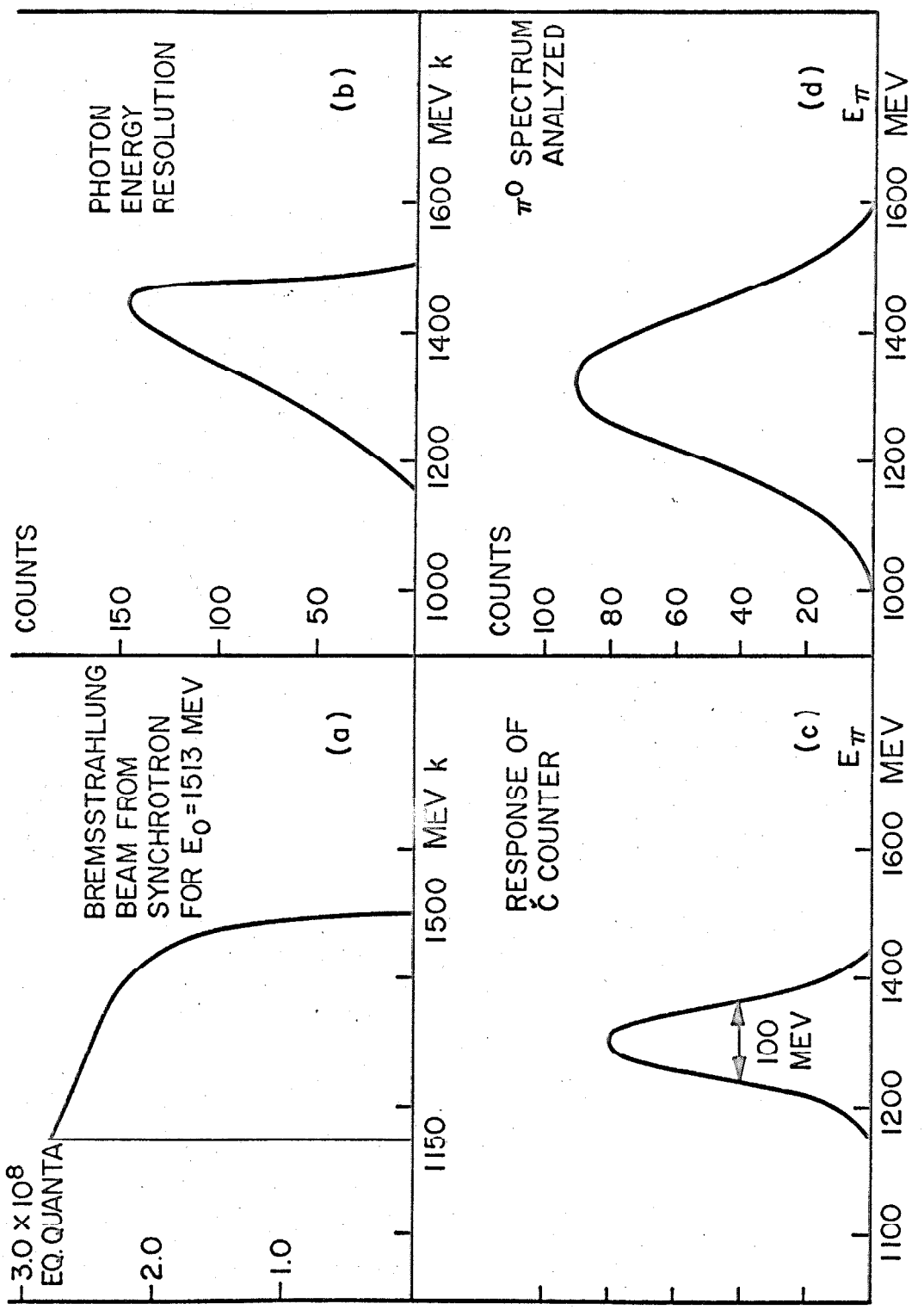

FIGURE 3: CALCULATION OF DETECTION EFFICIENCY
$\theta_{CM} = 30°$ $E_0 = 1500$ MEV

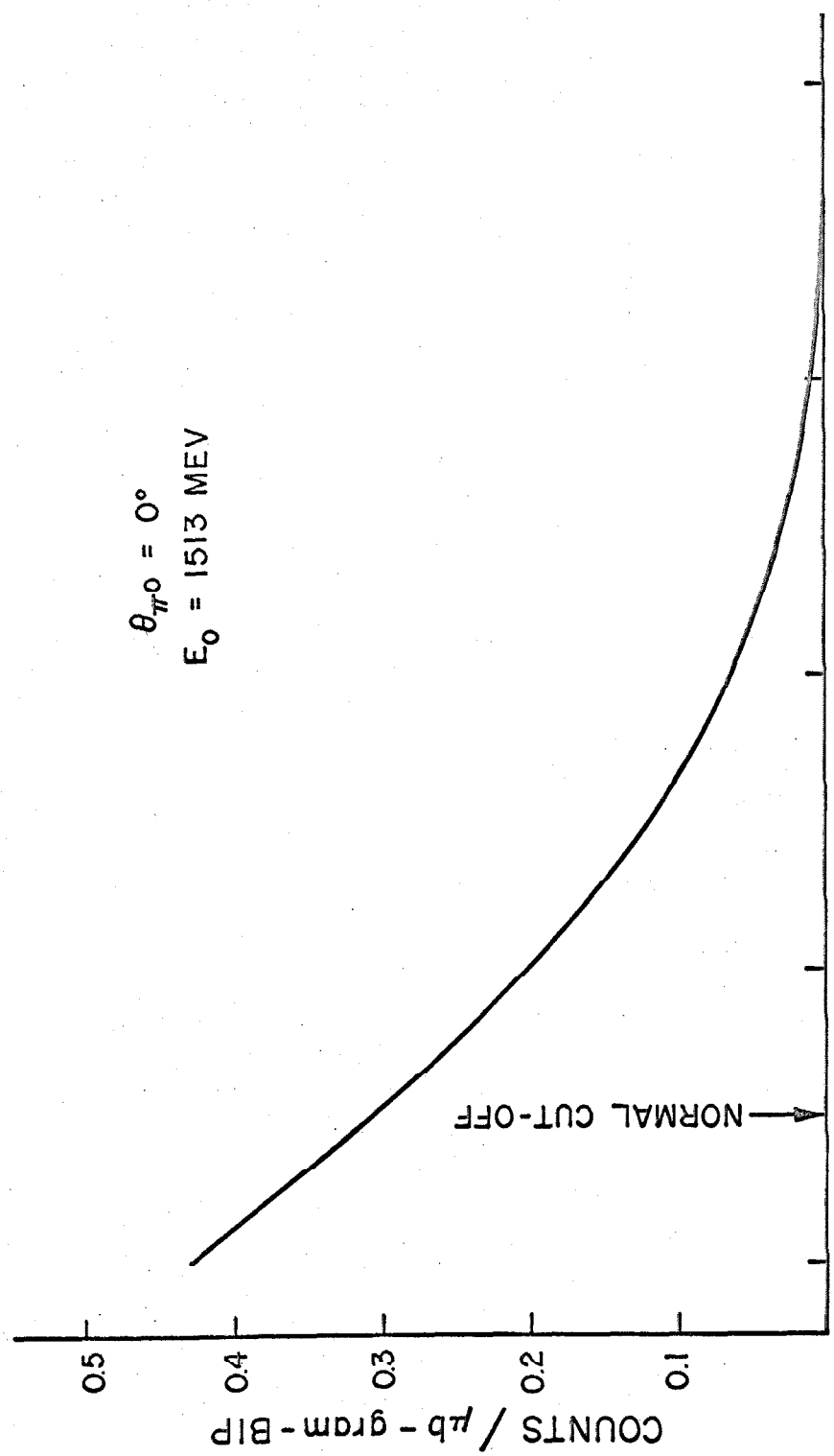

FIGURE 4: COUNTING RATE AS A FUNCTION OF PHOTON CUT-OFF ENERGY

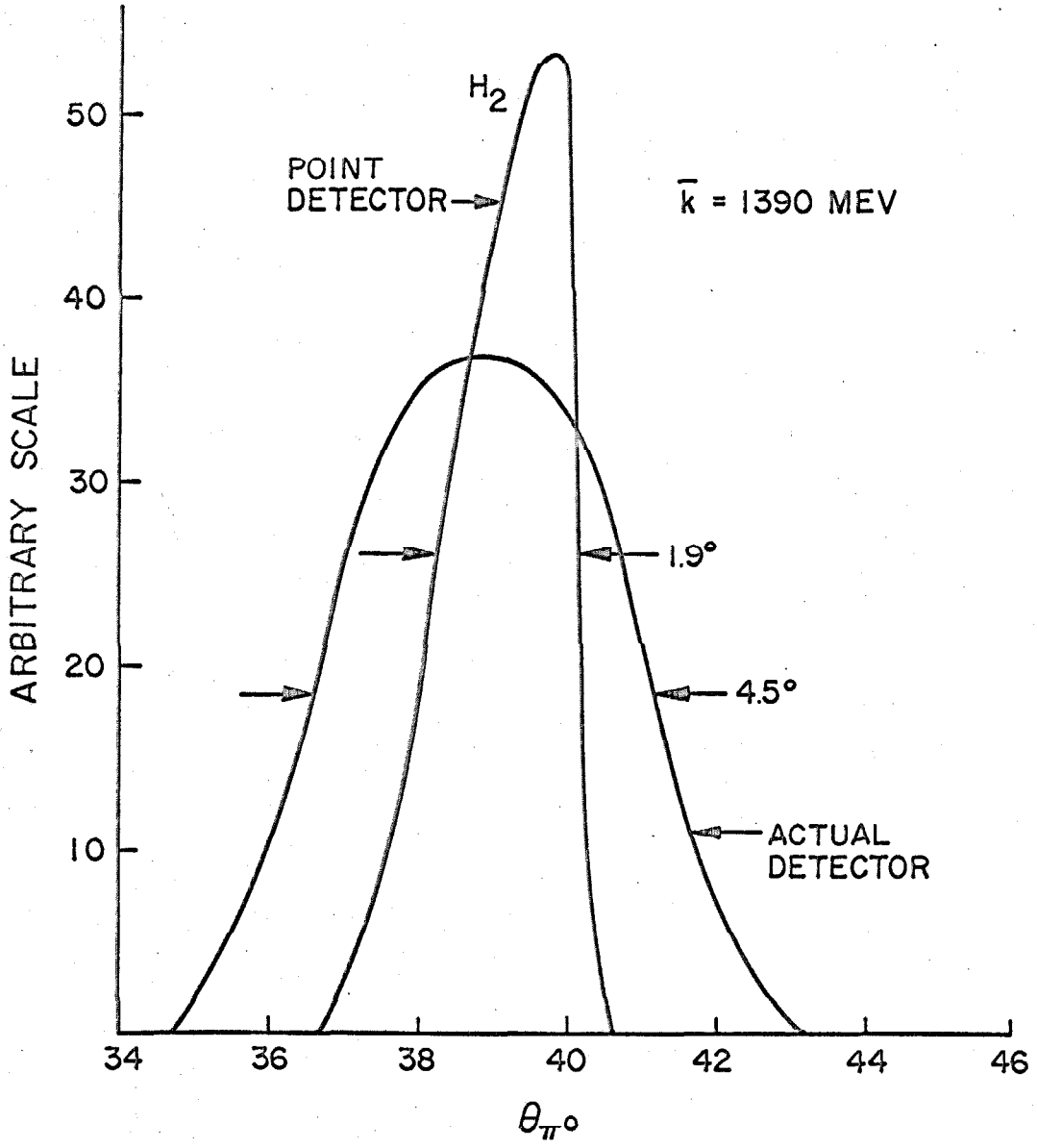

FIGURE 5: ANGULAR RESOLUTION FUNCTION

resolution is, however, quite narrow as shown in Figure 5. Typically the full width at half maximum was 4 to 5 degrees in the center of mass system.

C. Data Analysis

The analysis of the data proceeded from the output of a two-dimensional Nuclear Data pulse height analyzer. These data were in the form of a two-dimensional matrix, 32 channels on a side. One coordinate represents the energy of one decay gamma ray, the other represents the coincident gamma-ray.

Figures 6 - 9 show the π^o energy spectrum in various stages of analysis. In Figure 6 the matrix output of the two-dimensional analyzer is shown for a foreground run at $\theta_\pi = 22^o$ (Lab.) and $\bar{k} = 1182$ MeV. The two inputs of the analyzer are calibrated to have roughly the same energy scale, in this example each channel is about 45 MeV wide. To obtain the sum spectrum (π^o energy) one adds the counts along a diagonal as shown. The π^o events are in the region above the dashed line and a valley can be seen to separate these events from the huge π^o pair background. From this matrix one can also see that the events gather near the main diagonal of the matrix where the symmetrical decays reside.

Figure 7 shows the π^o energy spectrum obtained by summing along diagonals of the matrix in Figure 6. The total number of triggers was 919. The main features of the spectrum are:

(1) a valley at channel 18-19 which lies at about 850 MeV

(2) a huge background below this valley, due mainly to π^o pairs, which

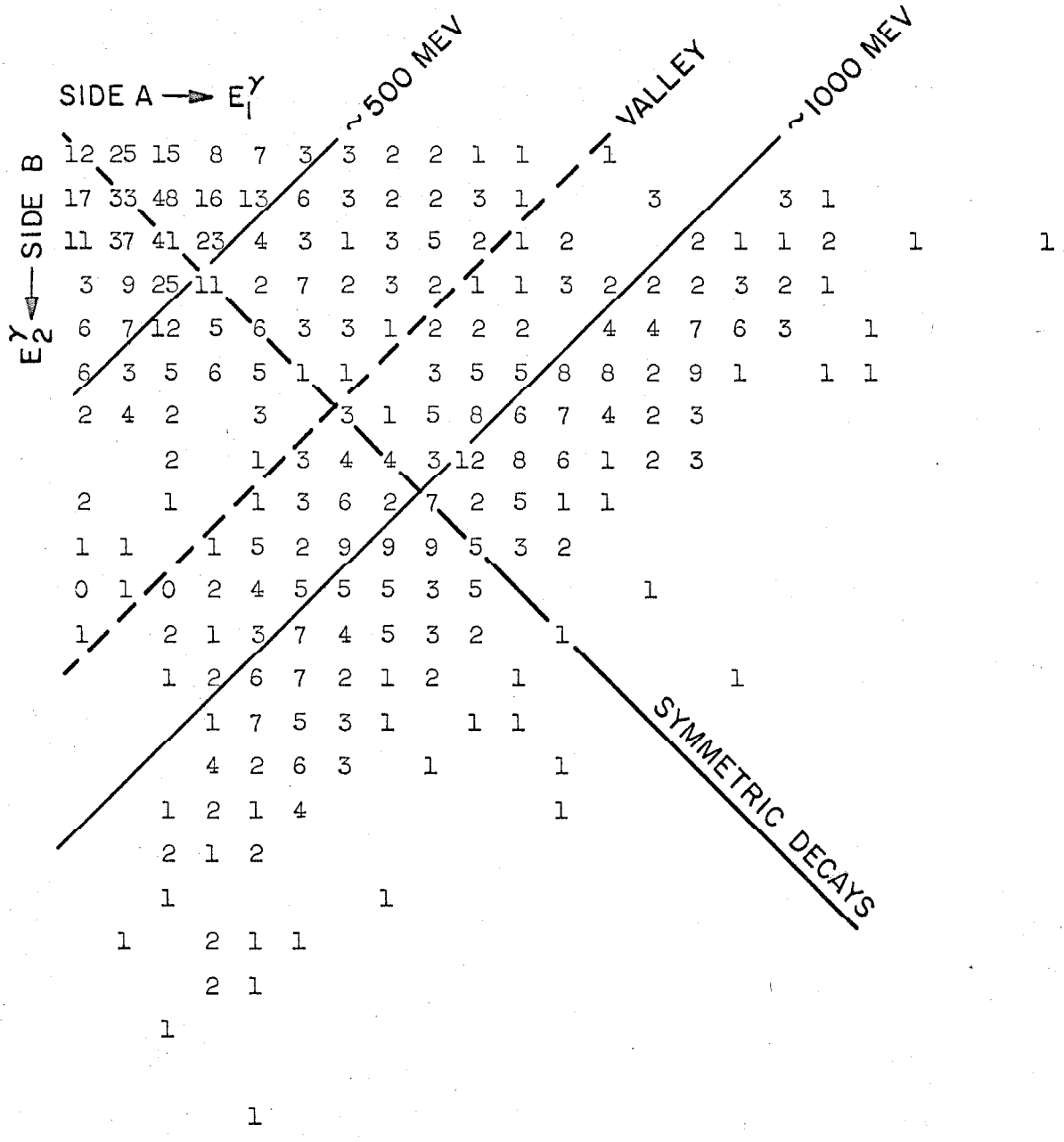

32 × 32 CHANNELS (ZEROS SUPPRESSED)

FIGURE 6: OUTPUT OF 2-DIMENSIONAL PULSE HEIGHT ANALYZER $\bar{k}$ = 1182 MEV θ_π = 22°

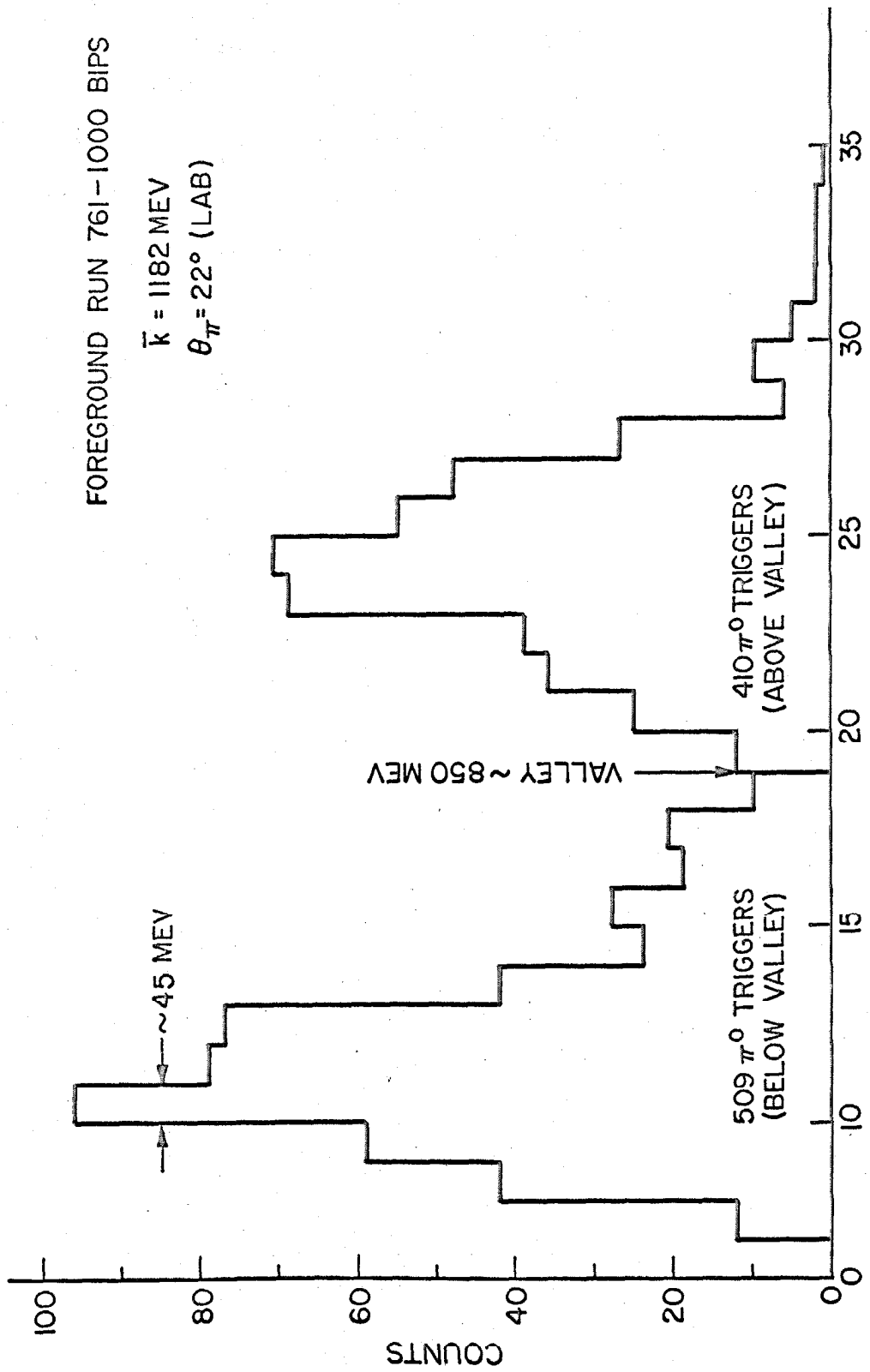

FIGURE 7: SUM SPECTRUM FROM UNCALIBRATED MATRIX

is cut off at the low energy end by the energy discrimination on single γ-rays

(3) a peak above the valley which contains π^o mesons.

The second stage of analysis involves an energy calibration of the original matrix, assuming we know the calibration exactly. We then obtain a second matrix using 20 or 25 MeV bin widths. The narrower bins result from interpolation and do not contain any resolution information not contained in the original wide bins. If we sum the diagonals of this matrix we get the energy spectrum shown as the solid histogram in Figure 8. Just the spectrum above 350 MeV is shown so that the low energy cutoff cannot be seen. The calibration has been adjusted so that the mean energy of the events above the valley (called π^o events) is the same as the computed value for a flat cross-section. The geometric cutoff, including smearing due to counter resolution, should be at 825 MeV.

The dashed histogram is the sum of accidentals and empty target runs for the same amount of photon beam. The background has the same general character at low energy as the full target spectrum without the large π^o peak. For this example there are 32 π^o triggers from the empty target runs and 11 π^o triggers due to accidental coincidences. There is roughly 0.05 - 0.10 grams of material due to the mylar end caps on the target and the air path in the photon beam during empty runs, compared to about 1.25 grams during full target runs so the 32 empty target versus 413 foreground π^o events is reasonable. The fact that the below cutoff events for foreground and

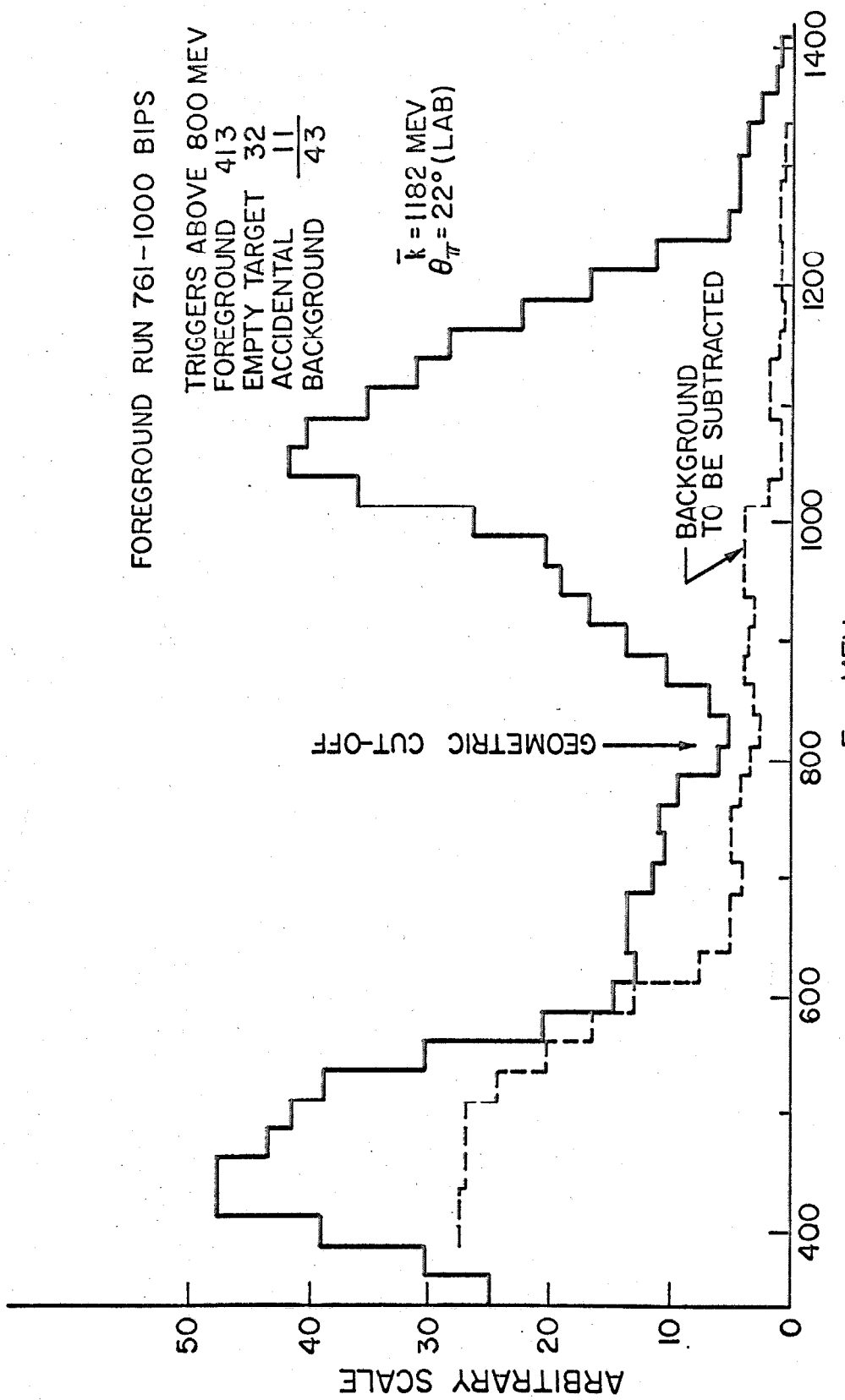

FIGURE 8: SUM SPECTRUM FROM RECALIBRATED MATRIX

background are not in the same ratio as above can probably be explained by differences in coherent π^o pair and single π^o production in the mylar end caps and air. Also, π^o pairs produced in the air close to the counters have a larger efficiency of detection than single π^o's produced at the same spot.

Other foreground runs at this same angle are added to produce the background subtracted spectrum shown in Figure 9. Here the π^o spectrum computed by the Monte Carlo efficiency is shown for comparison. The error bars on the Monte Carlo calculation are not shown on the figure but are purely statistical.

The fit is excellent at all places except near the cutoff. At cutoff the background subtracted spectrum does not quite vanish and near the cutoff the measured spectrum appears to be significantly higher implying either the cross-section is in a region of rapid change or we are seeing the effects of π^o pair production. The latter is the more likely case.

Since one purpose in this experiment was to unfold the photon energy dependence of the π^o photoproduction cross-sections, we must know the π^o energy spectrum very well. In order to calibrate the $\check{C}$ counters, the following scheme was used.

The $\check{C}$ counters were calibrated in a monoenergetic electron beam whose energy calibration was know to about 2%. To check the energy calibration on a daily basis, it was decided to use the 50% point in the integrated spectrum (called the peak) of cosmic rays measured by the $\check{C}$ counters. This was done whenever the experi-

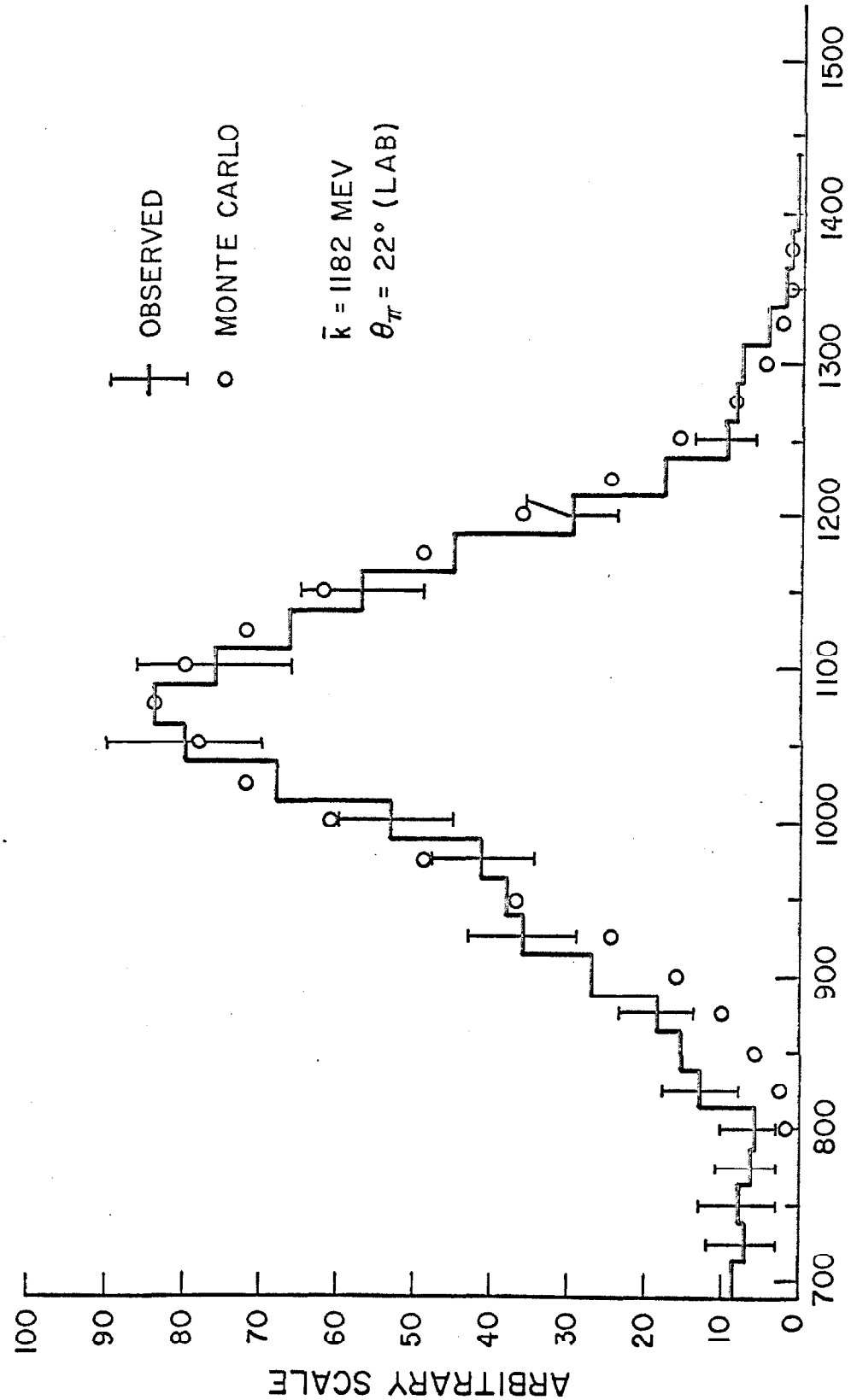

FIGURE 9: BACKGROUND SUBTRACTED SUM SPECTRUM

ment was not being run. From the electron beam measurements the cosmic ray peak was found to be equivalent to a 220 MeV electron. Using this energy equivalent and the location of the peak, the daily energy calibration for the two-dimensional matrix could be determined. Unfortunately, the energy calibration did not remain constant from day to day, but fluctuated by as much as 5% in an unexplained way. With this variation in the measured energy calibration unfolding the energy dependence of the cross-section would be quite undependable.

To test the absolute energy calibration the measured π^o spectra were used. The energy spectra expected for the π^o's at the various angles and energies were computed using a flat cross-section. The mean energy of the measured π^o spectrum was compared with that of the computed π^o spectrum. This was done for all the foreground runs in the experiment and the best value for the cosmic ray energy calibration on each day was chosen. This value was generally different from that derived from the daily cosmic ray distribution and the monoenergetic electron beam. There was an average systematic error corresponding to about a 2% shift in the π^o energy scale with 2% fluctuations. The systematic shift could be easily compensated for, but the 2% fluctuation ruined any hope of making an energy calibration using the π^o energy spectra themselves. This can be seen by computing the shift in the mean energy of the π^o energy spectrum as a function of the slope in the cross-section. Clearly the slope must be great enough to cause a shift in $\bar{E}_\pi$ greater

than the uncertainty in $\bar{E}_\pi$.

We fold a cross-section of the form

$$\sigma = A + B\,(E_\pi - \bar{E}_\pi)$$

into the flat cross-section π^o spectrum and find the change in the mean of this distribution. It is found to be displaced by

$$\Delta\bar{E}_\pi = \frac{B\Gamma^2}{\sigma}$$

where Γ^2 = second moment of the energy spectrum. For this experiment $\sigma \simeq .1$ μb and $\Gamma \simeq 70$ MeV. The error in the calibration is given above as 2% or 20 MeV at 1000 MeV so the slope in the cross-section must be

$$B \geq \frac{\Delta\bar{E}_\pi \cdot \sigma}{\Gamma^2} = 0.4\ \mu b/100\ \text{MeV}$$

However, slopes of only 0.1 μb to 0.3 μb per 100 MeV were observed in the measured cross-sections.

It appears unfolding would not work for two interconnected reasons. First, the calibration could not be measured in an absolute way without reservation. Second, any attempts to glean the calibration from the data would negate any attempts at unfolding because the uncertainties in the energy calibration of the spectra would mask the energy dependence of the cross-section.

It is interesting to note that even if the calibration were known exactly, we would have been limited ultimately by counting statistics. For 1000 counts in a spectrum (our spectra had between 200-800 counts) one knows that the mean is measured only to within

$\Delta \bar{E}_\pi = \frac{\bar{E}_\pi}{\sqrt{1000}}$ or $\Delta E_\pi \simeq$ 30 MeV at $\bar{E}_\pi$ = 1000 MeV. This is equivalent to a slope in the cross section of about 0.5 μb/100 MeV (from formula above).

A program prepared before data was available was used to check these conclusions. The output of this program was a polynomial fit to σ(k). This proceeded as follows:

1. Adjust the energy calibration to make the mean energy of the measured π^o energy spectrum the same as that of the computed π^o energy spectrum noting the required calibration parameters.
2. Fit the measured π^o energy spectrum to a cross-section of the form $\sigma(k) = A + B(E_\pi - \bar{E}_\pi)$.
3. Recompute the expected π^o energy spectrum using this cross-section and readjust the $\bar{E}_\pi$ of the measured spectrum.
4. Fit again expecting B to be zero.

The results were:

a. The energy calibration is known to ± 2% corresponding to an error of about 20 MeV in $\bar{E}_\pi$.
b. B has an error equal in magnitude to itself, consequently when iteration is performed B does not change.

An example of this result can be seen by trying to fit the spectrum in Figure 9. Two kinds of photon energy fits are made to this particular π^o energy spectrum. First, the cross-section is expanded in a power series of the form

$$\sigma(k) = \sum_{n=0}^{N} A_n (E - \bar{E}_\pi)^n$$

where $\bar{E}_\pi$ is the average energy in the π^o spectrum. In the fit the flat cross-section efficiency is modified by the energy dependence of $\sigma(k)$. A fit is first made with only A_o. This gives the average cross-section for the photon energy range being measured but has the advantage that the structure of the measured π^o spectrum is being used rather than just the number of π^o's contained in it. A_o always agreed very well with the average cross-section computed by dividing the π^o counting rate by the efficiency η; therefore the later numbers (which are more convenient to calculate) are used in our cross-section results. A fit is next made letting N = 1 from which the slope of the cross-section is found. Unfortunately the results are sufficiently uncertain to negate any need for including higher powers of $(E_\pi - \bar{E}_\pi)$.

The second type of fit is referred to as "bin" fitting. In this method the photon energy range is cut up into intervals in which the cross-section is taken to be flat. Two fits were made, one used one bin, the other used two bins.

Results for both the polynomial and "bin" fitting are given in the table following. A second series of fits is attempted replacing the flat cross-section used in the first set of fits by the cross-section found in the first polynomial fit.

Energy Fits to Cross-section

Polynomial Fit

N	A_o(μb)	A_1(μb/100 MeV)	$P(\chi^2)$
0	1.56 (± 0.07)	0	0.49
1	1.56 (± 0.07)	1.91 (± 2.00)	0.50
Refit with σ =	$1.56 + 1.91 (E_\pi - \bar{E}_\pi)$		
0	1.56 (±0.07)	0	0.46
1	1.56 (± 0.07)	1.91 (± 2.10)	0.46

Bin Fit

N	Bin 1	Bin 2 (higher k)	
0	1.56 (± 0.07)		0.49
1	0.15 (± 0.08)	2.37 (± 0.14)	0
Refit with σ =	$1.56 + 1.91 (E_\pi - \bar{E}_\pi)$		
0	1.56 (± 0.07)		0.46
1	0.28 (± 0.09)	2.30 (± 0.14)	0

III. RESULTS

Three angular distributions were measured and are plotted in Figures 10, 11 and 12. The kinematic parameters for these distributions are given in Table 1. Each angular distribution is the average over a photon energy interval of about 200 MeV centered on the mean photon energy $\bar{k}$ given for each curve. The points are plotted for the average acceptance angle of the counter apertures and were set at about 10° intervals in the CMS except at the zero degree setting where the average center of mass angle was near 3.5°. The Table G1 contained in Appendix G gives the counting rate data. Table 2 gives the cross-sections as well as the efficiencies used to compute them.

The $\bar{k}$ given for a particular angular distribution is the average of those computed at the various angles in the angular distribution. Again it should be noted that the cross-section reported is an average over a large interval of about 200 MeV so that a 10 MeV variation in the central photon energy as a function of center of mass angle is insignificant. From Figure 3(b) one can see how the photon resolution function weights the photons in the acceptance interval.

Plotted with the results of this experiment are data from several sources. Some of these other data are used to compare with our results while the rest are used to help fill out the backward angles where our method is not useful. The data which can be compared directly are those of Talman[10] taken with the same equipment at roughly the same photon energy intervals, and recent data of

Brannschweig et al.[9] from Hamburg. The agreement with Talman's data is excellent except at $\bar{k}$ = 911 MeV where large error bars on his data prohibit careful scrutiny. The Hamburg data at $\bar{k}$ = 1360 MeV agree reasonably well with the results of our data at $\bar{k}$ = 1390 MeV. The results of Diebold[5], Alvarez et al.[7], and the preliminary results of Wolverton[6] have higher resolution than this experiment. Their measured cross-sections are assumed to be correct and are folded into our efficiency calculation to obtain the counting rate (C.R.), which we would have measured. The cross-section is then computed in the normal way σ = C.R./η. This value of the cross-section is plotted on our graphs for comparison. We agree well with Diebold but find some disagreement with Alvarez et al. at 90° for $\bar{k}$ = 1390 MeV. For completeness the value of the cross-section at the average photon energy is plotted when it differs significantly from the value with this experiment's resolution folded in. This condition exists only at 60° and 120° for $\bar{k}$ = 911 MeV where the differential cross-section, as measured by Diebold, has local minima. Details concerning corrections to the measured cross-sections due to curvature in $\sigma(\theta, k)$ are given in Appendix D, part c, page 83.

The errors shown on the graphs are due to the random errors incurred in counting rates and errors in determining the proper energy cutoff in the π^o energy spectra. Other random errors due to positioning the counters before each run, setting and maintaining the endpoint energy of the synchrotron, and beam monitoring have

each been estimated to be less than 1%. A systematic error of about 2% is introduced by the measuring error in fixing the lower photon energy cutoff. Finally, a systematic error of no more than 4% due to an uncertainty in the machine energy calibration is present in the data. Both systematic errors lead to a normalization error in the cross-sections.

Table 1

Kinematics Table

$\bar{k}$	(MeV)	911	1182	1390
E_o	(MeV)	1073	1308	1513
k_{min}	(MeV)	700	950	1150
Parameters computed at mean photon energy				
k	(MeV)	526	625	693
W	(MeV)	1609	1760	1868
q	(MeV)	508	610	680
q_o	(MeV)	526	625	693
β_π		0.966	0.976	0.981
-t	(GeV^2)			
	0^o	0.31×10^{-3}	0.22×10^{-3}	0.18×10^{-3}
	60^o	0.27	0.38	0.47
	120^o	0.80	1.14	1.42
	180^o	1.07	1.53	1.89
Location and residue at 788 MeV vector meson pole computed for unit coupling constants.				
Cos θ_o		2.16	1.81	1.66
Residue (μbarn)		-6.20	-5.47	-4.99

k = Photon energy
W = Total center of mass energy
q = Pion momentum
q_o = Pion total energy
$\beta_\pi = q/q_o$
-t = Transverse momentum squared

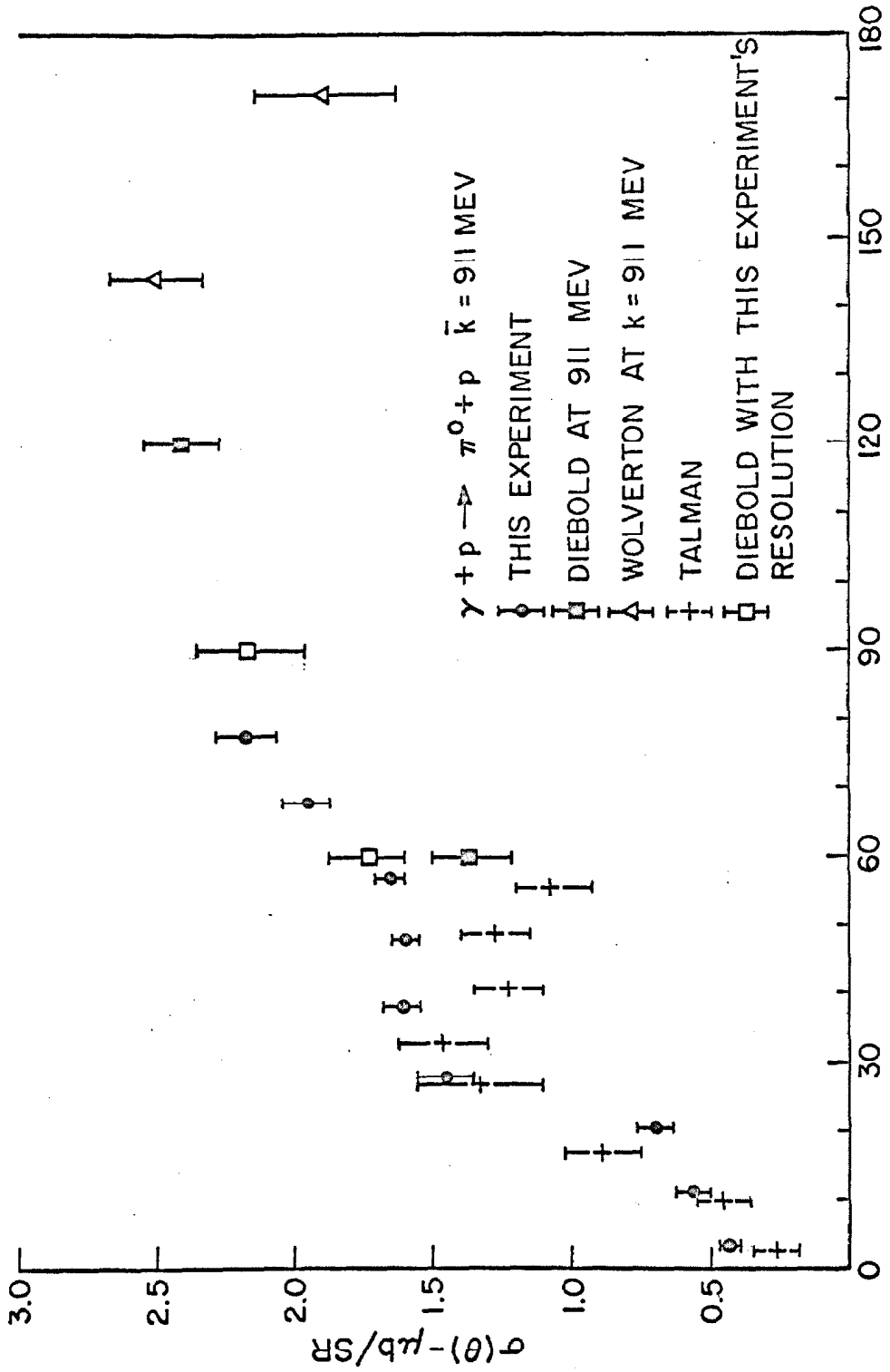

FIGURE 10: π^0 PHOTOPRODUCTION CROSS-SECTION $\gamma + p \rightarrow \pi^0 + p$ NEAR $\bar{k}$ = 911 MEV

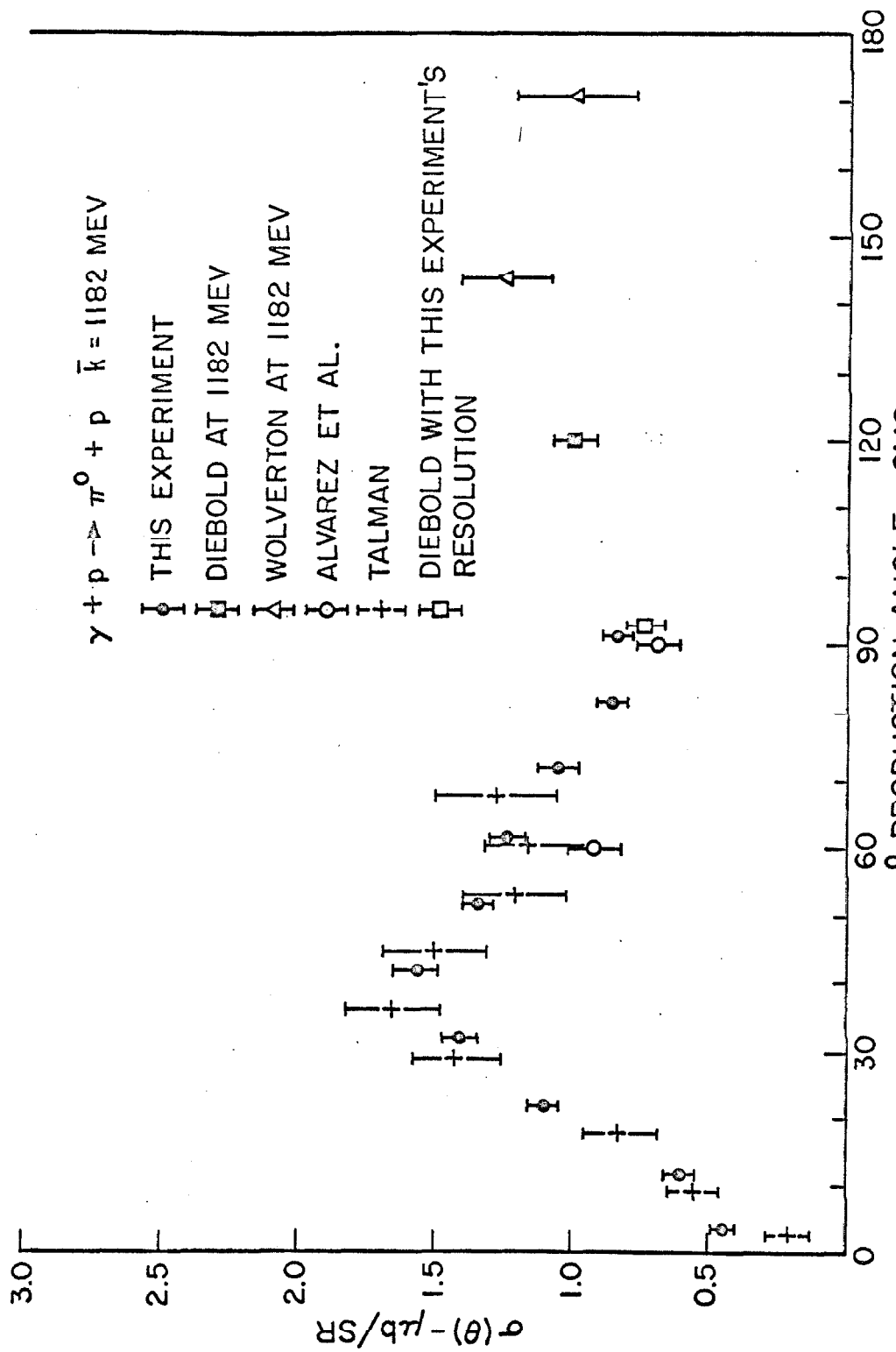

FIGURE II: π^0 PHOTOPRODUCTION CROSS-SECTION $\gamma + p \rightarrow \pi^0 + p$ NEAR $\bar{k} = 1182$ MEV

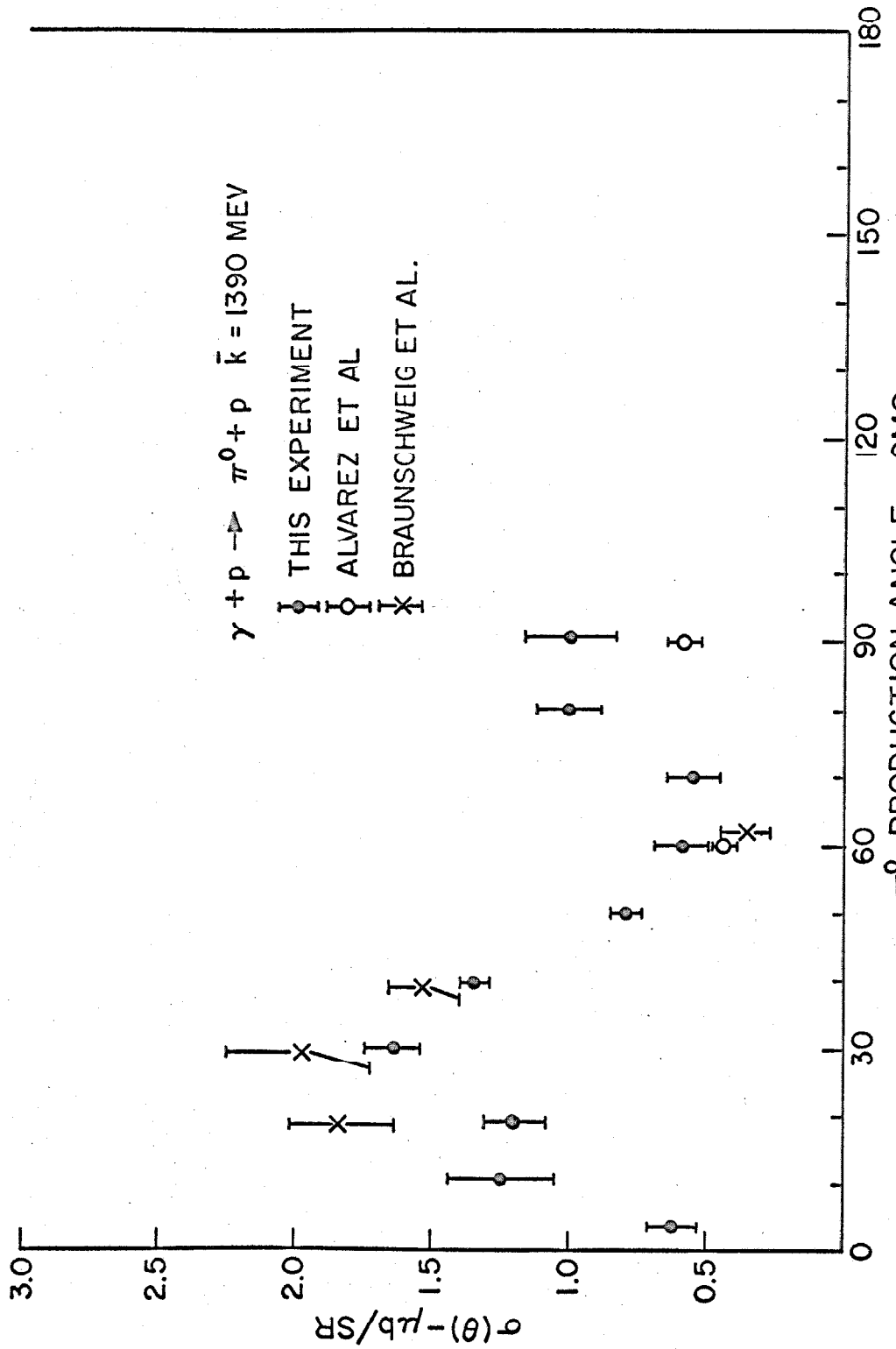

FIGURE 12: π^0 PHOTOPRODUCTION CROSS-SECTION $\gamma + p \rightarrow \pi^0 + p$ NEAR $\bar{k} = 1390$ MEV

Table 2

Cross-section Data

$\bar{k}$ = 911 MeV

Angle LAB	Angle C M	Mean K	Det Eff η	Counting Rate(error)	Cross Section Microbarns/Sr.
0.	3.5	924	0.625	0.278(.023)	0.445(.037)
5.0	11.2	923	0.606	0.343(.036)	0.566(.060)
10.0	20.3	924	0.565	0.395(.044)	0.700(.077)
15.0	28.0	915	0.534	0.780(.055)	1.461(.103)
21.0	38.1	923	0.671	1.076(.056)	1.603(.083)
28.0	47.9	906	0.611	0.995(.037)	1.629(.061)
35.0	57.4	892	0.520	0.873(.035)	1.678(.067)
42.0	67.3	893	0.374	0.733(.031)	1.959(.083)
49.0	77.5	897	0.247	0.534(.026)	2.164(.106)

$\bar{k}$ = 1182 MeV

Angle LAB	Angle C M	Mean K	Det Eff η	Counting Rate(error)	Cross Section Microbarns/Sr
0.	3.7	1168	0.344	0.158(.015)	0.459(.043)
5.0	11.4	1165	0.337	0.202(.021)	0.599(.062)
11.0	21.4	1171	0.304	0.337(.018)	1.110(.058)
17.0	31.9	1175	0.263	0.372(.014)	1.415(.053)
23.0	41.8	1176	0.224	0.349(.013)	1.557(.057)
28.0	51.6	1183	0.227	0.309(.015)	1.362(.067)
35.0	61.6	1194	0.158	0.196(.011)	1.241(.069)
42.0	72.0	1195	0.147	0.152(.010)	1.031(.066)
49.0	81.6	1194	0.117	0.102(.007)	0.868(.062)
56.0	91.0	1196	0.090	0.079(.006)	0.883(.062)

$\bar{k}$ = 1390 MeV

Angle LAB	Angle C M	Mean K	Det Eff η	Counting Rate(error)	Cross Section Microbarns/Sr
0.	3.1	1387	0.200	0.124(.021)	0.621(.103)
5.0	10.5	1390	0.182	0.226(.039)	1.243(.213)
10.0	19.6	1385	0.411	0.499(.042)	1.214(.102)
15.0	29.6	1385	0.375	0.622(.045)	1.658(.120)
21.0	39.2	1391	0.333	0.451(.031)	1.356(.093)
26.0	49.6	1394	0.253	0.203(.020)	0.804(.078)
32.0	60.3	1391	0.203	0.120(.019)	0.592(.092)
39.0	70.2	1391	0.158	0.084(.013)	0.534(.082)
46.0	80.8	1394	0.106	0.104(.013)	0.981(.122)
53.0	90.7	1391	0.083	0.082(.014)	0.984(.167)

IV. INTERPRETATION OF RESULTS

We shall try to interpret our results in terms of the cross-section resulting from the exchange of a neutral vector meson X^o of mass greater than the π^o. The two obvious candidates are the ω^o and ρ^o.

$\Gamma(X^o \to \pi^o + \gamma)$

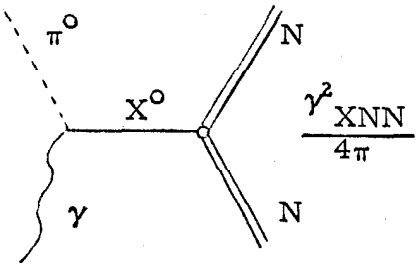

$$\frac{\gamma^2_{XNN}}{4\pi}$$

The cross-section computed using this diagram is (center of mass system)

$$\sigma(\theta) = \Gamma(X^o \to \pi^o + \gamma)\,\frac{\gamma^2_{XNN}}{4\pi}\cdot\frac{9}{M_X^3}\cdot\frac{q}{k}\cdot\frac{1}{\left(1-\left(\frac{M_\pi}{M_X}\right)^2\right)^3\left(\cos\theta-\cos\theta_o\right)^2}\cdot$$

$$\left\{\sin^2\theta+\frac{\Delta^2}{2W^2\beta^2}\left[(1+\alpha)^2(1-\beta\cos\theta)^2+\frac{\alpha^2\beta^2W^2\sin^2\theta}{2M_N^2}\right]\right\} \qquad (1)$$

where

$\Delta^2 = 2kq_o(1-\beta\cos\theta) - m_\pi^2$

W = total center of mass energy

q = π^o momentum

q_o = π^o energy

k = photon energy

$\beta = q/q_o$

θ_o = location of the pole in unphysical region - evaluated by setting $\Delta^2 = -M_X^2$.

The XNN vertex has been taken to be

$$\left[\sqrt{3}\,\gamma_{X\,NN}\,\bar{u}(p')\,\gamma_\mu\,u(p) + \frac{\sqrt{3}\,\gamma_{X^oNN}^{\alpha}}{4M_N}\,\bar{u}(p')\,(\not{\Delta}\,\gamma_\mu - \gamma_\mu\not{\Delta})\,u(p)\right]\epsilon_\mu,$$

where $\Delta = p - p'$, ϵ_μ = polarization vector of the vector meson, and p and p' are the initial and final momenta of the nucleon. At the $\pi^o\gamma X^o$ vertex we have

$$\left[\Gamma(X^o \to \pi^o + \gamma)\,\frac{96\pi}{M_X^3\left(1 - \frac{M_\pi^2}{M_X^2}\right)^3}\right]^{\frac{1}{2}} \cdot \epsilon_{\alpha\beta\gamma\delta}\,k_\alpha\eta_\beta\epsilon_\gamma r_\delta$$

where η_β is the polarization vector of the photon and r_δ is the 4 momentum of the X^o meson.

The number α is a measure of the anamolous magnetic moment of the X^o. For small angles the cross-section is dominated by the $\sin^2\theta$ term so that the value of α doesn't matter. The residue at the pole for our energies is very insensitive to the value of α varying by only 5% when α is changed from 0 to 1. The biggest effect of α is in the shape of the cross-section at backward angles. This is illustrated in the figure below where the cross-section for the pole term is shown for unit coupling constants.

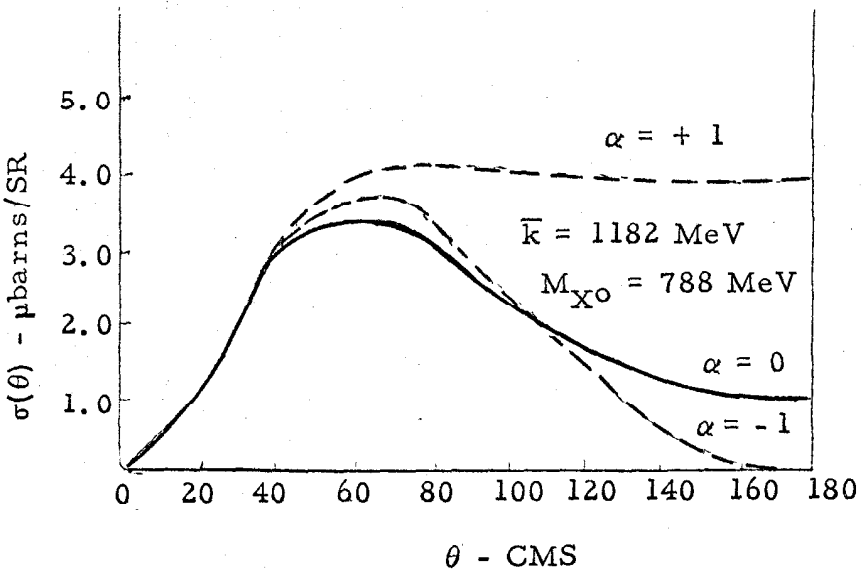

The parameter to be evaluated by our fitting procedure will be the product $\Pi = \Gamma(X^\circ \to \pi^\circ + \gamma) \frac{\gamma^2_{XNN}}{4\pi}$. Since a cursory examination of our data shows that a fit by just the pole term will be impossible and recalling that we are in the vicinity of second, third and fourth nucleon resonances where large backgrounds are to be expected, we are forced to use the Moravscik[2] fitting procedure. To do this we write the cross-section as a pole term plus resonances with a term containing the interference between them. For this calculation α will be taken to be zero (for want of evidence to the contrary) and the resonances will be contained in a polynomial term. Then the cross-section is

$$\sigma(\theta) = \frac{G(\theta)}{(\cos\theta - \cos\theta_o)^2} + \frac{A(\theta)}{(\cos\theta - \cos\theta_o)} + \sum_{n=0}^{N} C_n \cos^n\theta .$$

Here the first term is the X^o pole. Multiplying by $(\cos\theta - \cos\theta_o)^2$ we have

$$(\cos\theta - \cos\theta_o)^2\sigma(\theta) = C(\theta) + A(\theta)(\cos\theta - \cos\theta_o) + (\cos\theta - \cos\theta_o)^2\sum C_n\cos^n\theta$$

which can be rewritten as

$$(\cos\theta - \cos\theta_o)^2\,\sigma(\theta) = \sum_0^N A_n\cos^n\theta\,. \qquad (2)$$

This is the fit we make to the data. For a no pole fit we merely expand $\sigma(\theta)$ in powers of $\cos\theta$. Evaluating Equation (2) at the pole we obtain

$$(\cos\theta - \cos\theta_o)^2\,\sigma(\theta)\Big|_{\theta=\theta_o} = G(\theta_o) = \sum_0^N A_n\cos^n\theta_o$$

and from $G(\theta_o)$ we extract the value of the coupling constants.

There are two points that must be remembered when interpreting the results from Moravcsik fits to cross-section data. First, two additional powers of $\cos\theta$ are introduced when multiplying the cross-section by $(\cos\theta = \cos\theta_o)^2$. Hence the highest power of $\cos\theta$ needed to fit the cross-section apart from those contributed by the pole term is N-2 (Eq. 2). Secondly, the Moravcsik coefficients A_n are not simply related to the background coefficients C_n.

We have made fits to our data using M_{X^o} = 788 MeV at $\bar{k}$ = 911, 1182, and 1390 MeV. The highest power of $\cos\theta$ used in a fit is N. The quantity $\Pi = \Gamma(X^o \to \pi^o + \gamma)\,\frac{\gamma_{X^oNN}}{4\pi}$ has been evaluated for the various fits. The criteria for deciding when a fit exists as N is increased are (1) a sharp break in χ^2, while at the same time (2) the quantity $\rho^2 = \frac{\text{chi squared}}{\text{number of degrees of freedom}}$ (plotted in

Figures 13, 14, and 15) starts its gradual increase.

Table 3 summarizes the results of making Moravcsik fits to the data. Whenever possible backward angle data are added to our forward angle results to keep the fit from becoming unrealistic at the backward angles. Data at backward angles are not available above $\bar{k}$ = 1200 MeV so for our highest angular distribution at $\bar{k}$ = 1390 MeV we have used mild constraints in the form of $\sigma(\theta) = 1.0 \pm 1.0$ at 90°, 120°, 150° and 180°.

Figures 13, 14 and 15 show Π as a function of the highest power of cos θ used in the fit for a mass 788 MeV pole. Also, the statistical parameter ρ^2 is plotted for fits using three different masses for the exchange meson and for no pole.

We can make some observations on the basis of these three figures.

(1) When a pole diagram with a vector meson is used in fitting the data no powers of cos θ greater than four are ever needed. (See Figures 16, 17 and 18.) The fits at 911 MeV and 1390 MeV are poor due to peculiarities in the measured cross-section. At 20° and 30° for $\bar{k}$ = 911 MeV the measured cross-section has a very sharp knee. If the chi-square contributed by these two points is reduced to just 2 (allowing point to miss the fitting curve by only one sigma) the $P(\chi^2)$'s are increased by about a factor of five. At $\bar{k}$ = 1390 MeV the cause of the poor fit is the step at 10° and 20°.

(2) The value of Π when determined using the mass 788 MeV pole

Table 3

Fit to $(\cos\theta - \cos\theta_o)^2 \sigma(\theta) = \sum_{n=0}^{N} A_n \cos^n\theta$

M_X = 788 MeV

$\bar{k}$ = 911 MeV 13 points total

$\cos\theta_o$ = 2.16

N	χ^2	Π	$P(\chi^2)$	No Pole χ^2	No Pole $P(\chi^2)$
2	42.1	0.27 (.02)	0	77.4	0
3	39.9	0.48 (.14)	0	59.4	0
4	22.3	2.86 (.59)	1.8%	33.8	0
5	21.1	5.30(2.24)	1.5%	25.3	0.8%
6	20.9	8.60(9.30)	1.2%	17.3	2.4%
7	14.2	Negative	3.2%	16.8	1.8%

$\bar{k}$ = 1182 MeV 13 points total

$\cos\theta_o$ = 1.81

				No Pole	
2	13.1	0.27 (.02)	0	358	0
3	15.6	0.76 (.06)	9.5%	154	0
4	3.4	1.39 (.18)	90%	33.9	0
5	3.1	1.07 (.55)	87%	8.8	28%
6	2.9	1.90(1.98)	82%	3.8	70%
7	2.8	0.83(6.16)	75%	3.0	70%

$\bar{k}$ = 1390 MeV 10 points total

$\cos\theta_o$ = 1.66

				No Pole	
2	90.0	0.08 (.03)	0	92.8	0
3	52.8	0.57 (.09)	0	92.2	0
4	11.6	1.99 (.24)	6.0%	51.4	0
5	8.9	3.29 (.79)	8.5%	20.5	1%
6	8.1	1.82(2.00)	6.2%	7.4	13%
7	6.8	-5.33(6.62)	5.0%	6.9	9%

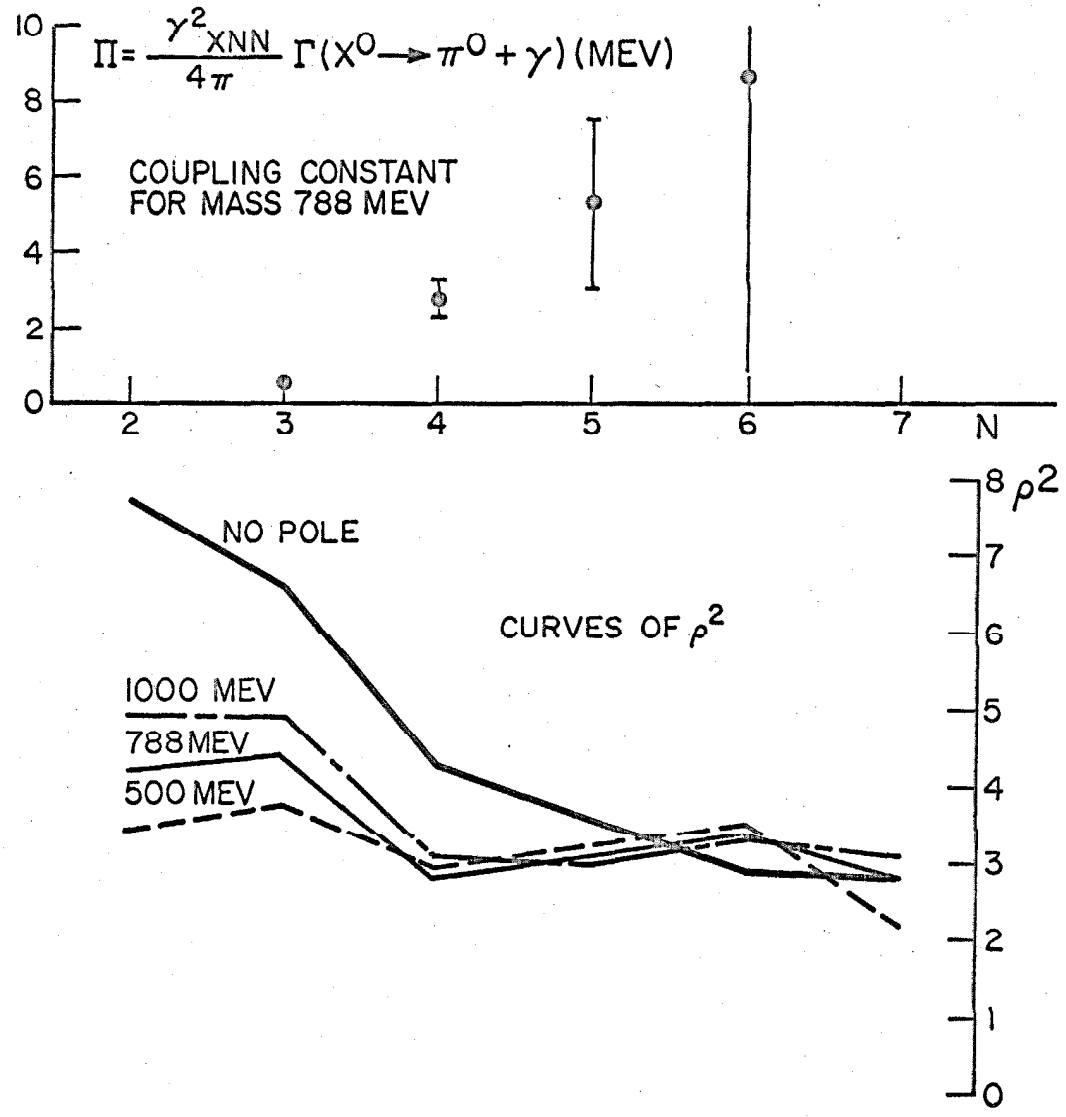

$\rho^2 = \frac{\chi^2}{NDOF}$: DETERMINED FOR MORAVSCIK FITS USING MASSES 500, 788, 1000 MEV AND NO POLE

N: MAXIMUM POWER OF $\cos\theta$ IN EXPANSION

$$(\cos\theta - \cos\theta_0)^2 \frac{d\sigma}{d\Omega} = \sum_0^N A_n \cos^n\theta$$

FIGURE 13: COUPLING CONSTANTS $\bar{k}$ = 911 MEV

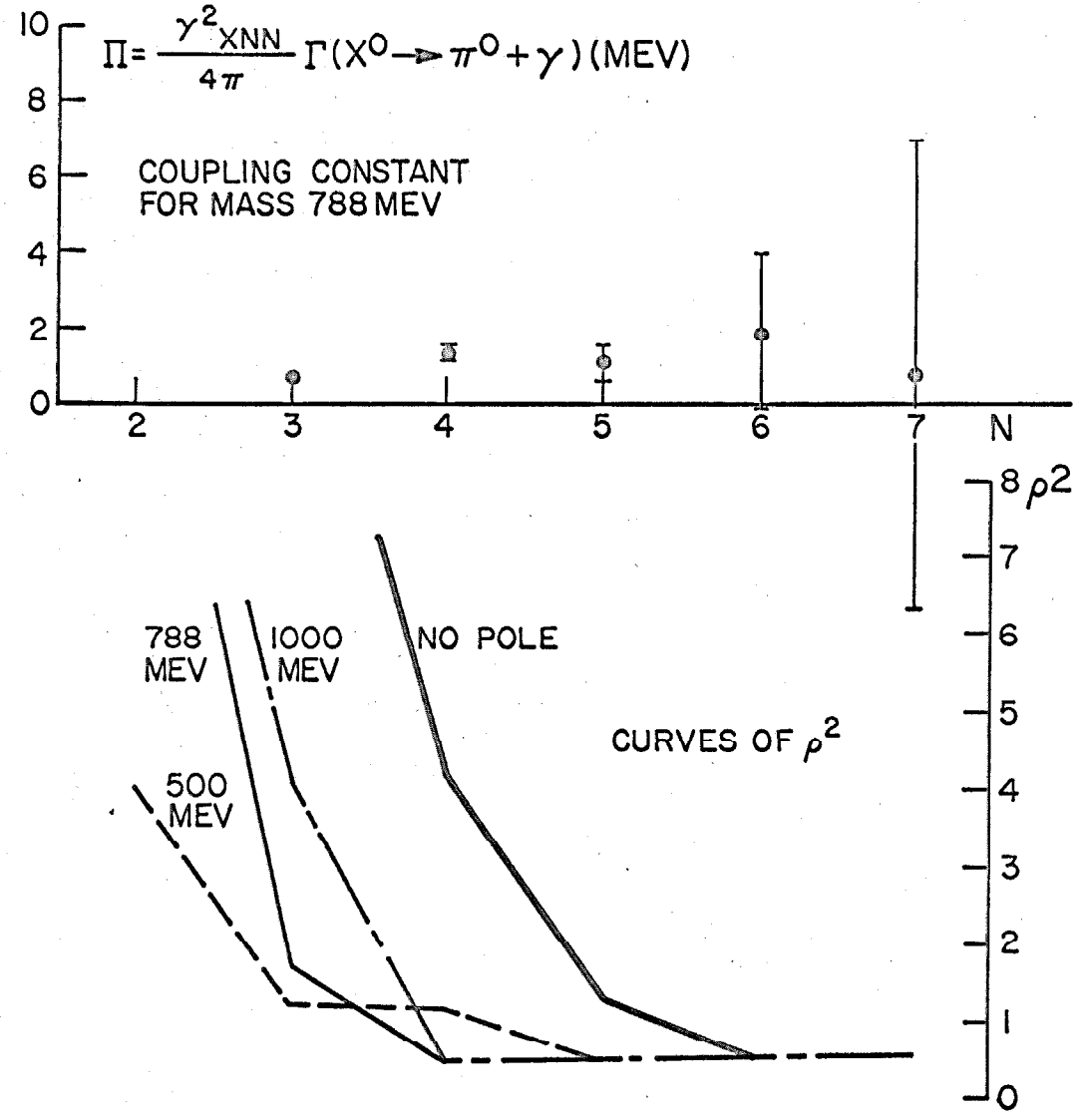

$\rho^2 = \frac{\chi^2}{NDOF}$: DETERMINED FOR MORAVSCIK FITS USING MASSES 500, 788, 1000 MEV AND NO POLE

N: MAXIMUM POWER OF $\cos\theta$ IN EXPANSION

$$(\cos\theta - \cos\theta_o)^2 \frac{d\sigma}{d\Omega} = \sum_0^N A_n \cos^n\theta$$

FIGURE 14: COUPLING CONSTANTS $\bar{k}$= 1182 MEV

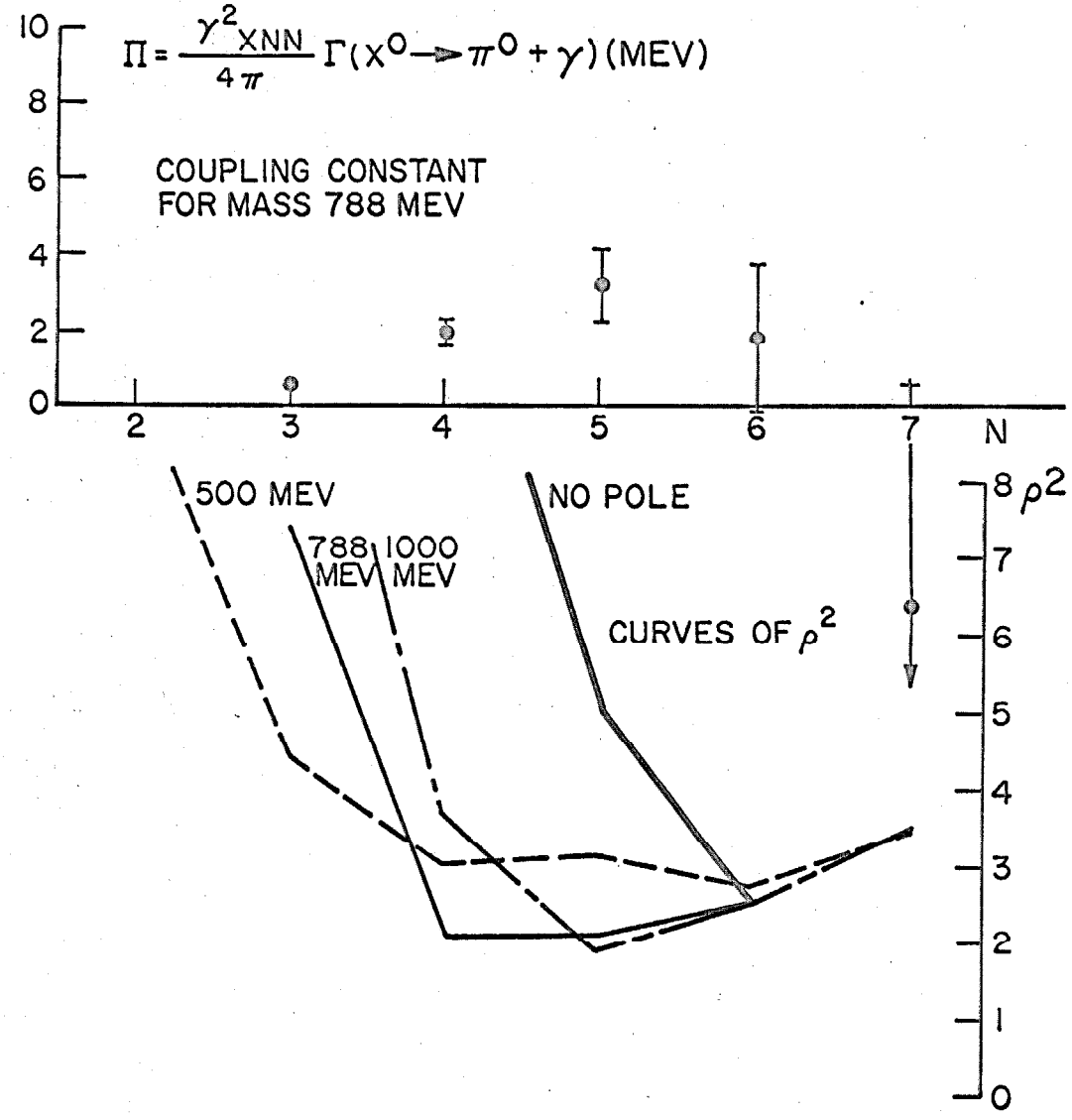

$\rho^2 = \frac{\chi^2}{NDOF}$: DETERMINED FOR MORAVSCIK FITS USING MASSES 500, 788, 1000 MEV AND NO POLE

N: MAXIMUM POWER OF $\cos\theta$ IN EXPANSION

$$(\cos\theta - \cos\theta_0)^2 \frac{d\sigma}{d\Omega} = \sum_0^N A_n \cos^n\theta$$

FIGURE 15: COUPLING CONSTANTS $\bar{k} = 1390$ MEV

and 4 powers of cos θ is roughly the same at all three energies.

$\bar{k}$	Π	N
911 MeV	2.9 ± 0.6 MeV	4
1182 MeV	1.4 ± 0.2 MeV	4
1390 MeV	2.0 ± 0.2 MeV	4

(3) A change in the mass of the exchange meson by ± 200 MeV does not have much effect on the goodness of the fit.

(4) When no pole is used and we expand $\sigma(\theta) = \sum_{o}^{N} A_n \cos^n\theta$ we find 6 powers of cos θ are needed to fit the data.

We can compare our results for Π with the best estimates available at present. Abarbanel et al.[13] used the following values of the coupling constants to calculate the nucleon magnetic moments:

$$\frac{F^2_{\omega NN}}{4\pi} \simeq 9 \pm 5 \qquad \frac{F^2_{\rho NN}}{4\pi} \simeq 2 \pm 1$$

$$\Gamma_{\omega \to \pi + \gamma} \simeq 8\, \Gamma_{\rho \to \pi + \gamma}$$

where $F^2_{xNN} = 3\,\gamma^2_{xNN}$. Since $\Gamma_{\omega \to \pi + \gamma} = (0.12 \pm 0.03) \times (9.5 \pm 2.1) = 1.1 \pm 0.4$ MeV we have

$$\Pi_\omega = (\Gamma_{\omega \to \pi + \gamma}) \frac{\gamma^2_{\omega NN}}{4\pi} \simeq 3.3 \pm 1.6 \text{ MeV}$$

and $$\Pi_\rho = (\Gamma_{\rho \to \pi + \gamma}) \frac{\gamma^2_{\rho NN}}{4\pi} \simeq 0.08 \pm 0.04 \text{ MeV}.$$

The best fit to our results at the three energies is (with $P(\chi^2) \simeq 4\%$)

$$\Pi_X = 1.8 \pm 0.2 \text{ MeV}$$

which is to be compared with the values above for Π_ω and Π_ρ.

Turning now to the fits with no pole we find at $\bar{k}$ = 1182 MeV an excellent fit is found at 6 powers of cos θ with the coefficient $A_6 = -3.0 \pm 1.3$. The power is rather high to be explained by the $f_{5/2}$ third nucleon resonance which should contribute only up to $\cos^4\theta$. Also, the fourth resonance $f_{7/2}$, still 300 MeV away when $\bar{k}$ = 1182 MeV should not be influencing the cross-section very strongly. Interference between the two resonances in this region could contribute up to 5 powers of cos θ. On the other hand, if the X^o pole term is expanded in powers of cos θ one find with $B \equiv 1/\cos\theta_o \simeq 0.5$

$$\sigma(\theta) = K\left\{1 + b\cos\theta + \sum_{N=2}^{\infty} (n+1)B^n - (n-1)B^{n-2}\cos^n\theta\right\}. \quad (3)$$

At $\bar{k}$ = 1182 MeV the coefficient of $\cos^6\theta$ is $K(7B^6 - 5B^4) = -1.2 \pm 0.2$ when K is evaluated using the Π found in the pole fits. Although the fits at $\bar{k}$ = 911 MeV and $\bar{k}$ = 1390 MeV are not as good, it is still found that 6 powers of cos θ are needed when the pole is left out. In both these cases the coefficient A_6 is also negative, however, it cannot be argued that the agreement with the coefficient of $\cos^6\theta$ in Equation (3) at these two energies is very good. The results are tabulated below:

$\bar{k}$	A_6	$K(7B^6 - 5B^4)$
911 MeV	-4.5 ± 1.7	-0.4 ± 0.1
1182 MeV	-3.0 ± 1.3	-1.2 ± 0.2
1390 MeV	-12.9 ± 3.7	-3.0 ± 0.3

In Figures 16, 17, and 18 the cross-sections are shown with the "best" fits for the three different energies. In each case the fit using the mass 788 MeV pole plus 4 powers of cos θ and the fit using just 6 powers of cos θ (no pole) is given. The shape of the curves for large angles at $\bar{k}$ = 1390 MeV is not a prediction but a reflection of the mild constraints used in the fitting where no data exist (see Page 39).

From the foregoing analysis it is not possible to draw any firm conclusions. If the vector meson pole term is present in the cross-section then we find that is more likely the ω-meson rather than the ρ-meson if a choice is to be made between the two. Our results obviously do not preclude the possibility of both the ω and ρ being present in an admixture. The one disturbing feature of the pole fits to the data is the fact that only two (N-2) powers of cos θ are needed to have a good fit. This is not physically reasonable at energies near $\bar{k}$ = 1050 MeV where the third nucleon resonance contribute up to four powers of cos θ, unless there is accidental cancellation. However, except at $\bar{k}$ = 911 MeV, where the fits are poor, it is noted that $P(\chi^2)$ does not get any worse when four (N-2) powers of cos θ are used instead of just two. Also the factor Π is substantially the same for $4 \leq N \leq 6$, i.e., two to four powers of cos θ.

The broad energy resolution and the energy calibration problem inherent in the photon detectors used in this experiment make it difficult, without very high counting statistics, to improve on the results obtained above. The broad photon energy acceptance interval necessary

to obtain adequate counting rates places serious restrictions on the usefulness of the cross-sections in testing theoretical models. A suggestion that has been made to decrease the photon energy resolution is the following: Measure angular distributions varying the mean photon energy, $\bar{k}$, in 50 to 100 MeV intervals retaining the 200 MeV photon energy interval at each step in $\bar{k}$. Then the photon energy dependence of the cross-section could be unfolded in 50 to 100 MeV bins. This system, of course, has the problem that uncertainties in energy calibration of the photon detectors could seriously affect the photon energy resolution.

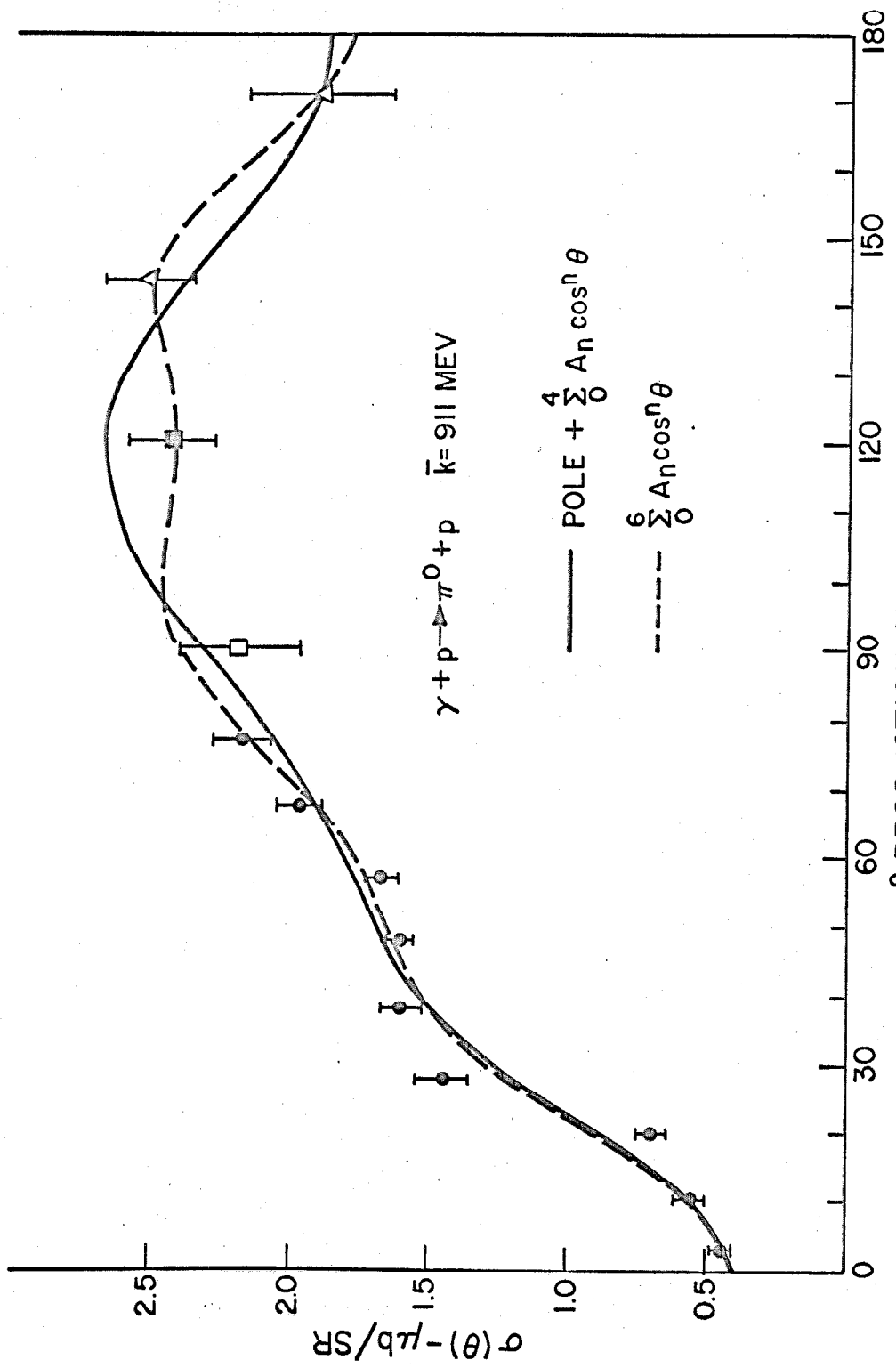

FIGURE 16: MORAVCSIK FITS TO π^0 PHOTOPRODUCTION CROSS-SECTION NEAR $\bar{k}$=911MEV

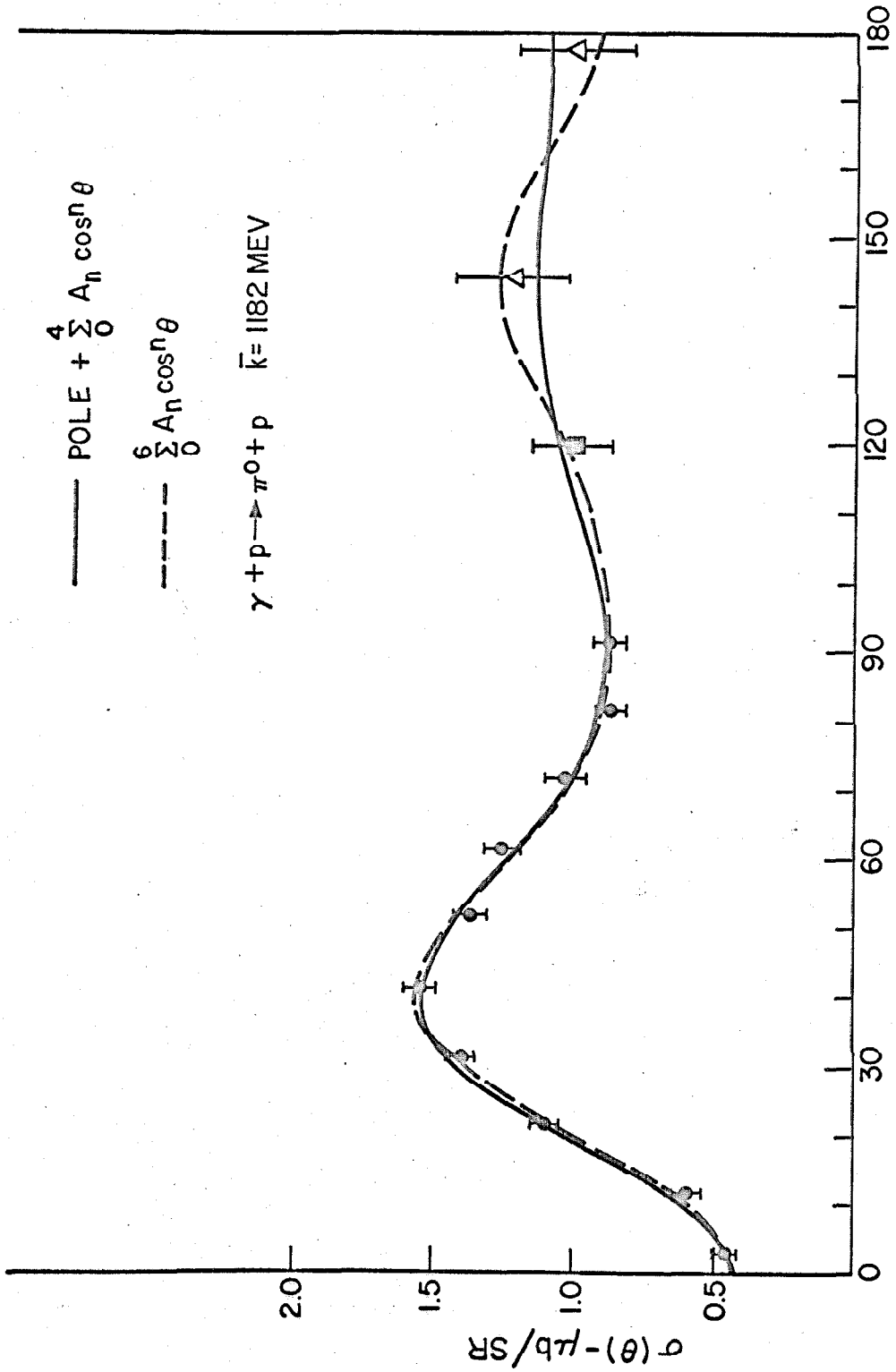

FIGURE 17: MORAVCSIK FITS TO π^0 PHOTOPRODUCTION CROSS-SECTION NEAR $\bar{k}$ =1182MEV

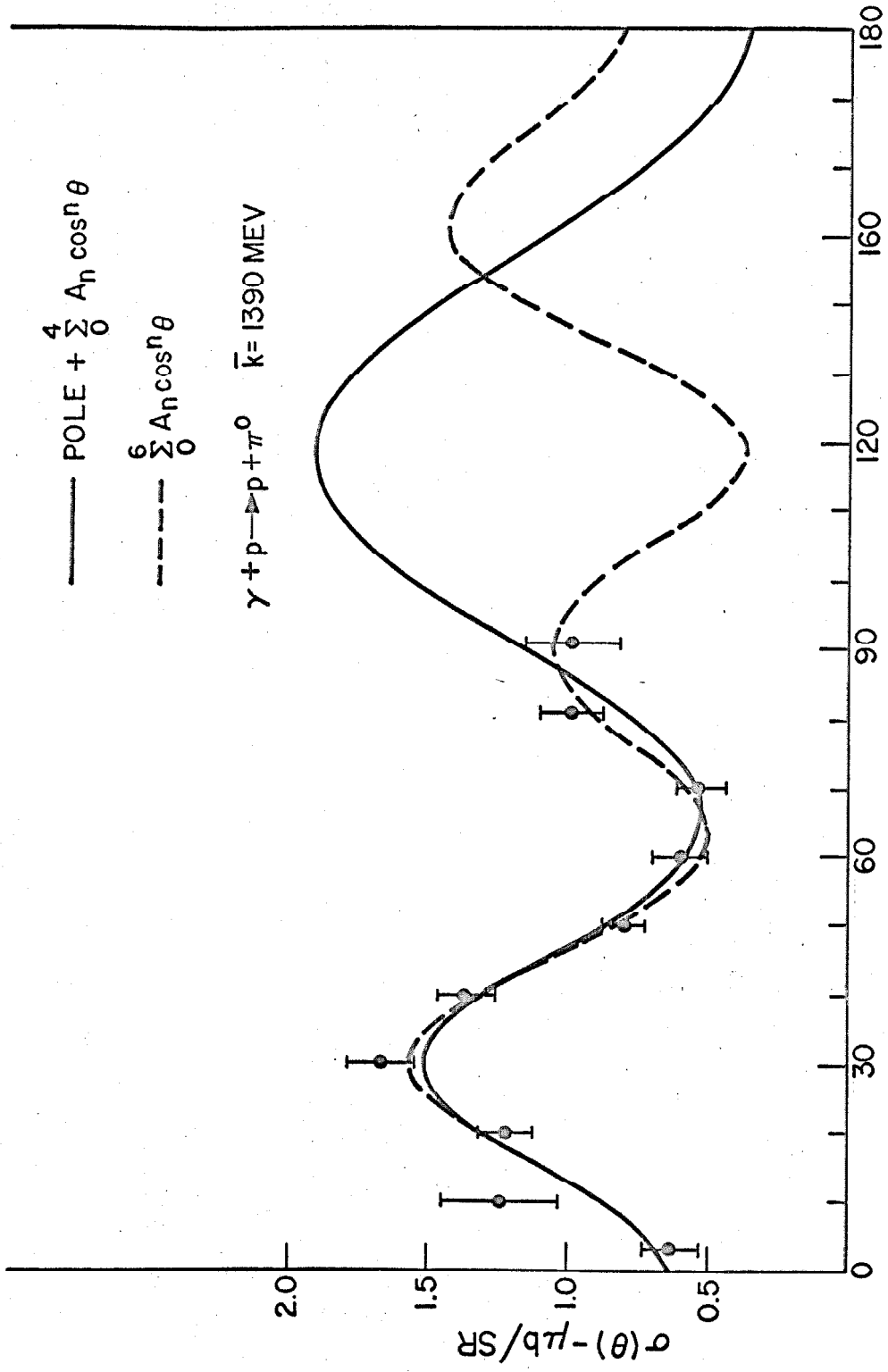

FIGURE 18: MORAVCSIK FITS TO π^0 PHOTOPRODUCTION CROSS-SECTION NEAR $\bar{k}$=1390 MEV

Appendix A

BEAM AREA EQUIPMENT

a. Synchrotron Beam

This experiment was run during a period of much change in the operating characteristics of the Caltech Synchrotron. The beam intensity had been increased tenfold making possible higher data collection rates. The radio frequency accelerating apparatus had been completely rebuilt with capacity to reach 1500 MeV, the design limit of the machine magnet. This new high energy enabled us to make measurements of the π^o production cross-sections at energies never before reached.

But all these improvements were not without some drawbacks due mainly to straining a system to new heights. The main problems were premature beam dump and premature R. F. cutoff, the former leading to beam with an end point energy less than the plateau energy and the latter causing high counting rates during a small fraction of the beam dump. The pre-dump never exceeded one percent of the total beam dumped and was typically much less. The premature cutoff of the accelerating voltage occurred as often in foreground runs as it did in background runs so the effect was minimized.

The salient features of the photon beam were the following:

Pulse rate	1 per sec.
Energy at dump	1073, 1308, 1513 MeV

Electrons accelerated 10^{10} per sec.

Dump length ~ 90 ms

The photon beam passed from the machine through a 9/16" lead collimator 13" long placed in the shielding wall of the synchrotron. As shown in Figure A1 the beam then passed through two scrapers and into the experimental hydrogen target. The beam size at the target was 1-5/8" diameter. After passing through the target the beam was stopped in a Wilson type quantameter for the purpose of beam monitoring. At this point the beam had grown to three inches in diameter -- but well within the four-inch sensitive region of the quantameter. A scintillator was placed in front of the quantameter to monitor the shape of the beam dump.

At small angles ($< 20^{o}$ in C.M.) a helium-filled bag was stretched from the hydrogen target to the $\check{C}$ counters along the beam line to eliminate production in the air.

b. Counters

Figure A1 which is on Page 6 shows the arrangement of the detection equipment. Two lead glass total absorption Čerenkov counters were placed one above the other on a moveable trolley. The trolley could be swung along tracks to selected production angles and the counters could be moved in the vertical direction to selected positions. The $\check{C}$ counters were shielded by lead - four inches on their sides and eight inches in the front. The aperture on their front side facing the hydrogen target was made in the eight-inch wall.

Two scintillator counters with paraffin sandwiched between them were placed in front of each Čerenkov counter behind the lead apertures to detect charged particles. Two scintillators to veto vertical moving cosmic rays were placed side by side between the two Čerenkov counters. Finally, one scintillator was placed above the top Čerenkov counter and one scintillator was placed below the lower Čerenkov counter to detect cosmic rays for Čerenkov counter calibration.

In conjunction with the cosmic ray veto and cosmic ray calibration schemes two layers of lead bricks were placed between the Č counters to serve as shields for the two Čerenkov counters from the machine photon beam and to eliminate low energy cosmic rays from the counter calibrations.

c. Hydrogen Target

The hydrogen target is shown in cross-section in Figure A2. Since it had to be used for both hydrogen and deuterium it had an appendix for condensing gas and a jacket for cooling the appendix. This assembly was suspended inside an aluminum vacuum chamber which was fitted with mylar windows at each end. The appendix had end caps made of 0.0015" mylar. The target was filled by first filling the jacket with liquid hydrogen and then admitting hydrogen gas to the appendix. The appendix hydrogen gas pressure was maintained at about 1 psig to suppress bubble formation in the photon beam path. The condensed liquid hydrogen was maintained as long as the jacket remained full of liquid hydrogen. The appendix was 2" in diameter

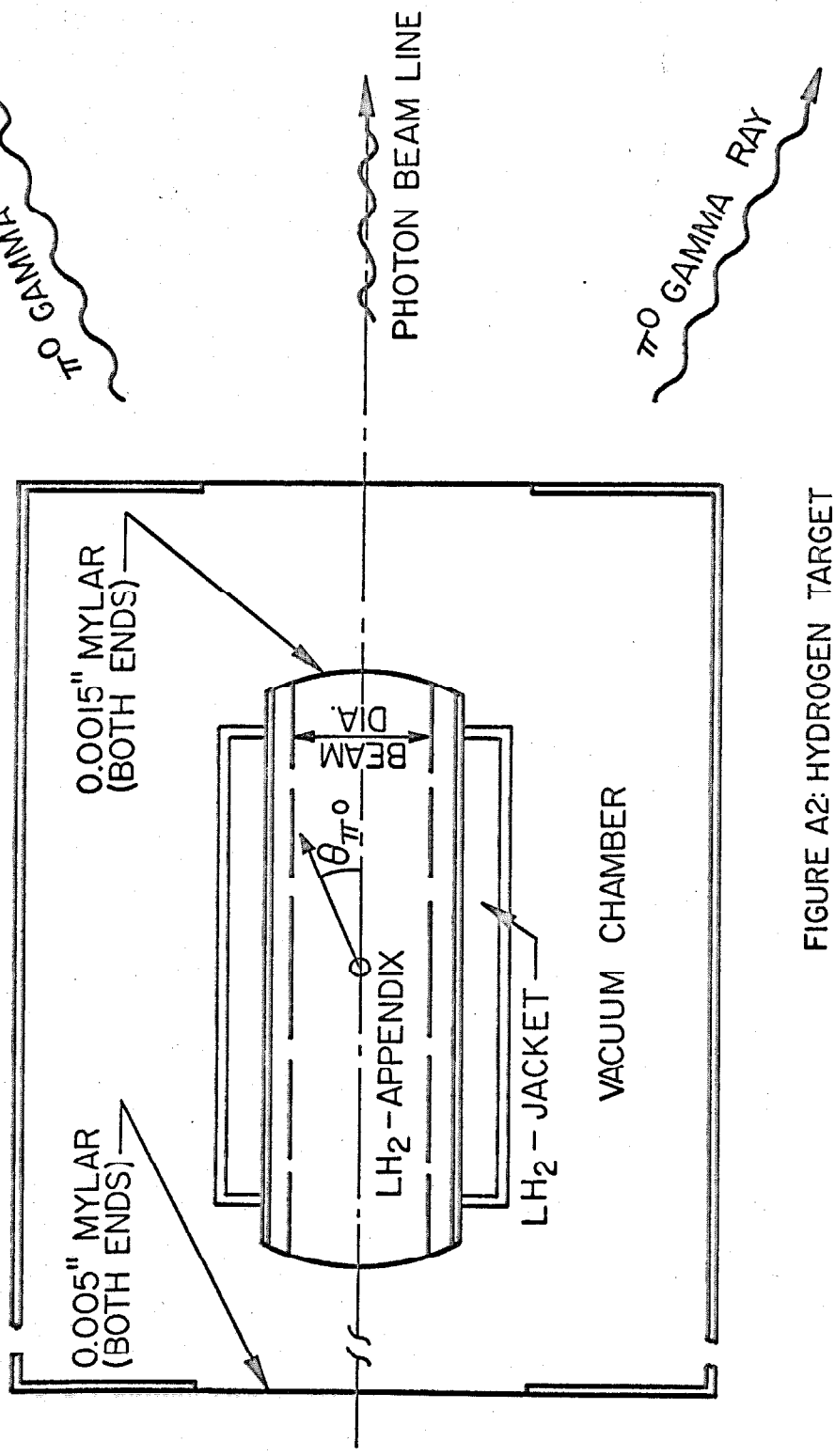

FIGURE A2: HYDROGEN TARGET

and 6.5" long at its center and with liquid hydrogen at 16 psi had a cross-sectional density of 1.17 g/cm^2.

The target was positioned inside a magnet used to sweep charged pairs produced in the hydrogen target clear of the $\check{C}$ counters. This was used for angles $\leq 20^\circ$ in the lab.

d. Quantameter

Beam monitoring was done using a Wilson type quantameter as a beam catcher (or stopper). This eliminated the need of using an auxiliary monitor which would require constant attention. The quantameter used was not the quantameter normally used in the Synchrotron Laboratory for beam monitoring. We shall call the quantameter used in this experiment QII to distinguish it from the other, QI.

The total energy of the beam is measured by QII to be $W = U_{QII} \cdot q$ where U_{QII} (MeV/coul) is determined completely by the physical characteristics of the quantameter and the density of gas inside it. q is the amount of charge collected from the quantameter when a beam with total energy W is stopped in it. To measure U_{QII} we compared QI and QII for the same total energy W. It was found that U_{QII} was 2.4% less than U_{QI} for all but the runs made at $\bar{k}$ = 1390 MeV. During the 1390 MeV runs (August 1964 - October 1964) Q_{II} began to change at the rate of about 4% per six months such that $U_{QII} = 1.02 \cdot U_{QI}$ by the end of this experiment.

Figure A3 shows the calibration of the charge integrator (full scale = 1 BIP) used for measuring the charge from the quanta-

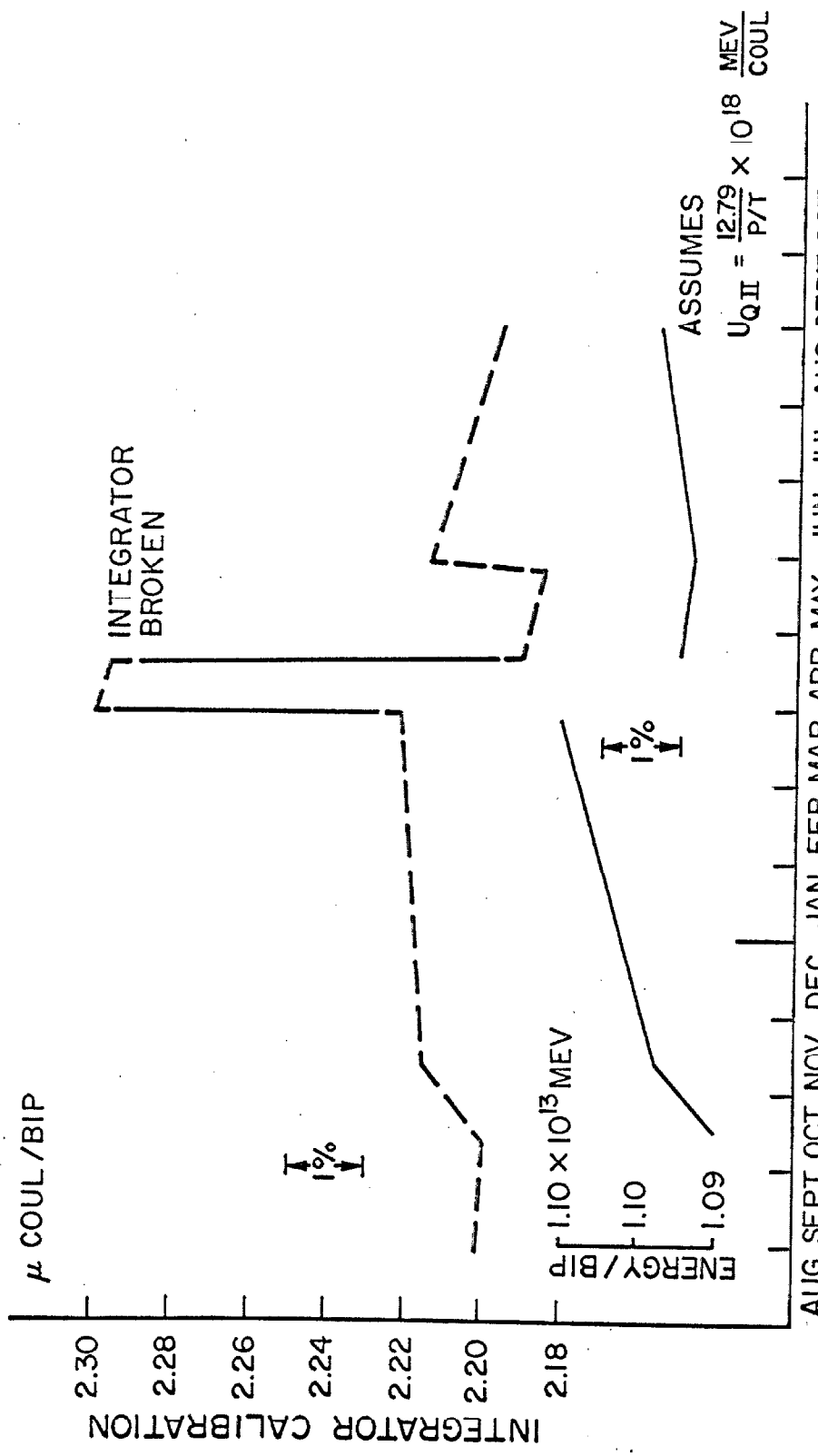

FIGURE A3: QUANTAMETER AND INTEGRATOR CALIBRATIONS

meter. The energy per BIP is computed assuming the sensitivity of the quantameter U_{QII} is constant. The integrator calibration is constant to ± 1% except for the short period in March - April 1964 when bad tubes caused a 4% change.

Further investigation by Rochester et al.[8] in the period after October 1964 has shown that the sensitivity of QII was in fact changing smoothly at the above quoted rate and that it was due to a pin hole leak in the quantameter wall. Subsequently, the quantameter was repaired, cleaned and refilled. A comparison in June 1966 of the quantameters showed QI and QII were equal to within 2%.

Appendix B

Č COUNTER CHARACTERISTICS

The two lead glass total absorption counters used in this experiment have been reported in detail by Ruderman, et al.[3] However, their salient features will be briefly stated here.

a. Physical Characteristics

Figure B1 shows the basic construction details of the counters. The two glass blocks used in each counter are 14" x 14" x 16" pieces of lead glass of density 3.88 g/cm^3 with a radiation length of 2.5 cm. The photon or electron initiated showers in the pb-glass produce high energy electrons whose Čerenkov radiation is recorded by nine RCA 7046 5" phototubes sealed against the back face of the pb-glass blocks. The nine outputs are added together to form a pulse whose charge content is proportional to the energy of the shower initiating particle.

The pulse height resulting from a muon, pion, or nucleon detected by a Čerenkov counter is small since these particles do not readily create a shower of secondary particles radiating Čerenkov light as is the case with the photons and electrons. The pulse height equivalent of a high energy cosmic ray passing through a counter is equivalent to that of a totally absorbed 220 MeV electron.

b. Selection of Tubes and Voltages

Tubes to be used in the counters were tested with an argon lamp light pulser to determine their gain versus multiplier voltage

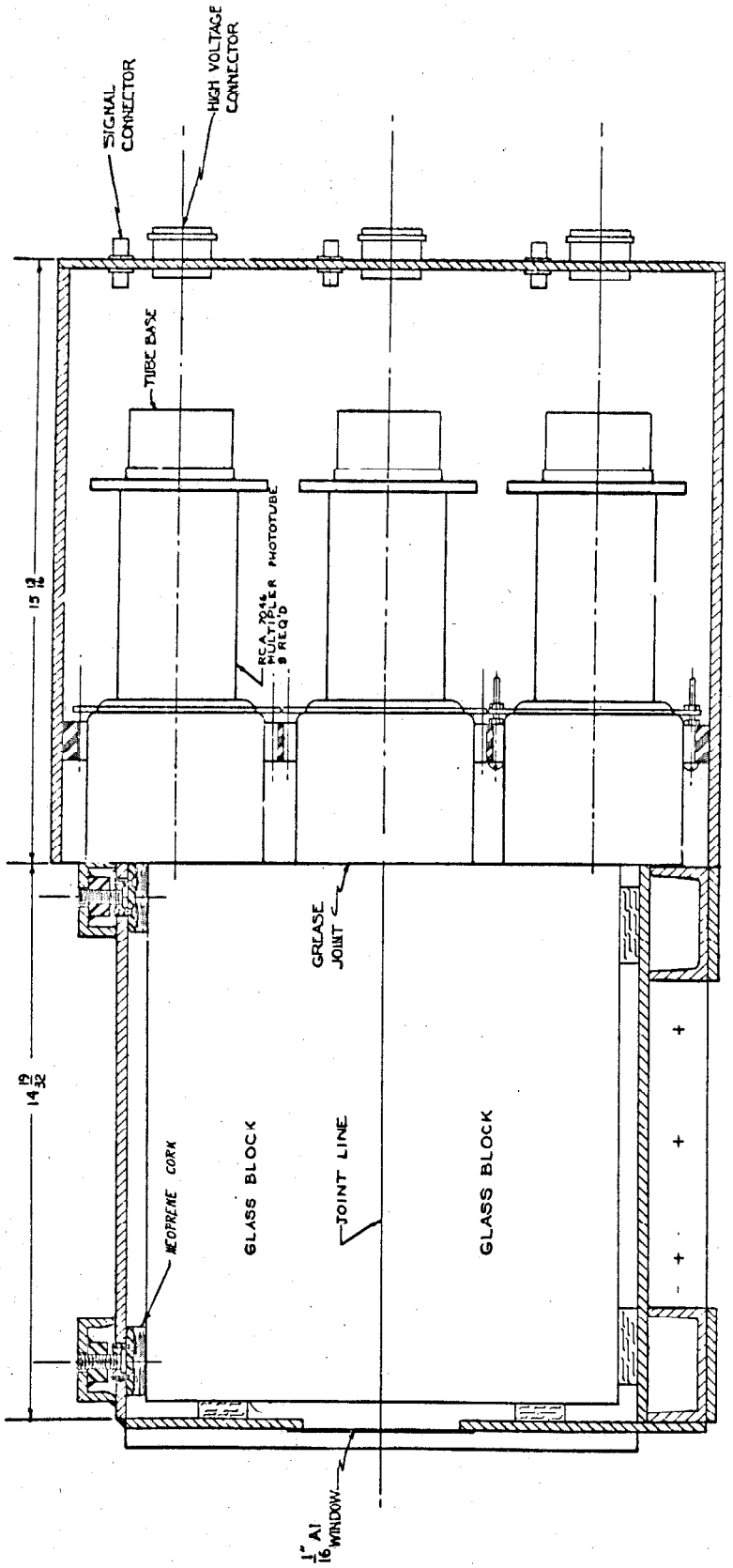

FIGURE BI: CERENKOV COUNTER ASSEMBLY SHOWING DETAILS OF CONSTRUCTION AND PHOTOTUBE MOUNTING.

characteristics and their relative cathode efficiencies, i.e., the number of photoelectrons per tube for a fixed amount of light. The width of a pulse height distribution from one of these tubes when using a pulsed light source is determined mainly by the statistics in the number of photoelectrons produced, hence the number of photoelectrons = (mean pulse height/half width of distribution)^2. Tubes with very low cathode efficiencies were replaced when feasible.

The tubes with the highest cathode efficiencies were chosen for the central positions in each counter. The tube voltages were set so that all the tubes had the same output per photoelectron. In Čerenkov counters where the greatest source of statistical fluctuations in the output of the various phototubes is in the photoelectric effect at each cathode, one minimizes the width of the summed output pulse by making the electronic gains of the several tubes the same. This has the effect of making the group of phototubes look like one large phototube.

Finally to obtain the narrowest current pulse possible from the $\check{C}$ Counter the pulses from the various tubes were timed to overlap. This was done using an argon lamp light pulser placed inside the face of the counter. The pulse outputs of the tubes were then set equal in time with respect to one another to within one nanosecond using a sampling oscilloscope and adjusting cable lengths.

The final pulse shape was measured by placing the $\check{C}$ counter in an electron beam and photographing the output of the counter with

a sampling scope. The pulse had a rise time of 5 nsec. and a full width at half maximum of 17 nsec.

c. Resolution and Linearity-Calibration

The integral spectrum from the $\check{C}$ counter for mono-energetic electrons at 1000 MeV is shown in Figure B2 along with a straight line fit to the middle section of the curve. The tails of the distribution are distinctly non-gaussian, an effect which was not investigated in detail since the true response of the counter is to be used for data reduction, not the fact that it might be gaussian. This figure shows the width (σ in gaussian distribution) at 1000 MeV to be about 6.5%.

Figure B3 shows the width σ as a function of $1/\sqrt{E}$ for both counters. From these curves one can see that the response is given by $\sigma(\text{MeV}) = 65\sqrt{E(\text{GeV})}$ where E(GeV) is the energy of the electron or photon initiating the shower. This relationship was tested for electron energies from 200-1000 MeV. These widths correspond to 237 photoelectrons in each counter at 1000 MeV. Likewise, the linearity of the counters was tested in the same electron energy range, this is shown in Figure B4. Finally, the amplitude of the pulse from each counter was set at 0.5V for 1000 MeV electrons.

The response of the counter to variation in the position of a 1-inch square beam across the face of the counter was measured, the results at 1000 MeV for counter A and at 700 MeV for counter B are shown in Figure B5. Only the central 6" by 8" region where the apertures were placed was scanned. A check at 700 MeV for counter

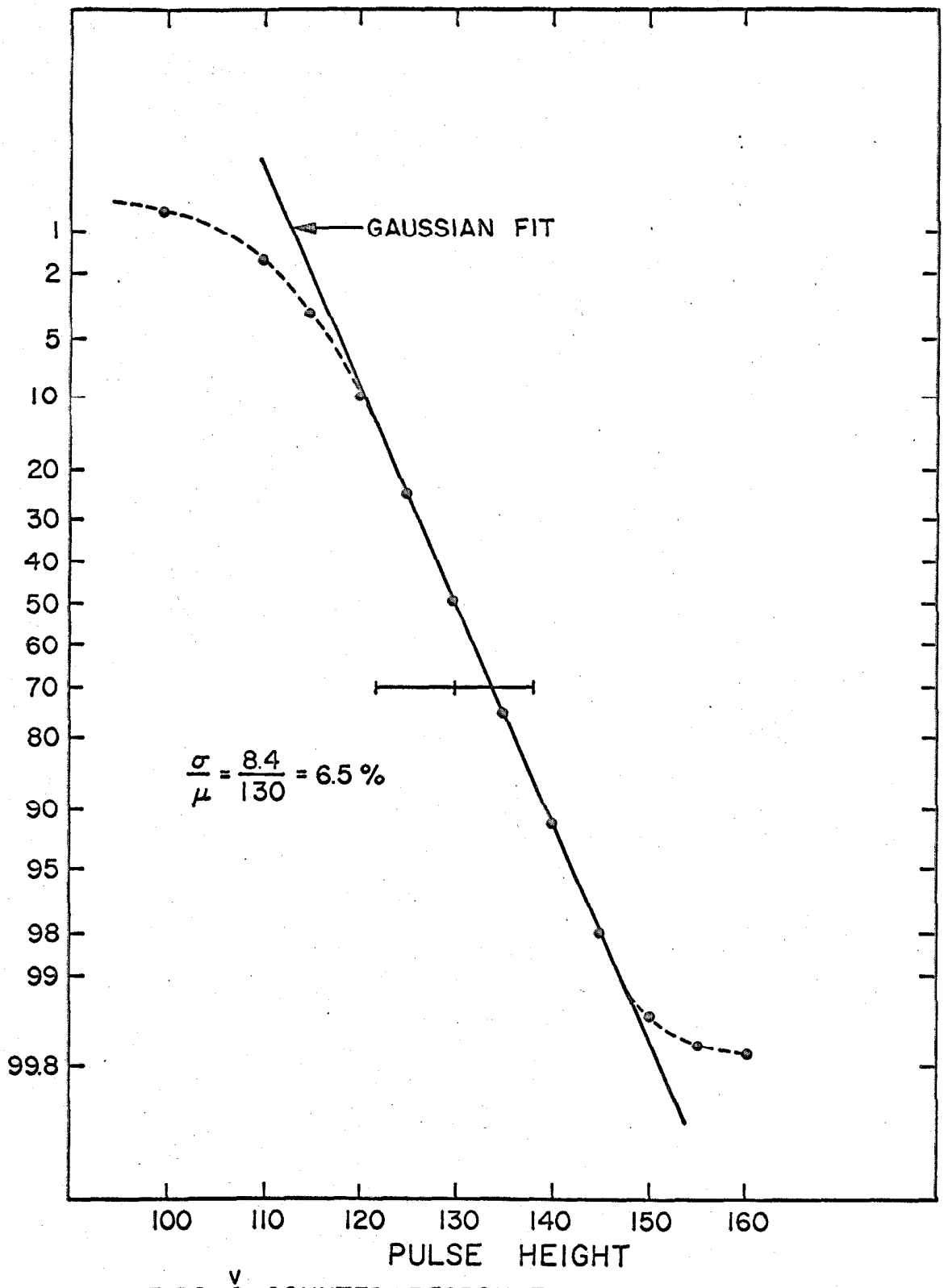

FIGURE B2: $\frac{V}{C}$ COUNTER RESPONSE TO 1000 MEV ELECTRONS

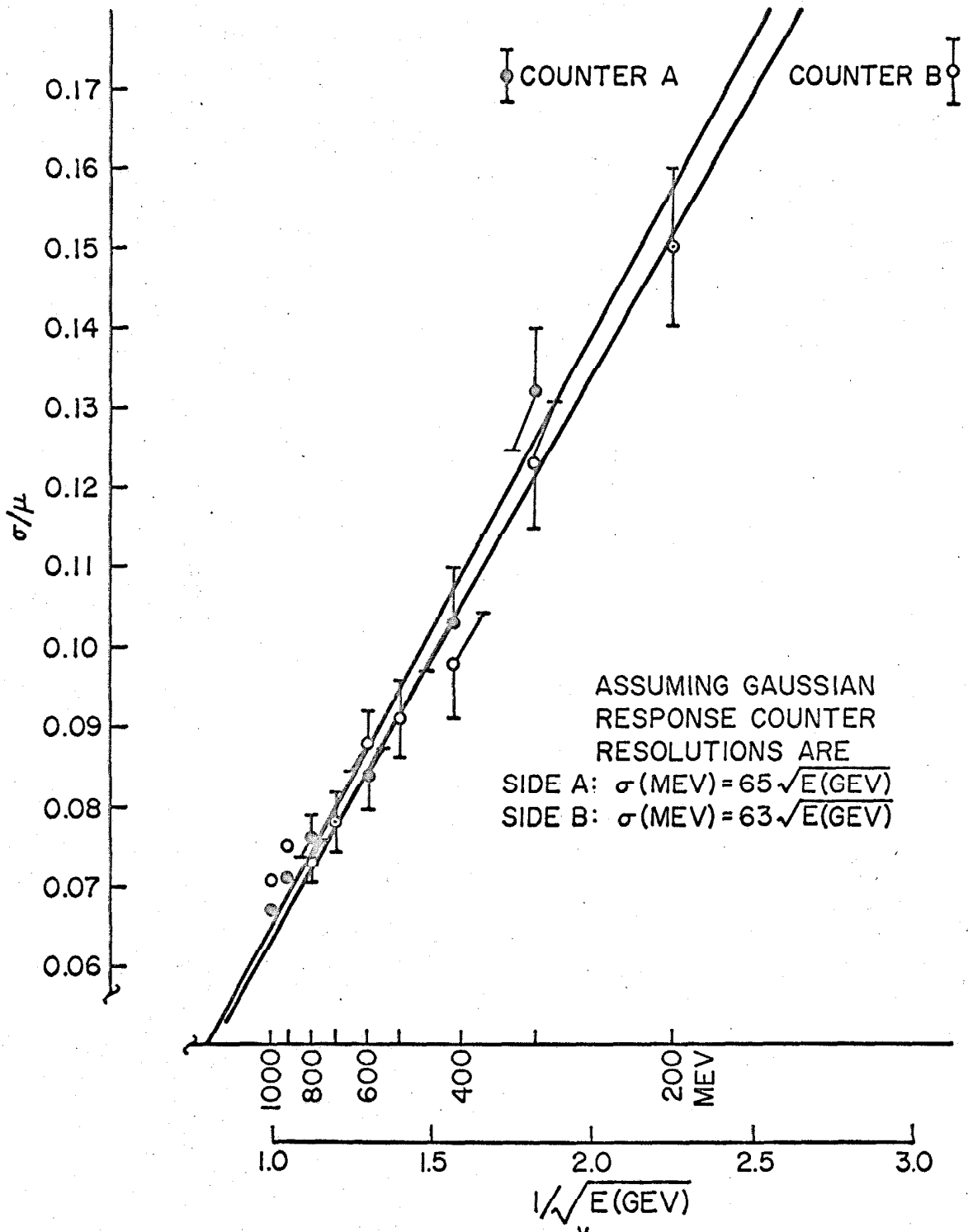

FIGURE B3: RESPONSE OF C COUNTERS TO MONOENERGETIC ELECTRONS

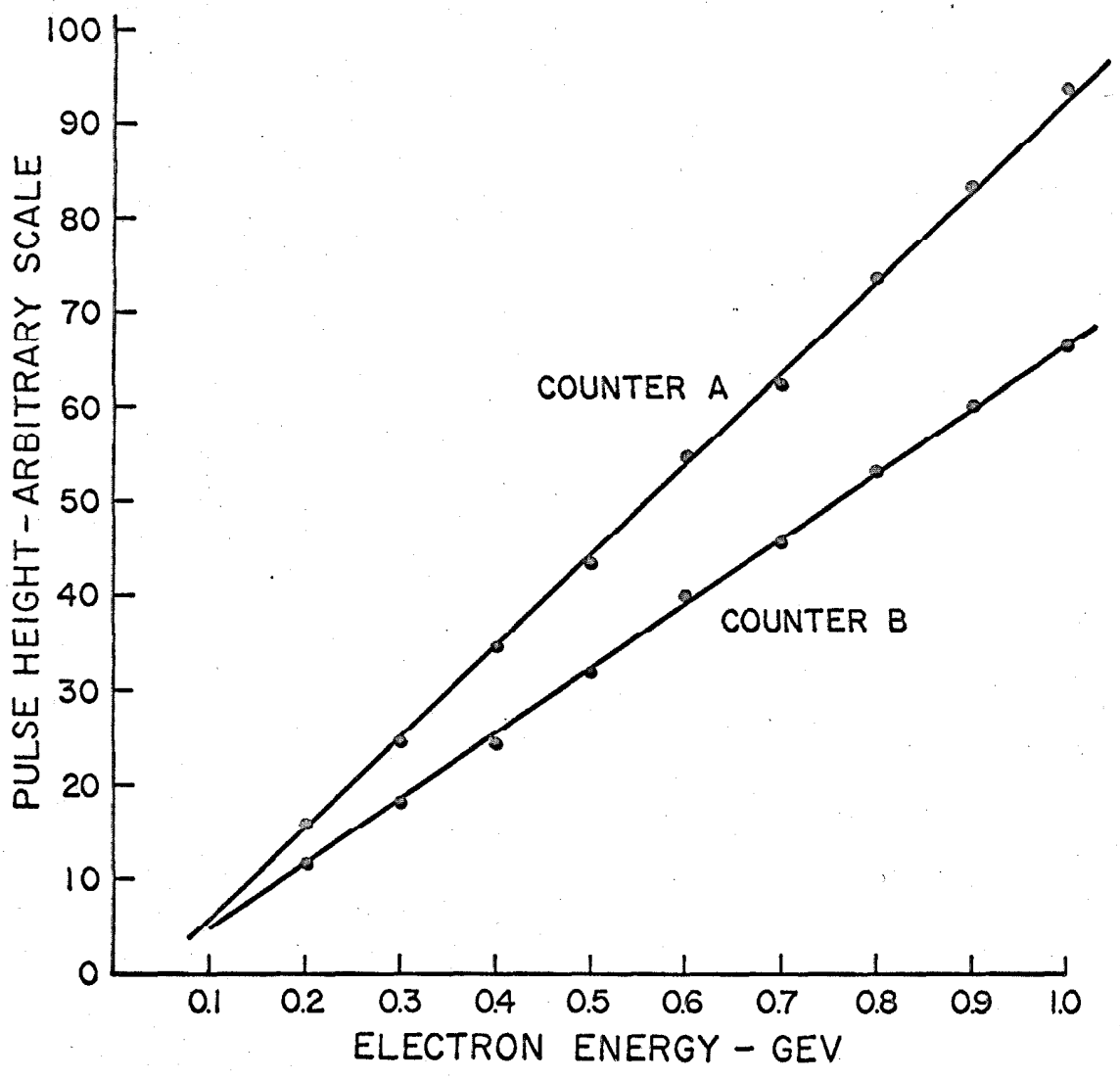

FIGURE B4: $\check{C}$ COUNTER LINEARITY

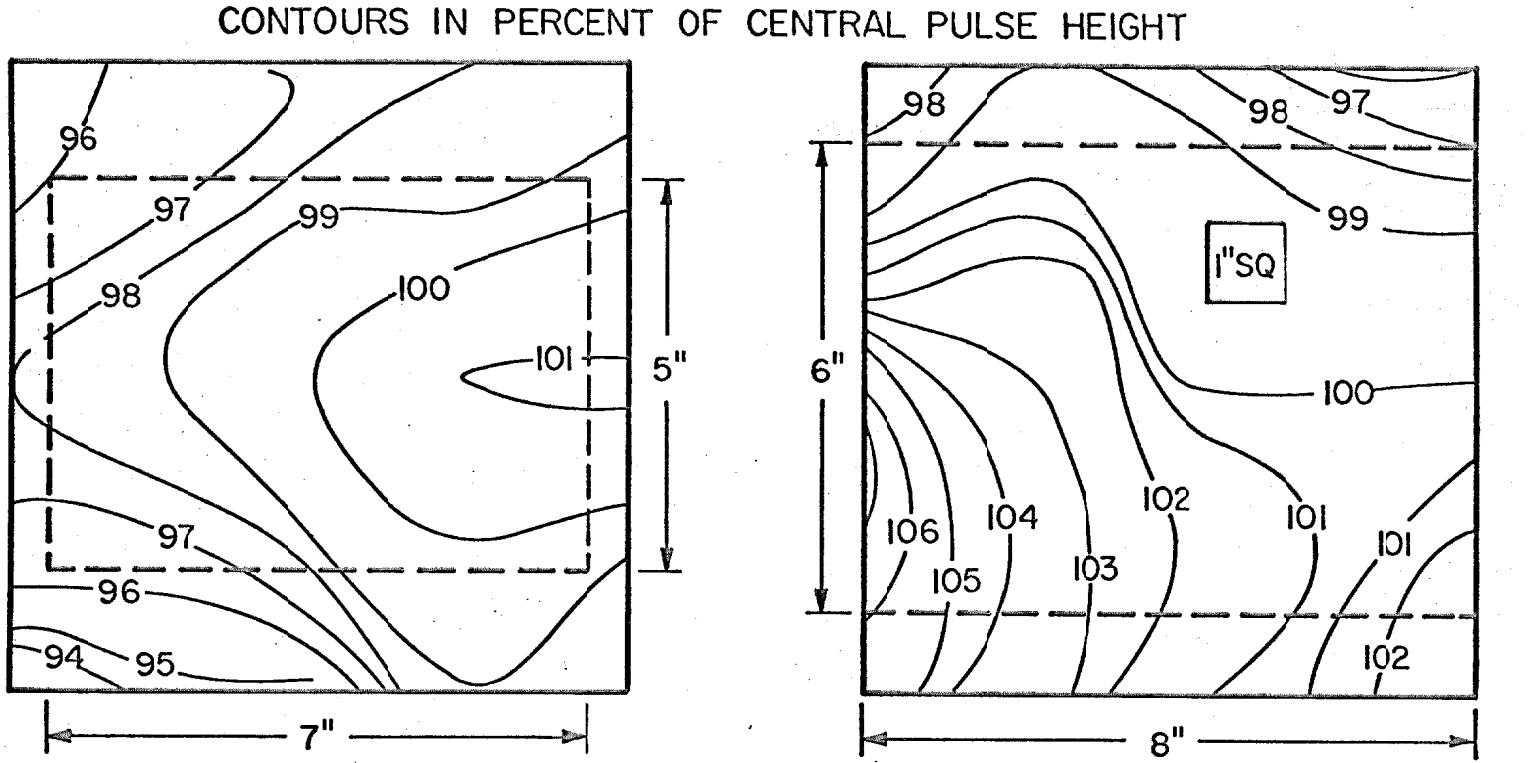

COUNTER B
SHOWING POSITION OF 5×7 APERTURE

COUNTER A
SHOWING POSITION OF 6×8 APERTURE

FIGURE B5: VARIATION IN OUTPUT OF $\check{C}$ COUNTERS FOR 1" SQUARE ELECTRON BEAM INCIDENT ON THE FACE OF THE COUNTERS

A indicated no rapid energy dependence.

d. Maintenance of Counter Calibration

In order to fit the pulse height spectra and unfold the photon energy dependence of the production cross-section, it would be necessary to know the absolute energy calibration of each counter to better than 1%. This implies that the daily change in the calibration must be known to 1%. The scheme for minimizing and monitoring the changes was the following.

High voltage input to the individual phototubes in a $\check{C}$ counter was made through a distribution box. The two distribution boxes were fed by a common power supply whose voltage was kept constant at 0.03%. Assuming the voltage dividers in the distribution boxes work properly we should expect an error in the grain of individual tubes to be no more than about 0.4% since the gain of these phototubes varies like $\sim V^{13}$.

As a check on the constancy of the voltage dividers, an electrostatic voltmeter was used to measure the voltages at the individual tubes. The meter permitted checking the voltages to 1%. Since one would expect the dividers to vary in a statistical way, the tiny variations should cancel to maintain the same pulse height. Also, if just one tube changes, then since it contributes approximately one-ninth of the pulse height, a 1% change would induce about a 1% change in total pulse height due to the V^{13} law.

The actual pulse height of the peak in the cosmic runs was measured each day. The peak of the spectrum in each counter was

A indicated no rapid energy dependence.

d. Maintenance of Counter Calibration

In order to fit the pulse height spectra and unfold the photon energy dependence of the production cross-section, it would be necessary to know the absolute energy calibration of each counter to better than 1%. This implies that the daily change in the calibration must be known to 1%. The scheme for minimizing and monitoring the changes was the following.

High voltage input to the individual phototubes in a $\check{C}$ counter was made through a distribution box. The two distribution boxes were fed by a common power supply whose voltage was kept constant at 0.03%. Assuming the voltage dividers in the distribution boxes work properly we should expect an error in the grain of individual tubes to be no more than about 0.4% since the gain of these phototubes varies like $\sim V^{13}$.

As a check on the constancy of the voltage dividers, an electrostatic voltmeter was used to measure the voltages at the individual tubes. The meter permitted checking the voltages to 1%. Since one would expect the dividers to vary in a statistical way, the tiny variations should cancel to maintain the same pulse height. Also, if just one tube changes, then since it contributes approximately one-ninth of the pulse height, a 1% change would induce about a 1% change in total pulse height due to the V^{13} law.

The actual pulse height of the peak in the cosmic runs was measured each day. The peak of the spectrum in each counter was

chosen to be at the 50% point in the integrated spectrum. The pulse height corresponding to this peak was found to vary smoothly by 10% in seven months with 3% to 5% day-to-day fluctuations.

Any larger changes in the pulse height of the peak of the cosmic rays would warn of some drastic change in one or more phototubes. To search out the problem phototubes, we were able to use an argon light pulser which had been placed inside each $\check{C}$ counter. The relative pulse heights coming from the individual tubes could be used to see gross changes in tube gains.

Appendix C

ELECTRONICS AND π^o DETECTION LOGIC

The electronics used in this experiment are the standard Synchrotron Laboratory transistorized modules. They offered great versatility in arranging logic schemes and reliability, coupled with great ease in trouble-shooting, because of simplicity of construction.

The transistor circuits operate on d.c. voltages of ± 27.0 and -6.3 volts. These voltages were monitored by a digital voltmeter and were measured to be ± 27.0 ± 0.03 (0.1%) and -6.35 ± 0.05 (1.0%) for the duration of the experiment.

a. π^o Detection

Figure 2 on Page 10 shows the main components in the logic for π^o detection. The figure below shows in more detail the logic used to obtain a γ-ray signature in one $\check{C}$ counter (e.g. counter A).

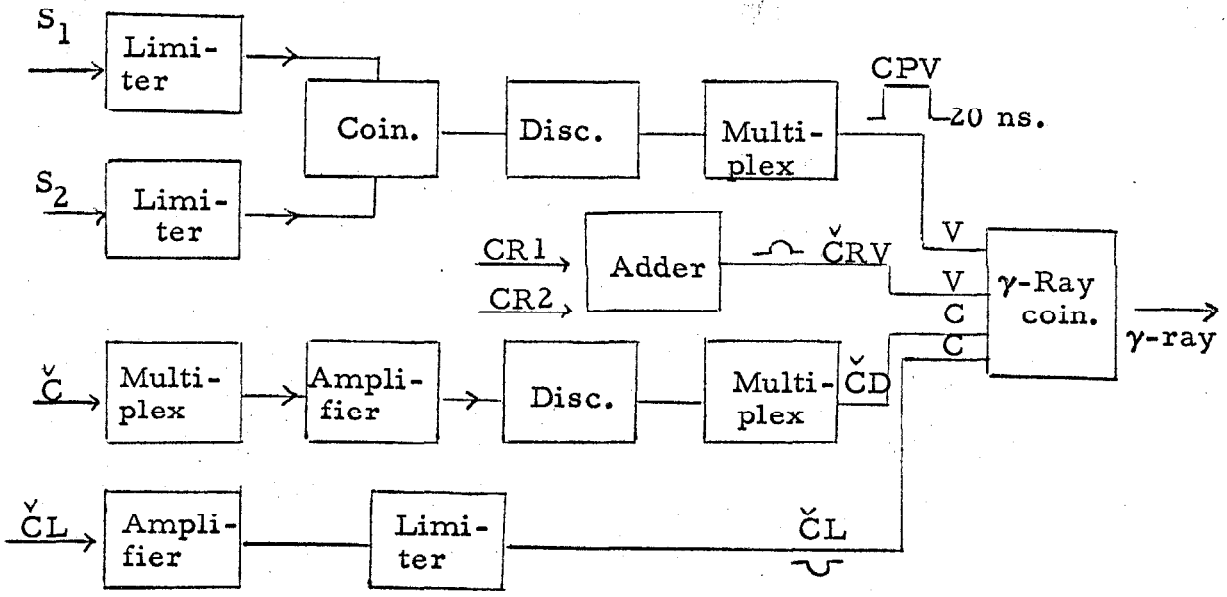

The charged particle veto scintillators S_1 and S_2 are put in coincidence and a positive signal of 20 ns. duration (CPV) is generated to veto charged particles in the $\check{C}$ counter. Two adjacent scintillators are placed between the $\check{C}$ counters, their two signals (CR1 and CR2) are added together and inverted to veto cosmic rays appearing in the two $\check{C}$ counters. The complete pulse from the $\check{C}$ counter ($\check{C}$) is multiplexed and amplified. A discriminator is set to accept only pulses ($\check{C}$) above a predetermined voltage amplitude. The energy of the shower initiating particle is proportional to the pulse height (i.e., charge) from the $\check{C}$ counter so that energy discrimination is equal to charge discrimination not pulse amplitude discrimination. However, the high counting rates of the $\check{C}$ counters prohibited pulse integration before discrimination so that the energy cutoffs seen in the pulse height spectra are not sharp but exhibit a width due to statistical fluctuations in pulse shape. The output of the discriminator ($\check{C}D$) is multiplexed and put in coincidence with the logic pulse $\check{C}L$ which is the output of just the central 3 phototubes in the $\check{C}$ counter. This pulse has been amplified and then shaped by the limiter.

A γ-ray signature can be written as $\overline{CPV} \cdot \overline{CRV} \cdot \check{C}L \cdot \check{C}D$, i.e., both aperture scintillators did not have a pulse, neither cosmic ray scintillator had a pulse, there was a pulse in the $\check{C}$ counter, and it was above a preset minimum. To establish this minimum, one determines the lowest energy γ-ray to which the apparatus is sensitive. This γ-ray is from that π^o decay in which the highest energy

π^o detectable for the lab angle and photon energy range being used decays most assymetrically, i.e., when it has an opening angle equal to the angle subtended by the outer edges of the apertures. This energy was always between 100 and 200 MeV.

This same logic was performed on counter B and the two γ-ray signatures were put in coincidence to yield π^o - like event triggers (π^oT). The figure below shows the gating of $\check{C}$ counter pulses for the ND analyzer. The gating circuits, $\underline{\check{C}\ \text{GATE}}$ were tested to see if there was any pile-up due to the high rate of low voltage pulses coming from the $\check{C}$ counters. This was done by passing a test pulse through the gating circuit while the experiment was running. The effective smearing of the pulse height of the test pulse was very small compared to the energy resolution of the $\check{C}$ counters.

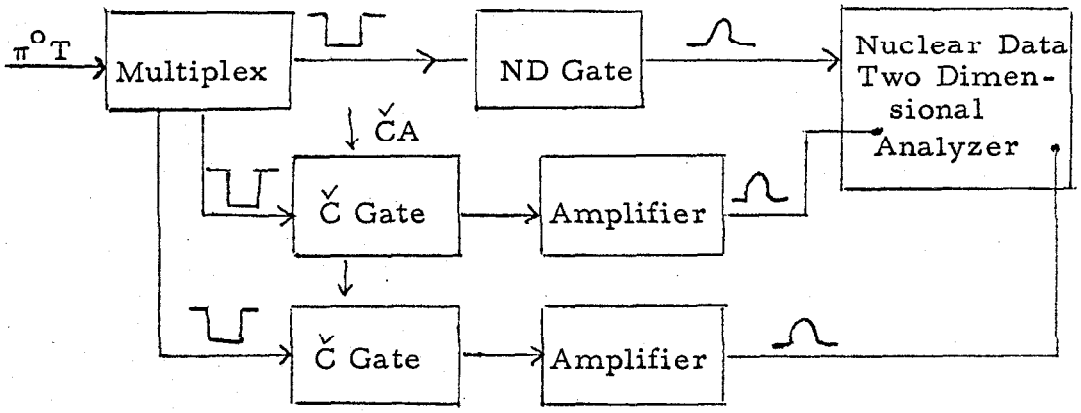

The ND gate was added to eliminate the very low energy pulse noise which would feed through the $\check{C}$ Gate circuit and cause dead time losses in the analyzer.

Deadtime losses and triggering errors due to high rates were kept below 1% by controlling the photon beam intensity. Consistency checks between the π^o triggering rate for the pulse height analyzer and the number of counts in the analyzer always showed none was lost.

Other logic used in the experiment was as follows:

1. The coincidence CPV (SIDE B) · γ-ray (SIDE A) was used to monitor how often a γ-ray in one $\check{C}$ counter was accompanied by a charged particle in the other $\check{C}$ counter causing a veto. This gives a measure of the π^o decays vetoed due to an accompanying charged particle. Measures were taken to keep this rate below 1% of the γ-ray rate.
2. The coincidence CPV · $\check{C}$D was made for each counter to monitor charged particles. A coincidence was then made between the two counters to measure charged pairs. These results were used primarily for monitoring rates to ascertain that the experiment was running normally.
3. The coincidence γ-ray (Counter A) · γ-ray (Counter B delayed by 100 ns) was used to monitor accidental coincidences. The pulse $\check{C}$B was also delayed by 100 ns. into the ND analyzer so that normal pulse height information could be obtained for background subtraction in the π^o energy spectrum.
4. The coincidence between the cosmic ray calibration scintillators was made when the experiment was not being run (synchrotron beam gated out) and was used for monitoring the

energy calibration of the $\check{C}$ counters.

b. Electronic Calibration

To make an energy calibration for the C counters and associated electronics, daily tests were made using an SKL Pulser with a shaped pulse. This test pulse was put into the mixer circuit (sums outputs of the nine tubes) at a point similar to the nine photo-tube inputs. The voltage amplitude of the test pulse was measured using a digital voltmeter. These daily electronics calibrations produced gain curves, i.e., pulse amplitude (in volts) at input versus channel location in ND analyzer, for the entire electronic system. The variation of the gain of the system as measured by the voltage for a particular channel (upper edge of channel 23 of 32 total) shows a smooth downward drift of about 10% in seven months (both sides). This drift was accompanied by a day-to-day fluctuation which varied from 3% to 5%.

A direct measurement of the stability of the ND analyzer was made by putting an appropriately shaped pulse directly into the analyzer. The changes in the voltages corresponding to the upper edges of channels 7 and 23 are given below:

	Low Channel (7)	High Channel (23)
SIDE A	3% in 7 months	1.2% in 7 months
SIDE B	3% in 7 months	1.2% in 7 months
	(fluctuations $\simeq$ 0.5%)	

These changes can be seen to be due to a drift in the pedestal of the analyzer by noting that $\frac{.03}{23/7} \simeq 1\%$, i.e., there had been a shift in

the gain curve, not a change in its slope.

Appendix D

EFFICIENCY CALCULATION

a. Calculation

If we assume a flat cross-section as a function of center of mass angles and photon energies to which we are sensitive, then the pion counting rate, when detecting pions in the energy range $E_1 < E_\pi < E_2$, is

$$CR = \left.\frac{d\sigma}{d\Omega}\right|_{CM} \int_{E_1}^{E_2} Y(E_\pi) \cdot \text{kinematic factors} \cdot dE_\pi \equiv \left.\frac{d\sigma}{d\Omega}\right|_{CM} \cdot \eta.$$

The quantity $Y(E_\pi)$ is the effective solid angle which the decaying π^o of energy E_π and production angle θ_π^{lab} sees due to the size and position of the apertures of the two gamma-ray detectors. $Y(E_\pi)$ is a function of the dynamics of the two decay gamma-rays and the geometry of the electrons.

Talman has produced an approximate analytic expression for $Y(E_\pi)$ which is very handy for quick calculations. He does use several simplifying approximations as follows:

(1.) The π^o mesons are produced isotropically for a given π^o energy,

(2) the counters lie on a spherical shell,

(3) the counters are in effect very narrow implying that the distribution of opening angles between pairs of points, one in each counter, is a triangular function,

(4) uses small angle approximations to trigger functions. The first approximation can be and is corrected for in Part b of this appendix by including the measured curvature of the cross-section. The second is trivial provided the correct radius is used. The third point has been tested by cutting the counters into ten vertical strips and computing the contributions to $Y(E_\pi)$ from the various combinations of strip counters. The difference in $Y(E_\pi)$ was less than 1%. Also, the distribution in opening angles was computed by cutting each counter into 100 blocks and pairing the blocks, one in each counter, in the various 10,000 ways. This lead to a triangular function identical to the assumed one to within 1%. $Y(E_\pi)$ computed in this way seems to be most in error at wide angles where the small angle approximation is not as good since the arguments of the trigonometric functions are reaching 10-12 degrees.

For this experiment the efficiency for detecting a π^o of energy E_π is according to Talman[10]

$$Y(E_\pi) = Y(E_\pi, \Theta_2) - 2Y\left(E_\pi, \frac{\Theta_2 - \Theta_1}{2}\right)$$

where Θ_2 is the angle subtended at the target by the outside edges of the $\check{C}$ counter apertures and Θ_1 is the angle subtended at the target by the inside edges of the $\check{C}$ counter apertures. The function

$$Y(E_\pi, \bar{\Theta}) = \frac{(\Delta\alpha)^2}{2\pi} \frac{1}{\beta^3}\left[a \cos^{-1}\frac{1}{a} - \sqrt{1 - \frac{1}{a^3}}\right]$$

where

α = the angle subtended at the target by the sides of the apertures.

$\beta = P_\pi / E_\pi$.

$a = \frac{E_\pi}{m_\pi} \sin \frac{\overline{\Theta}}{2}$.

In Figure 3(b) the shape of the $Y(E_\pi)$ folded with the bremstrahlung beam spectrum is plotted. The energy scale is the photon energy k, however, the distortion of the shape is negligible when converting from pion energy to photon energy.

To obtain the π^o energy spectrum, the energy resolution of the $\check{C}$ counters, namely, $\sigma(\text{MeV}) = 65 \sqrt{E}$ (GeV) (Appendix B), is folded in. The response used is a gaussian. Using the real resolution as measured by monoenergetic electrons made no difference and was more cumbersome to use. Adding the response measured across the face of the $\check{C}$ counters as reported in Appendix B made no difference in the spectrum shape.

Clinesmith has developed a Monte Carlo calbulation of η which is found to be in very good statistical agreement with the analytical solutions. This method selects a photon energy at random and lets the pion decay -- a success being recorded for those pions that are detected. The value of all the kinematic quantities of the decaying pion and the resulting gamma rays are tabulated. From this information the gamma-ray energy spectrum of each counter and the pion energy spectrum are produced. These spectra are then

smeared with the gaussian response of the $\check{C}$ counters and the final result is the pion energy spectrum expected in the counters.

In addition, quantities such as the laboratory and center of mass angles are kicksorted to show their distribution. Finally, the two-dimensional matrix of events (E_1^{γ} versus E_2^{γ}) is plotted for direct comparison with the calibrated results from the Nuclear Data two-dimensional pulse height analyzer.

Since this technique is statistical in nature, the statistical error in the number of successes is given by

$$(\Delta C)^2 = npq = \frac{n}{s}(n - s)$$

where

s = number of successes.

n = number of tries.

p = probability of success = $\frac{s}{n}$.

q = probability of failure = $\frac{n-s}{n}$.

Typically, $n \simeq 18,000$, $s \simeq 3,000$, so that $(\Delta C)^2 \simeq 2,500$, and the error is $\Delta C/s \simeq 1.5\%$.

It is observed that the ratio R of η (Monte Carlo) to η (Talman) does not vary significantly for a given photon energy if the counter aperture size and the target-counter distance are held fixed. An R can be calculated from η (MC) and η (T) for each case. The $P(\chi^2)$ for each is about 0.4. Ignoring the possibility of a small variation in R (with angle) it appears safe to say that the normal-

ization error in the efficiency calculation would be less than 1% when the efficiency is set equal to $\eta = R\,\eta$ (Talman). This accepts the Monte Carlo calculation as the more exact calculation in principle.

In Table D1 the details of the computation of R are given for k = 911 MeV. Here two counter configurations were used, namely, 8" x 7" apertures with 110" radius and 6" x 7" apertures with 84-90" radii. The ratio seems to be roughly flat in both cases, the second being more desirable a fit than the first. The same computation done at the other two energies resulted in similar values of the R with similar goodness of fit.

To estimate the errors in our efficiency calculation due to uncertainties in parameters, it is necessary to look into the change of the efficiency η as a function of changes in the experiment parameters. Expanding η to first order in the parameters of the figure below

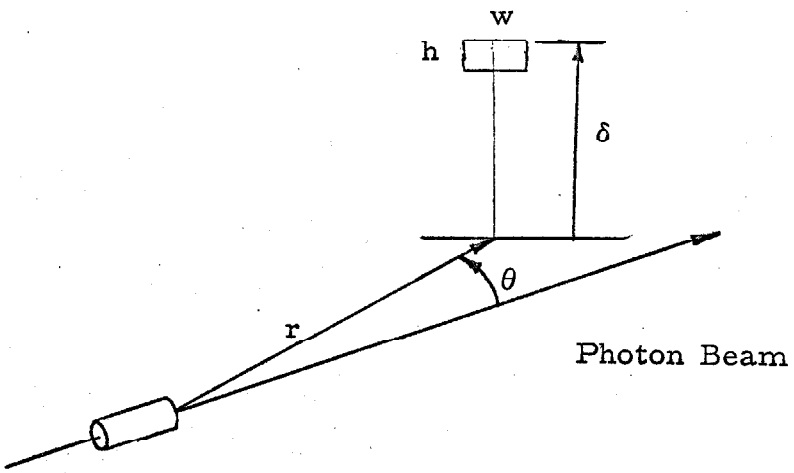

$$\eta = \eta_0 + \frac{\partial \eta}{\partial w}\Big|_0 dw + \frac{\partial \eta}{\partial h}\Big|_0 dh + \frac{\partial \eta}{\partial \delta}\Big|_0 d\delta \quad \frac{\partial \eta}{\partial r}\Big|_0 dr + \frac{\partial \eta}{\partial \theta}\Big|_0 d\theta + \frac{\partial \eta}{\partial E_0}\Big|_0 dE_0$$

Table D1

Ratio of Talman Efficiency to Monte Carlo Efficiency at $\bar{k}$ = 911 MeV for Two Different Counter Configurations

$\theta_{\pi(Lab)}$	$\eta_{(Tal)}$	$\eta_{(MC)}$	Ratio$\left(\frac{T}{MC}\right)$	
	8 x 7	Apertures		
0.	.494	.487	1.015	Statistics on Monte Carlo Calculation 2%
5.7	.487	.506	0.961	
11.3	.463	.478	0.967	
16.0	.442	.435	1.016	
21.8	.399	.414	0.964	
28.0	.342	.343	0.995	
		Average =	0.986	$X^2 = 8.6$
				$P(X^2) = 0.14$
	6 x 7	Apertures		
22.8	.639	.638	1.002	
29.1	.551	.560	0.984	
35.1	.447	.470	0.951	
42.1	.339	.347	0.975	
49.7	.239	.240	0.996	
		Average =	0.982	$X^2 = 4.0$
				$P(X^2) = 0.40$

+ . . . where E_o is the endpoint energy of the bremsstrahlung beam and η_o is the efficiency for nominal parameters.

Each of these derivatives is evaluated at the nominal parameters using the Talman program. The results are as follows:

1. $\frac{\partial \eta}{\partial w}\Big|_o$, $\frac{\partial n}{\partial h}\Big|_o$, $\frac{\partial \eta}{\partial r}\Big|_o$, and $\frac{\partial \eta}{\partial \theta}\Big|_o$ are small. Since the possible errors in these dimensions are small, the corrections are less than 1%.
2. $\frac{\partial \eta}{\partial \delta}\Big|_o$ shown as Figure E3 in Appendix E is quite large. However, the correction due to edge effects of the apertures can be made exactly. The actual setting error of this dimension during the experiment can be evaluated in the following way: δ is reset each time within 1/32 inch of its "measured value" and this occurs statistically about 5-10 times for each angle, hence the errors cancel to better than 1/100 inch. According to Figure E3 this can lead to an error of no more than 0.8%. In addition, the systematic error in the "measured value" of δ is 1/64 inch introducing an error of about 2%.
3. $\frac{\partial \eta}{\partial E_o}\Big|_o$ shown as Figure D1 is significant in the light of a problem which has existed for many years at the Caltech Synchrotron, namely E_o has not been known to better than 1% to 2% i.e., 10-20 MeV at 1000 MeV.

First, the fluctuation in setting and maintaining E_o fixed at the proper value during running time is less than 2 MeV implying

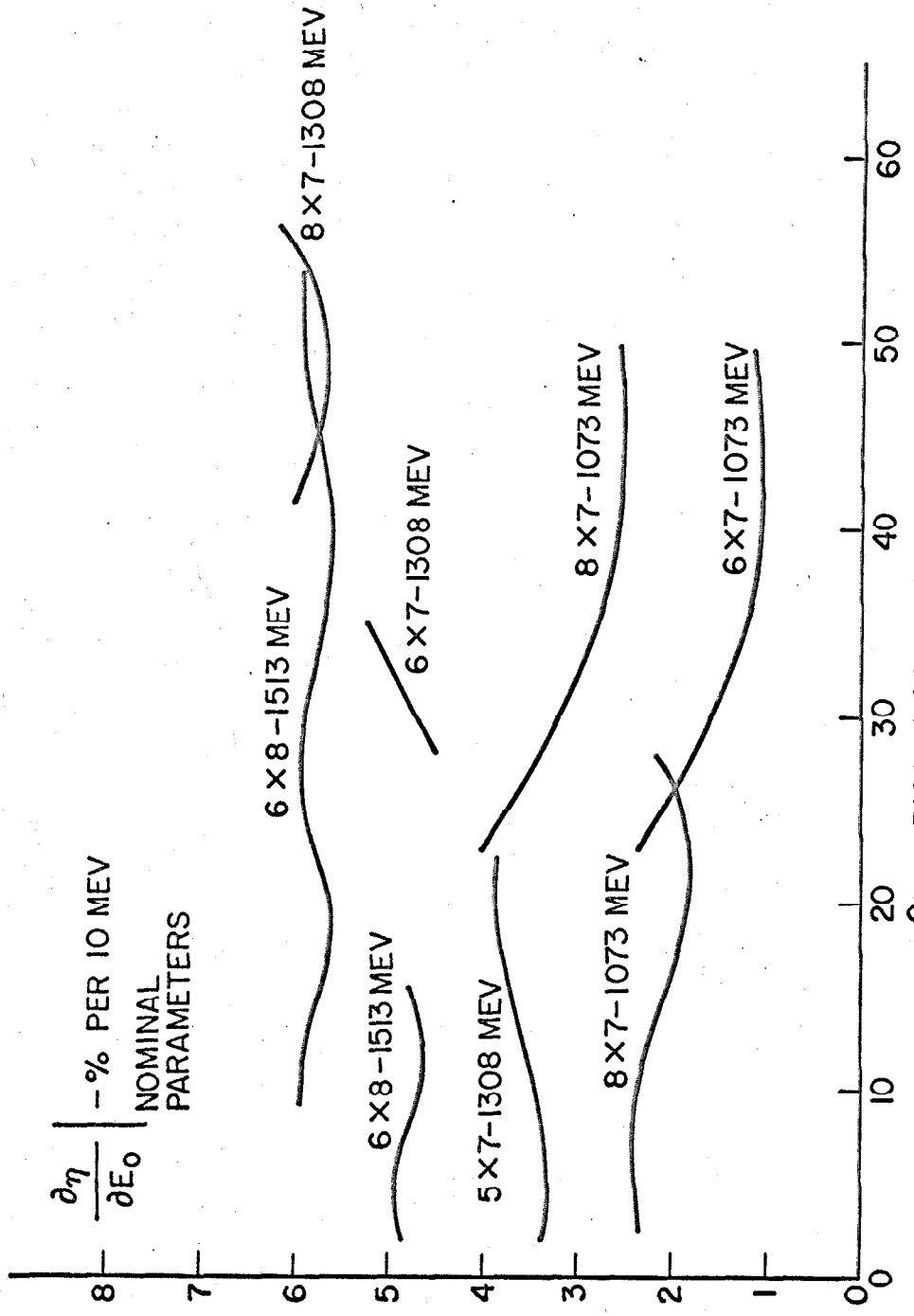

FIGURE DI: $\left|\frac{\partial \eta}{\partial E_0}\right|$ FOR THE VARIOUS APERTURES AND ENDPOINT ENERGIES

< 1% error in efficiency. On the other hand, some check must be made to instill confidence in the absolute calibration of the beam energy meter. This has been done by previous experimenters at the Synchrotron. Their results are listed below. All were done with the magnet of Walker except for Talman who used the same apparatus as this experiment.

	Set E_o	Real Energy
Diebold	1000 MeV	1021 ± 3 MeV
Peck	1280 MeV	1303 ± 6 MeV
Ecklund	1000 MeV	1020 ± 10 MeV
Talman	1280 MeV	1300 ± 10 MeV

All measurements indicated a + 1% to + 2% error in E_o. In February 1965, H. A. Thiessen[11] made detailed tests of the electronics associated with the beam energy monitor and found that for a beam radius of 146"

$$E_{o\ true}/E_{o\ meter} = 1.021 \pm 0.003 .$$

Since this agrees very well with the checks made by previous experimenters, it is reasonable to conclude that the endpoint energy of the machine is in fact, given by the Thiessen result. The beam radius for this experiment was 146.3 ± 0.2 inches, therefore, the endpoint energies were:

$E_{o\ set}$	$E_{o\ real}$	Error
1050 MeV	1073	± 4 MeV
1280 MeV	1308	± 5 MeV
1480 MeV	1513	± 5 MeV

The error includes the uncertainty in measuring the absolute energy and the uncertainty in the position of the beam target in the machine aperture.

Then it can be seen that a basic uncertainty of $\leq 4\%$ must be attached to our resulting cross-sections independent of statistical errors. This has the effect of moving all the cross-sections up or down by about 1% to 4%, depending on $\bar{k}$.

The efficiencies used are given in Table D2. Also given are the parameters of the experimental setup.

b. Correction to Cross-Section Due to Curvature in σ

The "average" cross-section for a measurement point (θ_o) has been computed assuming the real cross-section is constant. From the cross-section plots as a function of angle it can be seen that at some angles and energies the cross-section is changing quite rapidly. From these results one can iterate to find the average cross-section more exactly.

If we expand the cross-section in terms of $(\theta - \theta_o)$, where θ_o is the average acceptance angle, then

$$\sigma(\theta) = \sigma(\theta_o) + \sigma' \Big|_{\theta_o} |(\theta - \theta_o)| + \tfrac{1}{2}\sigma'' \Big|_{\theta_o} (\theta - \theta_o)^2 + \ldots$$

Table D2

EFFICIENCY - PION/μbarn - BIP

$\bar{k}$ = 811 MeV E_o = 1073 MeV k_{min} = 700 MeV

θ_{CM}	θ_{lab}	Aperture h x w	Efficiency (η)	Radius Inches	Delta(δ) Inches
3.5	0.0	8.05 x 7.00	0.624	110.0	21.35
11.2	5.7	8.05 x 7.00	0.609	110.0	21.45
20.3	11.3	8.05 x 7.00	0.569	110.0	21.65
28.0	16.0	8.06 x 7.00	0.534	110.0	22.26
38.1	21.4	8.06 x 7.00	0.474	110.0	22.86
47.5	29.1	6.06 x 6.83	0.620	84.50	18.31
57.4	35.1	6.06 x 7.00	0.525	85.75	19.56
67.3	42.1	6.07 x 6.80	0.374	87.25	20.82
77.5	49.7	6.07 x 6.58	0.247	89.38	22.42
$\bar{k}$ = 1182 MeV		$\bar{k}_o$ = 1308 MeV	k_{min} = 960 MeV		
3.7	0.0	5.04 x 7.00	0.344	109.2	15.69
11.4	5.7	5.04 x 7.00	0.338	109.2	15.84
21.4	11.3	5.04 x 7.00	0.303	109.2	15.94
31.9	17.1	5.04 x 7.00	0.262	109.2	16.24
41.8	22.8	5.04 x 7.00	0.223	109.2	16.74
51.6	28.0	6.04 x 7.00	0.230	110.0	17.64
61.6	35.0	6.05 x 7.00	0.159	110.2	18.40
72.0	42.0	8.05 x 7.00	0.145	110.2	19.87
81.6	49.0	8.05 x 7.00	0.115	110.2	21.40
91.0	56.0	8.06 x 7.00	0.080	110.4	22.91
$\bar{k}$ = 1390 MeV		E_o = 1513 MeV	k_{min} = 1145 MeV		
3.1	0.0	6.08 x 8.04	0.204	146.9	17.43
10.5	5.0	6.08 x 7.81	0.182	146.8	17.43
19.6	10.1	6.08 x 7.66	0.174	146.0	17.73
29.6	15.3	6.08 x 7.33	0.143	145.1	18.03
39.2	20.2	6.09 x 8.04	0.335	109.4	14.14
49.6	26.0	6.07 x 8.04	0.252	109.4	14.65
60.3	32.4	6.09 x 8.04	0.203	109.4	15.58
70.2	38.7	6.09 x 8.04	0.154	109.5	16.61
80.8	53.0	6.10 x 8.04	0.080	110.0	19.60
90.7	53.0	6.10 x 8.04	0.080	110.0	19.60

Hence to second order the average cross-section is

$$< \sigma(\theta) > = \sigma(\theta_o) + \tfrac{1}{2}\sigma''\big|_{\theta_o} <(\theta - \theta_o)^2> + \ldots$$

The linear term is zero since $(\theta - \theta_o)$ is evenly distributed about θ_o. $\sigma(\theta_o)$ is the cross-section determined by dividing the counting rate by the efficiency. Hence the best average, to second order in $(\theta - \theta_o)$, is obtained by adding a small term proportional to the curvature.

The quantity $<(\theta - \theta_o)^2>$ is found using the Monte Carlo efficiency calculation and is generally three to four degrees^2. In order for the correction to be significant, it must be ≤ 0.1 μb, therefore

$$\sigma'' \leq \frac{2 \times 0.1}{4} = 0.05 \ \mu b/\text{degree}^2 \qquad \text{(in CM)}.$$

The table below shows the places where the curvature is large.

Correction to Cross-section for Curvature

Energy	Angle	σ''	$(\theta - \theta_o)^2$	σ_o	$\frac{1}{2}\sigma''<(\theta-\theta_o)^2>$
911	20.0	+0.009	2.92	0.70 ± 0.08	+0.03
911	28.0	-0.009	2.83	1.46 ± 0.09	-0.03
911	57.0	+0.003	4.38	1.66 ± 0.05	+0.01
1390	10.5	-0.010	2.00	1.24 ± 0.21	-0.02
1390	19.6	+0.004	2.00	1.24 ± 0.12	+0.01
1390	29.6	-0.003	3.02	1.65 ± 0.10	-0.01

The correction is small at all places and at the most is only one-third of the quoted error due to statistical fluctuations in the experiment.

An attempt was made to correct the cross-section as measured in this experiment for the curvature in the real cross-section as a function of photon energy. If we expand the cross-section

$$\sigma(k) = \sigma_o + \sigma' \Big|_o (k - \bar{k}) + \tfrac{1}{2} \sigma'' \Big|_o (k - \bar{k})^2 + \ldots$$

and take the average using this experiment photon energy resolution f(k) then

$$\langle \sigma \rangle = \int \sigma(k)\, f(k)\, dx = \sigma_o + \tfrac{1}{2} \sigma'' \Big|_o \langle (k-\bar{k})^2 \rangle + \ldots$$

where σ_o = C.R./η. Hence the "best" average value that we can quote differs from σ_o if there is curvature in $\sigma(k)$. The cross-section was plotted as a function of photon energy at the three average energies $\bar{k}$ = 911, 1182, and 1390 MeV. A smooth curve through the three points at each CM angle was used as a trial function for $\sigma(k)$. The counting rate and the cross-section $(\sigma_o)'$ was computed for the various points measured in this experiment. The difference $(\sigma_o)' - \sigma_o$ was found to be less than the statistical error assigned to the reported value σ_o.

In the graph on page 31 the values of σ at 60^o and 120^o for Diebold at 911 MeV and Diebold with this experiment's resolution differ due to local minima in $\sigma(k)$.

Appendix E

ABSORPTION CORRECTIONS

Corrections must be made for absorption of decay gamma-rays in the target assembly, in the air between target and counters, and in the charged particle veto counters.

a. Target

Figure A2 is the plan view of the hydrogen target. The $\check{C}$ counters are placed a distance R from the center of the target at an angle θ_{π^o} with the beam line. The effective beam diameter was 1-5/8 inches at the hydrogen target 320 inches from the machine target.

To calculate the absorption correction the sensitive volume of the hydrogen target was sectioned into 26 discs each of which was sectioned as shown in Figure E1. Furthermore, from Groom's measurements of the synchrotron beam profile[12] we are able to approximate the radial fall-off of the beam intensity as shown in Figure E1. Since two-thirds of the beam falls within the circle with radius equal to one-half the beam radius, the sum of the inside four sections is weighted equal to the sum of the outside eight sections. This allowance for the beam profile leads to a correction in the absorption calculation at small angles of about one-tenth the absorption.

The absorption as a function of angle is shown in Figure E2. The flattening at wide angles is understood by noting that at gamma-ray angles greater than about 30 degrees all gamma-rays must pass

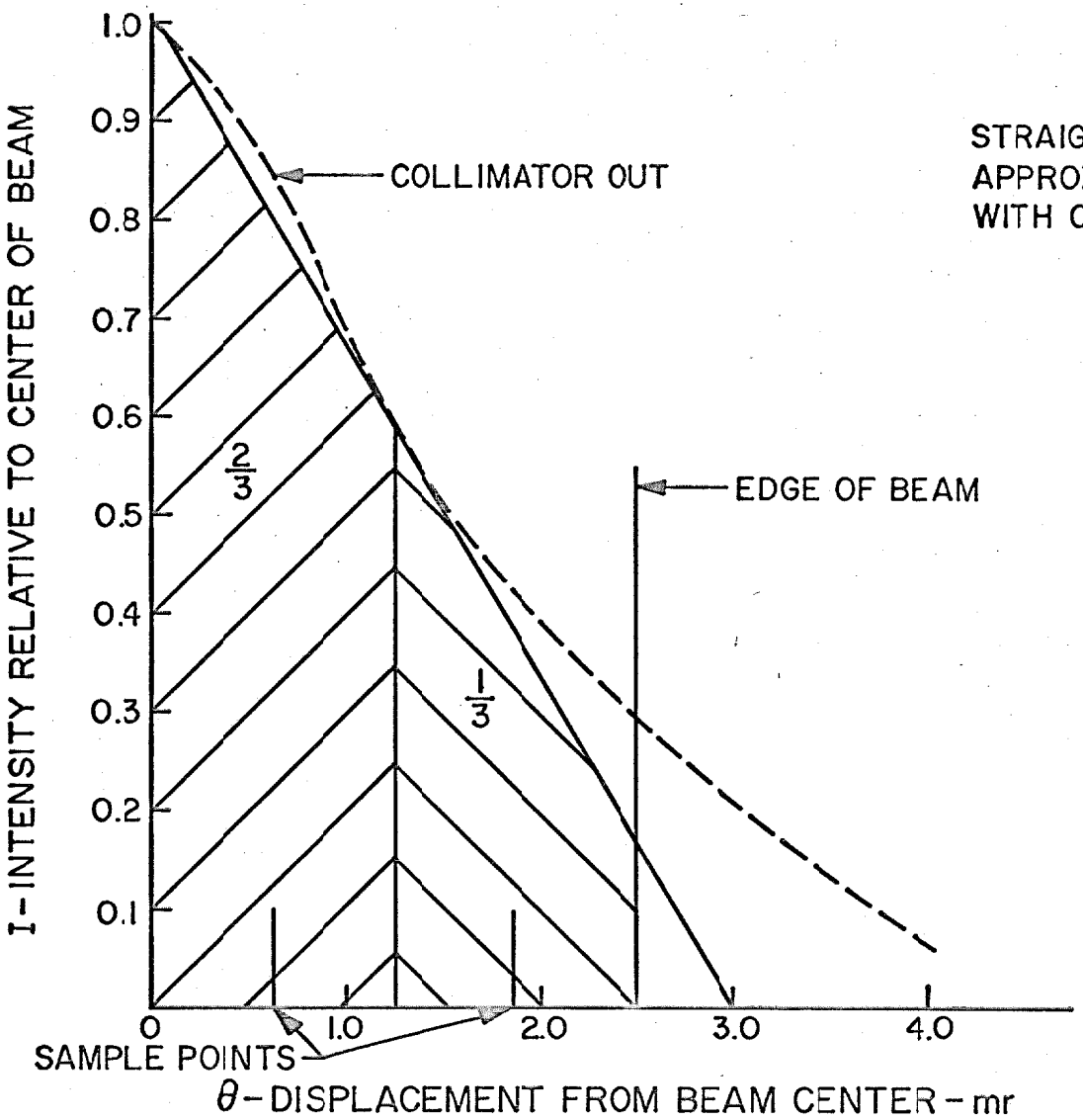

STRAIGHT LINE $I = -\theta/3 + 1.0$ IS APPROXIMATION TO BEAM PROFILE WITH COLLIMATOR IN PLACE

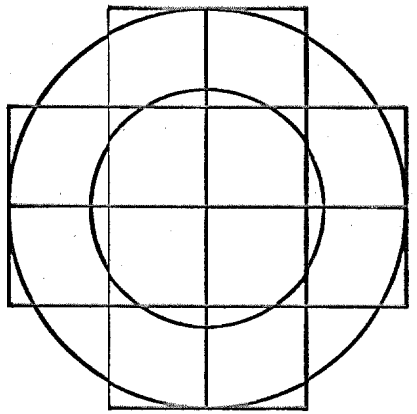

VIEW ALONG BEAM

FIGURE EI: PHOTON BEAM PROFILE

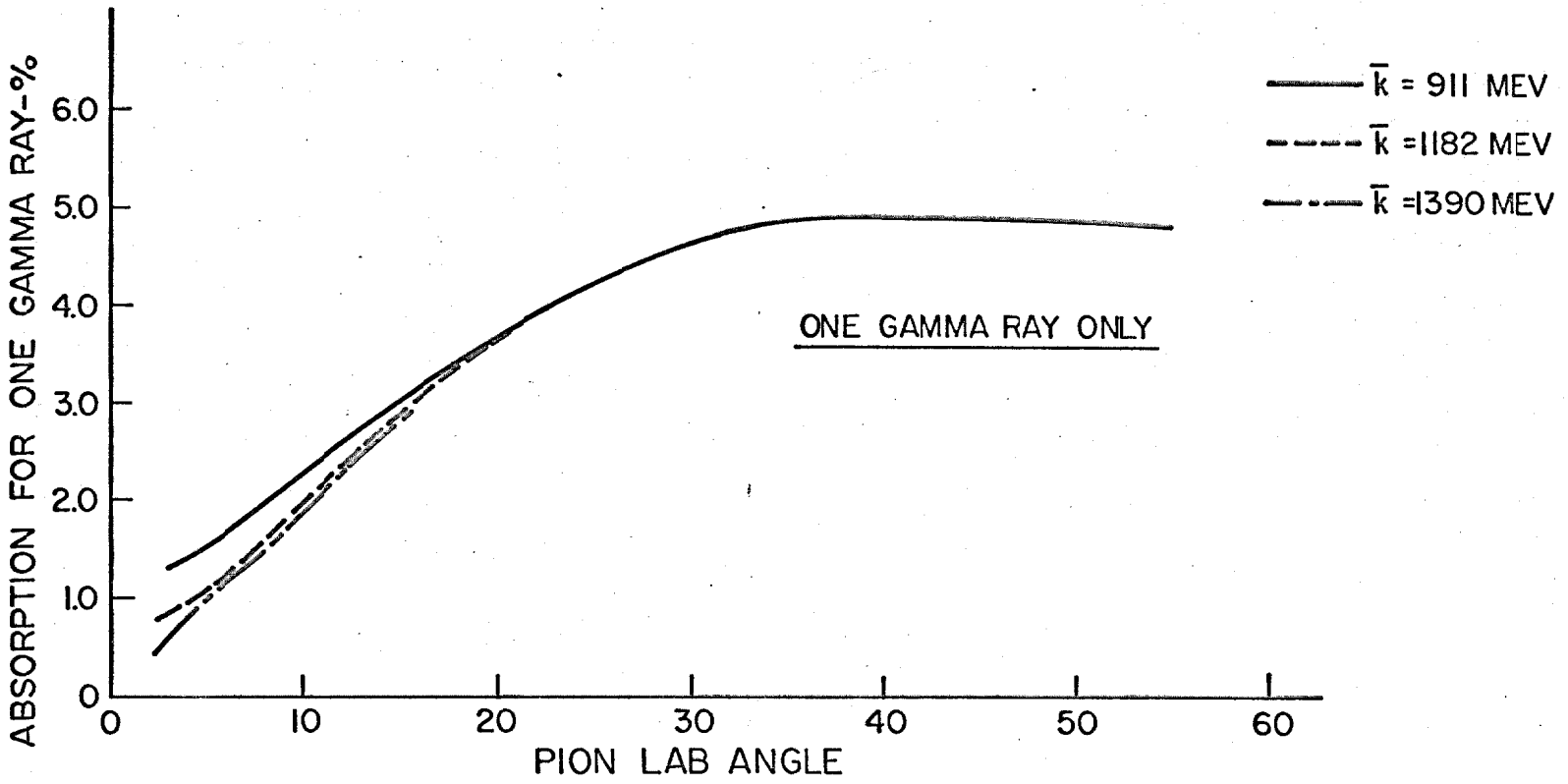

FIGURE E2: ABSORPTION OF GAMMA RAYS IN HYDROGEN TARGET

through all walls of the target with approximately the same angle.

b. Air and Veto Counter Absorption

The air path length from target to $\check{C}$ counters varied from 80-110 inches implying a 1% to 2% correction for absorption of decay gamma-rays.

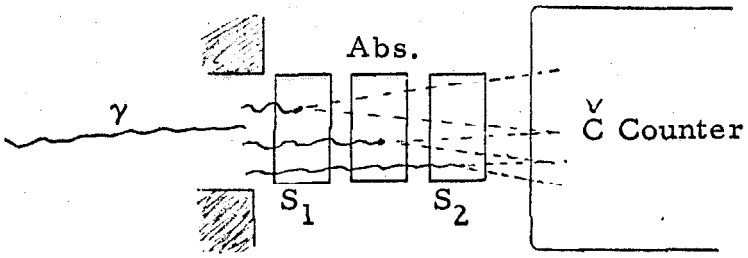

The absorption in the veto counter assembly can be seen by referring to the figure above where the two scintillators are shown with the paraffin absorber between. If a γ-ray converts to electrons in S_2, the paraffin, or surrounding air, the $\check{C}$ counter will still record the energy of the γ-ray (with a negligible degradation in energy) because there are not coincident pulses in S_1 and S_2. However, if the conversion takes place in S_1 then vetoing can take place if the electron makes a large enough pulse in S_1. The thickness t of S_1 is 1.27 cm and the $1/\sigma$ length for the γ-ray in scintillator material is 59 cm, so the intensity of γ-rays as a function of depth into the counter is essentially linear. There is also a function P(x) which is the probability that the conversion electrons will produce a large enough pulse to make a coincidence with S_2. This function obviously is nearly one for the front of the counter and nearly zero for the back - varying smoothly in between. The structure of P(x) is due to the fact that a minimum ionizing particle gives a spectrum of pulse heights, some being below the coincidence discrimination.

The discrimination level on the S_1 amd S_2 pulses was set to be one-half the average signal from a minimum ionizing particle traversing the counter. The electron pair produced are both minimum ionizing; therefore, conversion in the first three-fourths of the counter should produce a coincidence, i.e., the function P(s) is nearly unity out to $x = 3/4t$ where it decreases towards zero. Folding P(x) into the linear decay of the γ-ray intensity leads to an absorption correction of $\frac{3\sigma t}{4} = 1.7\%$ per γ-ray.

c. Partial Absorption at Edges of Apertures

The apertures were shaped on three sides so that gamma-rays entering the apertures would always make grazing angles with the sides of the apertures. However the remaining side was horizontal and would have gamma-rays incident upon it at relatively large angles, in the order of ten degrees. Gamma-rays can with a small probability make their way through the edges of the apertures and be recorded. They can also convert to electrons in the lead and be absorbed or vetoed. This effect leads to an increase both in effective aperture size and a decrease in the energy cutoff. If while sitting at an angle θ_π(lab) the distance between the outer edges of the two apertures is increased then the minimum E_π is decreased and the efficiency is increased.

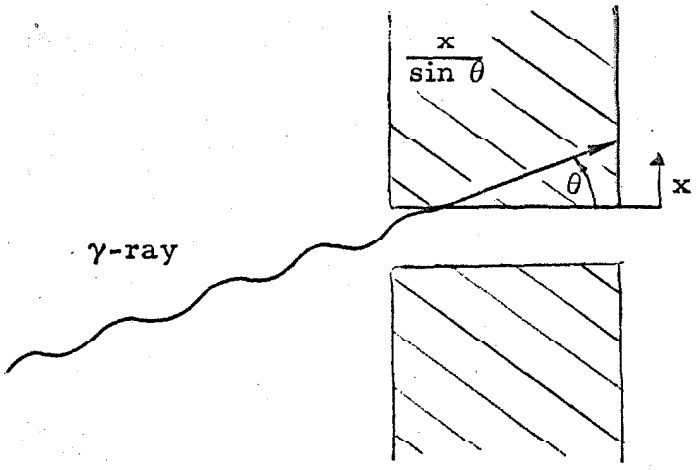

Referring to the figure above, x is the distance from the outer edge of the aperture. One can move this edge of the aperture up and down parallel to the x axis and calculate an efficiency $\eta(x)$ where $\eta(0)$ is the efficiency for the nominal position of the aperture. We expend the efficiency about x = 0 to be $\eta(0) + \frac{\partial \eta}{\partial x}\Big|_0 x$. The gamma-rays have a path length in the lead of $x/\sin\theta$. Then the corrected efficiency would be

$$\eta' = \eta(0) + \frac{\int_0^\infty \frac{\partial \eta}{\partial x}_0 \; x\, e^{-\frac{\sigma \sin\theta}{x}} \, dx}{\int_0^\infty e^{-\frac{\sigma \sin\theta}{x}} \, dx} = \eta(0) + \frac{\partial \eta}{\partial x}_0 \frac{\sin\theta}{\sigma}$$

From Figure E3 we can see that $\partial\eta/\partial\delta$ can be as great as 8%/0.1 inch or 30%/cm. Then the error due to the effective change in the location of the outer edge of the aperture can be as large as

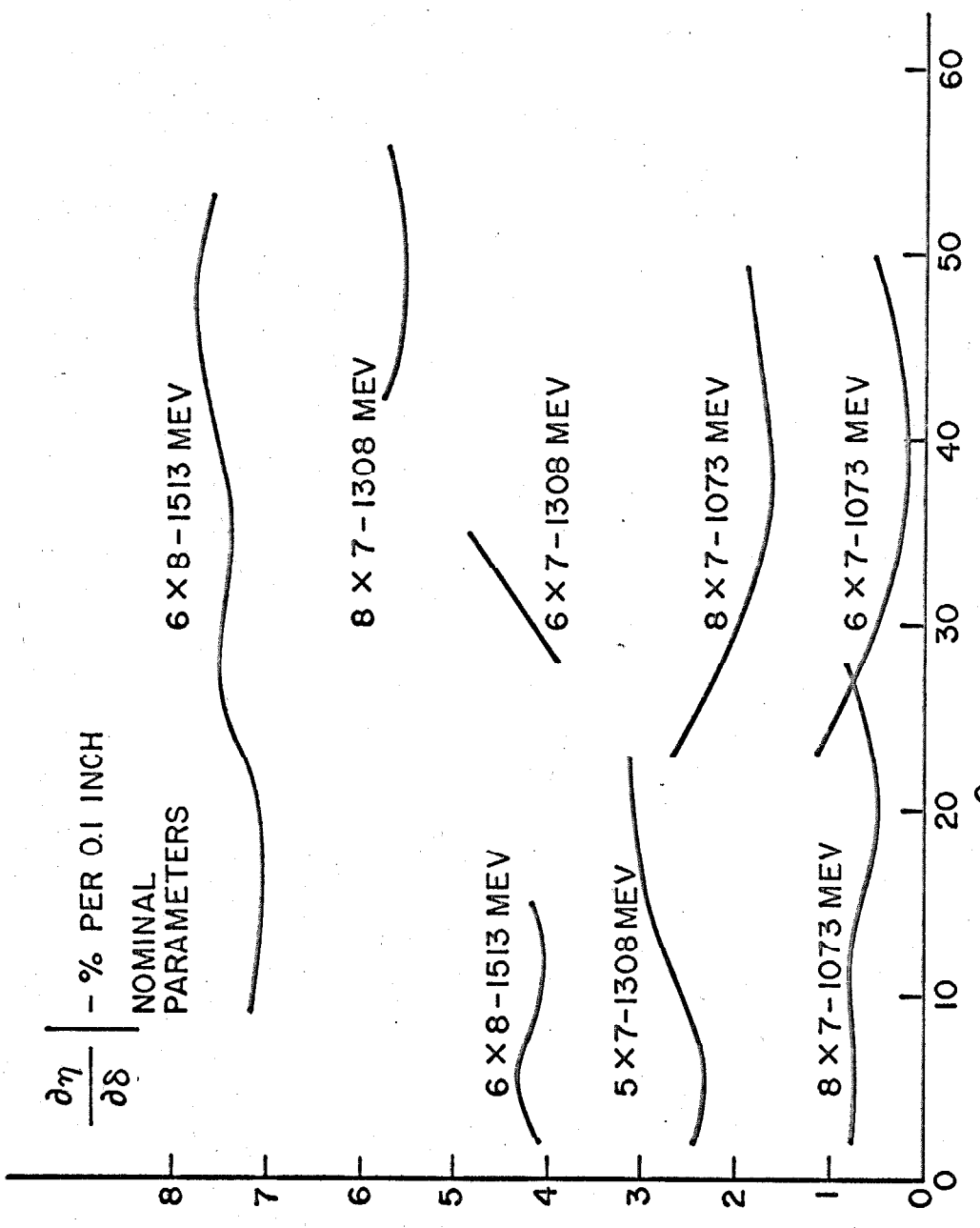

FIGURE E3: $\left|\frac{\partial\eta}{\partial\delta}\right|$ FOR THE VARIOUS APERTURES AND ENDPOINT ENERGIES

$$\frac{\partial \eta}{\partial \delta} \frac{\sin \theta}{\sigma} = 30\% \times 0.2 = 6\% .$$

Corrections also must be made due to the increase in the height (h) of the aperture. Typically $\sin \theta / \sigma = 0.2$ cm and $\partial \eta / \partial h = 6\%/\text{cm.}$, hence this correction is 1.2%. Both corrections are made to the efficiency.

Appendix F

ADDITIONAL EXPERIMENTAL DETAILS

a. Background Subtraction

In an experiment where high resolution is desired, empty target background measurements should be made during the same operating periods as the foreground (i.e., the same day in this experiment). Since there was some uncertainty in the calibration technique to the extent of ± 2%, it would be expected that the analysis of data taken on the same day would yield spectra which were dependent on the calibration only in the location of their mean pion energy. Unfortunately, the condensing target used in this experiment had no means for safe rapid emptying. However, whenever time permitted empty target runs were made at the beginning or at the end of the running period and used in conjunction with foreground runs made at the same angle on the same day. Spectra produced in this way compared in shape favorably with the computed spectra for a flat cross-section.

For the main portion of the experiment background runs were not made on the same day as foreground runs. This makes spectrum fitting more difficult because the background calibration must be in register with the foreground calibration. Because of the uncertainty of the daily calibration this was difficult to do.

However the average cross-section is computed by summing the counts above the pion energy cutoff (valley in the spectrum) in the background subtracted pion spectrum, a process which is only slightly

dependent on the calibration of the background spectrum and which permits a relatively large error in the position of the energy cutoff without producing a large error in the cross-section. This is true since the total number of background counts above cutoff is about 10% of the foreground and the uncertainty in the cutoff position introduces only a 10% error in the total background count, i.e., about 1% of the foreground. Fitting of a spectrum, on the other hand, is effected greatly by the tails of the distribution and consequently the small uncertainties in the spectrum amplitude around the cutoff position induce large fitting errors.

As a check on the status of the experiment the charged particle and gamma-ray counting rates were monitored continuously. The gamma-ray counting rates in the Čerenkov counters for the same angle and energy configuration were found to vary somewhat from day to day. This was attributed to small changes in the voltage bias put on the low energy gamma-rays. Also changes were sometimes observed when a data point was remeasured at a later time. They were attributed to small changes in the synchrotron beam dump and lineup. The latter changes showed up also in the empty target runs and made it necessary to match in time the background runs to foreground runs. The result was good agreement on the resulting cross-sections measured at the same angle and energy but at widely different times.

The counting rate of accidental coincidences was monitored during all foreground runs. Separate runs were made detecting and

pulse height analyzing accidental coincidences in order to obtain the necessary pulse height information to subtract from the foreground runs. An accidental was defined as a coincidence between two gamma-rays, one in each Čerenkov counter, which were 100 ns apart in time. The intensity of the synchrotron beam was generally the same for the accidental runs as it was for the foreground runs, but when it differed a small correction could be made to conpensate for the intensity difference by assuming the rate of accidentals varies like the product of the two gamma-ray counting rates producing the accidentals. The correction for accidentals was highest at small angles where it was always less than 5%. At wider angles the correction was generally only 1% to 2% of the foreground.

In order to protect against accidental vetoing of real pion events due to high charge particle counting rates a coincidence was made between the gamma-rays (γ_A) in one Čerenkov counter and the charged particles (V_B) present in the veto counters in front of the other Čerenkov counter. The accidental veto occurs when a gamma-ray from a real measurable pion event is vetoed by an accompanying signal from one of the two charged particle veto telescopes. The fraction of pions vetoed accidentally is $\frac{(\gamma_A) \cdot (V_B)}{(\gamma_A)}$. This fraction was kept below 1/100.

b. Consistency Checks

The main checks on the results of the experiment were imposed by the cross-sections previously measured by Talman,[1] Diebold,[5] and Alvarez et al.[7]. Additional meaningful tests were

made during the running of the experiment. They consisted of the following:

1) Monitoring counting rates and testing for day-to-day agreement and long term drifts,
2) measuring each cross-section in many short runs spread over a long period,
3) making runs at various aperture sizes and target-aperture distances at angles and energy where it could be done without affecting the detection efficiency adversely,
4) making runs with and without the sweep magnet surrounding the hydrogen target.

In 1) and 2) small drifts were detected in some rates due to variable beam alignment; however, the cross-sections computed were the same provided the background subtraction was done using runs of the same period (see Appendix F, Part a). In 3) the agreement in the cross-section measured at the various configurations served to show that the efficiency calculation was internally consistent to better than 1%. In 4) it was found that the computed cross-sections were unaffected by the presence of the sweep magnet provided proper background subtraction was made.

c. Check on Slope of $\sigma(\theta)$ Near 0°

At angles near 0° where the cross-section falls off very rapidly and tends towards zero at 0° one would expect few symmetric decays. This can be seen in the following way.

The figure below shows the arrangement of the photon beam and gamma-ray detectors when measuring the "zero" degree cross-= section. At "zero" degrees the

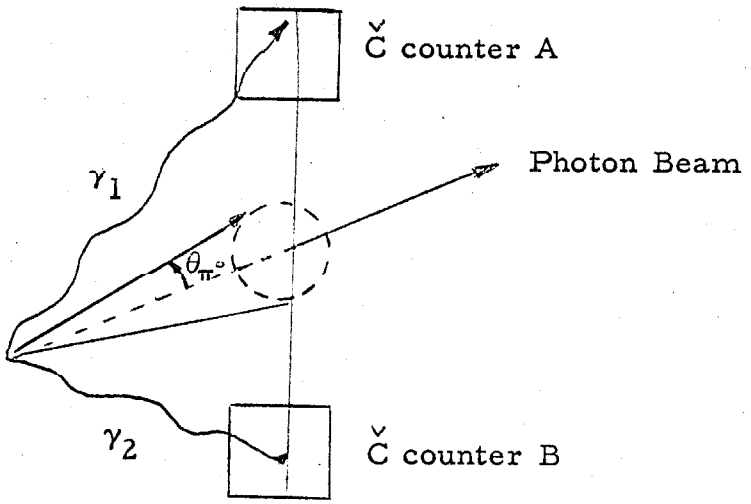

detectors are actually sensitive to production angles out to approximately five degrees in the lab frame (average angle 3.5° in CMS). If the cross-section is zero (or small) at 0° and increases as one moves away from 0° then only decay γ-rays pairs from π° mesons produced at angles off the photon beam line should be detected. As the production angle increases so does the cross-section, hence the π°'s detected would have had to decay asymmetrically to put a gamma-ray in both detectors.

This increase in asymmetrical decays over that expected from a flat cross-section was searched for in the zero degree data in the hope that the variation of the cross-section for the 0° -5° range could be unfolded. Because of the resolution of the counters and the spread of opening angles possible for the decay gamma-rays of the π° no accurate correlation between asymmetry and π° energy

could be made. However, a rough analysis for the three zero degree measurements showed that the cross-section had a slope approximately equal to that obtained by extrapolating the measured points.

Appendix G

COUNTING DATA

In Table G1 the complete counting data is shown for the three photon energies measured. When two different configurations of the detection equipment were used to measure the counting rate at a given angle the several runs were combined by compensating for the difference in detection efficiency. A mean counting rate was computed from the several runs at a given angle and chi square calculated. This is recorded along with the total number of runs -- the number of degrees of freedom = runs -1.

The analysis error is broken down into two parts. The first, Calib, is the error caused by not knowing precisely where the background spectrum cutoff should be taken since the energy calibration was not known exactly. The second, Cutoff, is the error due to the uncertainties in selecting the location of the valley in the foreground spectrum.

Table G1: Complete Counting Data

Angle CM	Counts	Bips	Rate(error)	Chisq (runs)	Empty Target Rate (error)	Accidental Rate(error)	Analysis Calib	Error Cutoff	π^o Rate(error)
		E_o= 1073 MeV	$\bar{k}$ = 911 MeV						
0.	365	1000	0.365(0.019)	0.7(2)	0.082(0.010)	0.005(0.005)	0.000	0.006	0.278(0.023)
5.0	258	540	0.478(0.030)	3.6(2)	0.132(0.019)	0.003(0.004)	0.003	0.007	0.343(0.036)
10.0	420	703	0.597(0.029)	0.1(2)	0.182(0.030)	0.020(0.010)	0.008	0.000	0.395(0.044)
15.0	455	500	0.910(0.043)	0.4(2)	0.120(0.024)	0.010(0.010)	0.023	0.000	0.780(0.055)
21.0	668	560	1.193(0.046)	1.1(2)	0.117(0.022)	0.000(0.010)	0.011	0.016	1.076(0.056)
28.0	1697	1520	1.116(0.027)	4.6(4)	0.088(0.015)	0.033(0.010)	0.010	0.015	0.995(0.037)
35.0	2124	2144	0.991(0.021)	3.2(6)	0.095(0.013)	0.023(0.010)	0.013	0.017	0.873(0.035)
42.0	1108	1370	0.809(0.024)	3.2(5)	0.062(0.011)	0.014(0.010)	0.007	0.010	0.733(0.031)
49.0	1100	1814	0.606(0.018)	0.1(2)	0.072(0.013)	0.000(0.010)	0.005	0.007	0.534(0.026)
		E_o = 1308 MeV	$\bar{k}$ = 1182 MeV						
0.	502	2100	0.239(0.011)	2.6(4)	0.067(0.008)	0.014(0.004)	0.002	0.005	0.158(0.015)
5.0	986	2850	0.346(0.011)	6.4(6)	0.072(0.012)	0.072(0.012)	0.003	0.005	0.202(0.021)
11.0	925	2000	0.462(0.015)	0.2(3)	0.056(0.004)	0.069(0.006)	0.005	0.002	0.337(0.018)
17.0	1337	3160	0.423(0.012)	0.7(3)	0.038(0.006)	0.013(0.005)	0.000	0.000	0.372(0.014)
23.0	1185	2987	0.397(0.012)	5.6(6)	0.038(0.003)	0.010(0.003)	0.000	0.003	0.349(0.013)
28.0	1109	3203	0.346(0.010)	2.2(6)	0.027(0.006)	0.010(0.007)	0.000	0.006	0.309(0.015)
35.0	698	3275	0.213(0.008)	2.6(7)	0.013(0.006)	0.004(0.003)	0.000	0.003	0.196(0.011)
42.0	390	2300	0.170(0.009)	5.7(5)	0.018(0.004)	0.000(0.000)	0.000	0.002	0.152(0.010)
49.0	340	3131	0.109(0.006)	4.9(6)	0.007(0.004)	0.000(0.000)	0.001	0.001	0.102(0.007)
56.0	358	4000	0.089(0.005)	9.0(6)	0.010(0.003)	0.000(0.000)	0.000	0.000	0.079(0.006)
		E_o = 1513 MeV	$\bar{k}$ = 1390 MeV						
0.	172	1016	0.169(0.013)	2.3(4)	0.045(0.012)	0.000(0.010)	0.000	0.004	0.124(0.021)
5.0	239	751	0.318(0.021)	0.5(3)	0.092(0.030)	0.000(0.010)	0.000	0.009	0.226(0.039)
10.0	1050	1078	0.974(0.030)	5.0(5)	0.275(0.020)	0.200(0.018)	0.005	0.010	0.499(0.042)
15.0	871	1100	0.792(0.027)	1.2(4)	0.140(0.020)	0.030(0.020)	0.013	0.019	0.622(0.045)
21.0	621	1200	0.517(0.021)	1.5(3)	0.056(0.015)	0.010(0.010)	0.005	0.014	0.451(0.031)
26.0	321	1450	0.221(0.012)	3.8(4)	0.018(0.010)	0.000(0.010)	0.001	0.006	0.203(0.020)
32.0	141	1020	0.138(0.012)	0.4(2)	0.018(0.010)	0.000(0.010)	0.001	0.004	0.120(0.019)
39.0	164	1650	0.099(0.008)	1.5(3)	0.015(0.010)	0.000(0.000)	0.000	0.003	0.084(0.013)
46.0	138	1150	0.120(0.010)	0.1(2)	0.016(0.006)	0.000(0.000)	0.000	0.005	0.104(0.013)
53.0	134	1400	0.096(0.008)	0.6(2)	0.014(0.010)	0.000(0.000)	0.000	0.005	0.082(0.014)

REFERENCES

1. R. M. Talman, C. R. Clinesmith, R. Gomez, A. V. Tollestrup, Phys. Rev. Letters 9, 177 (1962).

2. M. J. Moravcsik, Phys. Rev. 125, 734 (1962).

3. H. Ruderman, R. Gomez, and A. V. Tollestrup, California Institute of Technology Laboratory Report C. T. S. L. -31, (1962 unpublished).

4. C. R. Clinesmith, Thesis, Ph. D., California Institute of Technology (1967).

5. R. Diebold, Phys. Rev. 130, 2089 (1963).

6. Private Communication with F. B. Wolverton.

7. R. Alvarez, Z. Bar-Yum, W. Kern, D. Luckey, L. S. Osborne, S. Tazzari, and R. Fessel, Phys. Rev. Letters 12, 707 (1964).

8. Private Communication with L. S. Rochester.

9. M. Braunschweig, D. Husmann, K. Lübelsmeyer, D. Schmitz, Presented at XIII High Energy Physics Conference, University of California, Berkeley, California (1966).

10. R. M. Talman, Thesis, Ph. D., California Institute of Technology (1963).

11. H. A. Thiessen, CTSL Internal Report No. 22, California Institute of Technology (1966).

12. D. E. Groom, CTSL Internal Report No. 12, California Institute of Technology (1966).

13. H. D. I. Abarbanel, C. G. Callan, Jr., and D. H. Sharp, Phys. Rev. 143, 1225 (1966).